# Partial Discharge Characterization of New Environmentally Friendly Insulating Liquids

## A study on the Insulating Behaviour of Transformer Liquids

M. Fazlalizadeh

NTNU

TU Delft

Delft University of Technology/Norwegian University of Science and Technology

# Partial Discharge Characterization of New Environmentally Friendly Insulating Liquids

## A study on the Insulating Behaviour of Transformer Liquids

by

Mohammad Fazlalizadeh

to obtain the degree of Master of Science in Electrical Engineering

at the Delft University of Technology,

and the degree of Master of Science in Wind Energy
at the Norwegian University of Science and Technology

to be defended publicly on Friday July 12, 2024 at 03:00 PM.


| | | |
|---|---|---|
| Student number: | TU Delft: 5766419 / NTNU: 103111 | |
| Project duration: | October 1, 2023 – June 17, 2024 | |
| Thesis committee: | Prof. ir. P.T.M. (Peter) Vaessen, | Prof. K. (Kaveh) Niayesh, |
| | Dr. M. (Mohamad) Ghaffarian Niasar, | L. E. (Lars) Lundgaard, |
| | Dr. J. (Jianning) Dong, | Dr. T. G. (Torstein) Aakre |



Cover: https://www.qualitrolcorp.com (Modified)
Style: TU Delft Report Style, with modifications by Daan Zwaneveld

An electronic version of this thesis is available at http://repository.tudelft.nl/.


NTNU
Kunnskap for en bedre verden

SINTEF

EWEM

TU Delft

# Preface

To begin with, I would like to mention my father, Eng. Rafi Fazlalizadeh, who was always by my side. Without his unwavering support and attention, this work would not have been possible. He consistently encouraged and supported me, even when he was seriously ill. I also extend my deepest gratitude to my mother for providing for me during the early stages of my life and for her unreserved help and patience during my absence while completing this work.

I extend my appreciation to SINTEF Energy Company for providing the necessary equipment to perform the required tests and to Dr. Torstein Grav Aakre for his constant and unwavering assistance throughout many steps of this project. Special thanks to my supervisor, Professor Kaveh Niayesh, for his continuous help and follow-up during this project.

I would like to thank chief scientist Lars Esben Lundgaard for his full support and the extensive knowledge he shared throughout the project, and Dr. Mohamad Ghaffarian Niasar, my co-supervisor, whose valuable reviews guided the progress of this project.

In a broader view, I would like to express my gratitude to Toomaj Salehi, an Iranian rap singer whose only ”sin” was singing songs that advocate freedom for all Iranians. He has shown immense courage by standing firm for over a year and a month in prison, facing a death sentence for his music. His valour in standing alone for the entire community is deeply inspiring.
I am profoundly grateful to all the teachers and professors who, through their dedication and self-sacrifice beyond their assigned duties, inspired my interest in scientific progress and instilled in me a thirst for truth. I would like to specifically thank Mr. Farokhi, my elementary school physics laboratory teacher, and Mr. Mosannen, an experienced physics laboratory teacher at SAMPAD High School. Additionally, my heartfelt thanks go to Dr. Yazdan Ashkvari, my professor of electrical engineering at the University of IAU, and Dr. Amir Abbas Shayegani Akmal, an associate professor at the University of Tehran.

I am also grateful to my friend, Eng. Soheil KHosro Gorji, for his continuous support. My gratitude also goes to my dear friends and colleagues in the Power System track of the EWEM program 2022: Eng. Jens Kruse Hansen, Eng. Julian Wuijts, Eng. Sander Skogen, and Eng. Juri Volodin, for their help and guidance during this program.

Lastly, I would like to thank the people at NTNU’s mechanical and electrical workshops for their help when constructing the test setup.

*M. Fazlalizadeh*
*Trondheim, July 2024*

# Summary

Unwanted breakdown of insulation is one of the primary challenges affecting the reliability of power systems. Liquid insulation is commonly used in power grids and subsea installations due to its preferred qualities, such as heat transfer and safety. Some insulating liquids have been available since the earliest times, and some have been proven to be harmful to humans, animals, and the environment. Consequently, the search for better candidates has always been ongoing. Unfortunately, the knowledge of the quality of the insulating liquids is insufficient since numerous phenomena related to electrical discharge and breakdown in insulating liquids happen unexpectedly, often surprising the personnel involved.

Therefore, gaining a deep understanding of the breakdown physics of these liquids and mechanisms leading to the degradation of their dielectric properties is crucial. this understanding ensures that the new replacements are suitable for specific equipment. Partial discharge (PD), as one of the initial stages before breakdown and a major player in ageing the insulators, is the main focus of this work. One way to monitor a liquid's insulation quality is through the Partial Discharge Inception Voltage (PDIV) level. Based on PDIV measurements, there are defined standards, such as IEC 61294. This work is focused on investigating the behaviour of different types of liquids under the AC voltage stress above and below the PDIV level to determine if the defined standards reflect the dielectric characteristics of each liquid properly.

Three liquids have been examined, including two candidates from commonly used insulating liquids in electrical installations. Tests are performed in a needle-plane geometry under high-voltage AC stress. The same liquids and geometry have been used multiple times in previous studies under lower-frequency AC voltage, yielding unexpected results. Therefore, this study aims to investigate deeper by testing the liquids at higher frequencies and comparing observations with previous results. The experimental setup used for this work includes a $20\,\mathrm{kV}$ resonance voltage source, and the needle-plane gap distance is $20\,\mathrm{mm}$. The current flow from the plane to the needle is mostly capacitive in the range up to $100\,\mathrm{nA}$, but space charges are proved to play a major role in the conductive component of the current. PD behaviour has been found to relate to molecular structure and, in some cases, to the previous stresses, likely due to residual ions remaining from previous cycles. The presence and nature of space charges have been investigated carefully by testing liquids at higher frequencies below and above the PDIV level. Further, the test setup was facilitated, and half-cycle voltages were applied to involve only one polarity of space charges, and the differences were observed. Another part of this work involved the optical PD measurement method, which utilized two photomultiplier tubes (PMTs) and a coincidence circuit to filter out ambient dark noise. This method was employed alongside the well-known charge acquisition method to detect the initial PD pulses in the liquid. The results demonstrated a noteworthy difference between the two methods, prompting further investigation.

# Contents

# List of Figures

# List of Tables

# Nomenclature

## Abbreviations

| Abbreviation | Definition |
|---|---|
| AC | Alternative Current |
| DC | Direct Current |
| HV | High voltage |
| IEC | International Electrotechnical Commission |
| ISA | International Standard Atmosphere |
| ISO | International Organization for Standardization |
| PCB | Polychlorinated Biphenyl |
| PCT | Polychlorinated Terphenyls |
| PD | Partial Discharge |
| PDIV | Partial Discharge Inception Voltage |
| PMT | Photo Multiplier Tube |
| RMS | Root Mean Square |
| SCLC | Space Charge Limited Current |
| UV | Ultraviolet Radiation |
| CFD | Constant fraction discriminator |

## Symbols

| Symbol | Definition | Unit |
|---|---|---|
| $V$ | Voltage | [v] |
| $r_0$ | Needle tip radius | [m] |
| $J$ | Current density | $[\mathrm{A/mm^2}]$ |
| $\rho$ | Charge density | $[\mathrm{C/mm^3}]$ |
| $J_0$ | The current density of charges with a charge density of $\rho_0$ | $[\mathrm{A/mm^2}]$ |
| $e$ | amount of charge of an electron | [C] |
| $m_e$ | mass of an electron | [g] |
| $q$ | Charge | [C] |
| $C$ | Capacitance | [F] |
| $E$ | Electric field | [V/m] |
| $r_b$ | Radius of the crosssection | [m] |
| $f$ | Frequency | [1/s] |
| $g$ | Gain | |
| $Q$ | Quality factor | |
| $\rho$ | Density | [kg/m$^3$] |
| $\mu$ | Mobility | $[\mathrm{m^2V^{-1}s^{-1}}]$ |
| $\tau$ | Period | [s] |
| $\nu$ | Velocity | [m/s] |
| $\mu_z, \nu_z, \phi_z$ | ellipsoid coordinate axis moments | |
| $\eta, \zeta$ | spherical coordinate moments | |

# 1

# Introduction

## 1.1. On the History of Insulators

The need for a good insulator has a history as old as the commercial use of electric energy. There have been numerous materials tested and employed since the 18th century as insulators. From the pieces of wood within primitive electrical circuits to the most advanced thermal and electrical insulator materials inside spaceships nowadays. They all use different kinds of materials as insulators to prevent the electric current from flowing in unwanted directions.

### 1.1.1. Transformer Oil as an Insulator

The primary function of the transformer oil is to bring good insulation between conductors inside the transformer. Another important duty is cooling the transformer coils and taking away the heat generated inside the transformer due to losses. It must, therefore, have high dielectric strength, thermal conductivity, and chemical stability and should keep these properties even at high temperatures for extended periods. Transformer oil or insulating oil is a stable oil at high temperatures and has excellent electrical insulating properties. It has been used vastly in oil-filled transformers, switchgear, and cables.

They preferably have flash points greater than $140°\mathrm{C}\,(284°\mathrm{F})$, pour points less than $-40°\mathrm{C}\,(-40°\mathrm{F})$, and a dielectric breakdown greater than $28\mathrm{kV}_{\mathrm{RMS}}/\mathrm{mm}$ [1].

### 1.1.2. Diversity of the Liquids Used for This Purpose

A key insulating oil for use inside transformers is mineral oil. petroleum-based oils were the primitive oils that were used in 1892. however, because of the lower price, the industry moved to paraffin-based mineral oil besides its low properties like high pour point or the generation of insoluble sludge. transitioning from 1925, naphtha-based oil was commonly used in transformers, but some drawbacks, like high flammability, put installations at huge risk [2]. In 1930, Polychlorinated biphenyl (PCB) was introduced as an alternative. The flammability concerns 1899 the industry had moved to solved, but PCB's toxicity and non-biodegradable nature posed environmental hazards [3]. By revealing the danger of these materials the scope of interest has been changed to other liquids like silicon oil, introduced in 1970, replicated PCB's properties, but its widespread use was limited due to high prices.
The 1990s saw the advent of synthetic esters, which were mostly synthesised from Alcohols and acids [4], offering enhanced dielectric strength, biodegradability, lower viscosity, and higher fire resistance. A histogram of the development of the transformer oil has been shown in Figure 1.2.
As environmental regulations tightened, vegetable oil and natural esters gained prominence. Subsequently, in 2006, a blend comprising 80% mineral oil and 20% synthetic ester proved to enhance insulating oil performance [5]. Between 2008 and 2012, there was a shift towards vegetable oil-based palm fatty acid esters, alongside research exploring nanofluids' potential in transformer insulation [6, 7]

## 1.2. Environmental Impact of Transformer Liquids

Due to mineral oil's numerous drawbacks, such as limited biodegradability, potential future scarcity, and the presence of poly-nuclear aromatic hydrocarbons, which can be easily released into the environment in the event of a transformer explosion, ester oils have garnered attention as a promising alternative to mineral oil [4, 8]. contamination risk of the water supply is more severe compared to the contamination risk of soil [9]. Environmental concerns about using the mineral oils have been increased due to the low ratio of biodegradability (less than $20\%$ over a 28-day period [10]) of the mineral oils.

### 1.2.1. European Commission Directive on the Disposal of PCBs/PCTs

PCBs and PCTs, synthetic compounds manufactured extensively worldwide from the 1930s to the 1980s, found broad applications in lubricants and various electrical and hydraulic equipment. Their widespread use has resulted in their presence being detected in soil, surface water, groundwater, and even food sources. Classified as probable human carcinogens, these chemicals induce various adverse effects in both human and animal populations.

On 16 September 1996, the European Commission identified PCBs as *highly toxic* and *heavily re-*

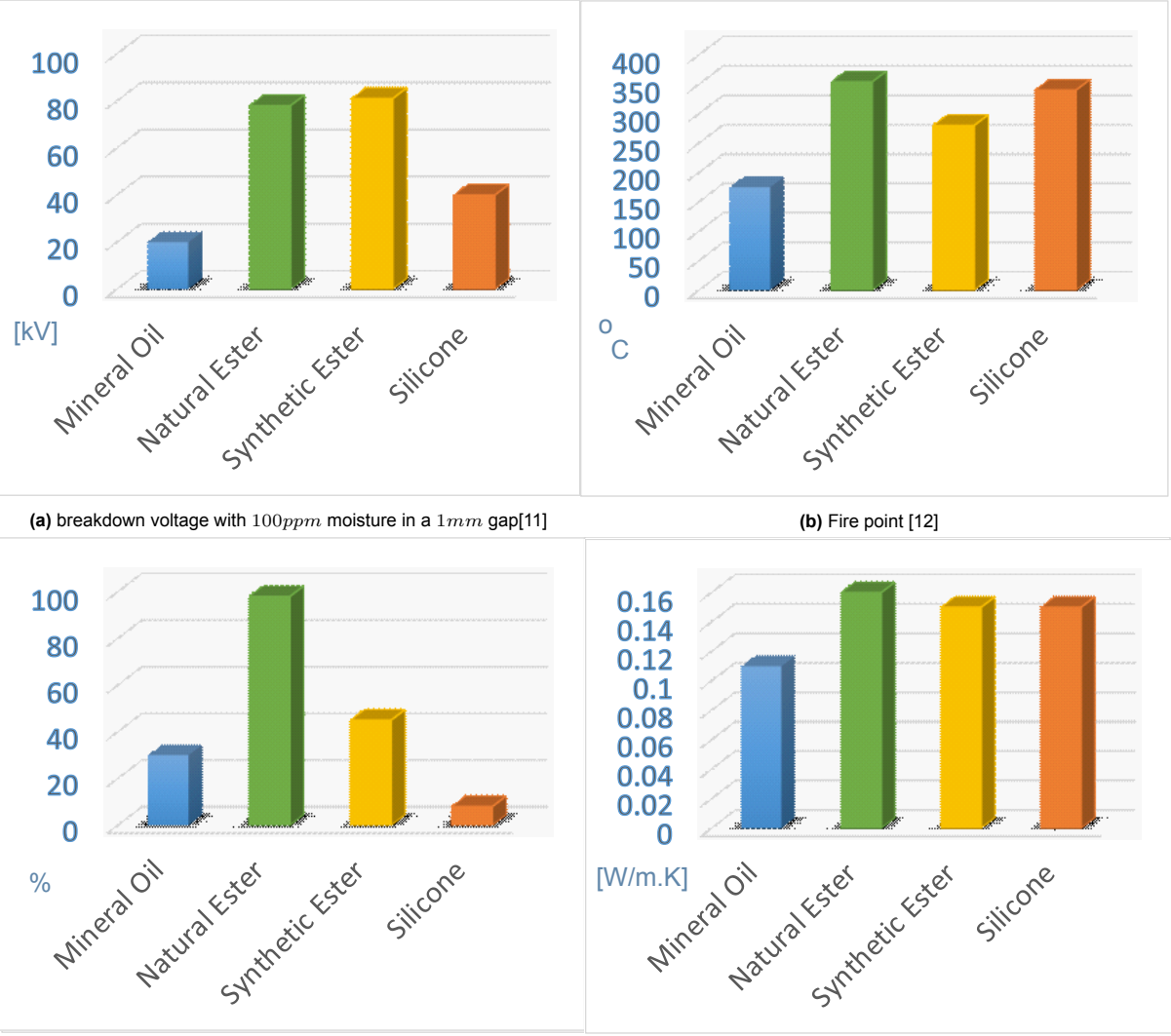


**(a)** breakdown voltage with $100ppm$ moisture in a $1mm$ gap[11]

**(b)** Fire point [12]

**(c)** Biodegradability (21 days) [13]

**(d)** Thermal conductivity [12]

**Figure 1.1:** Comparison of typical characteristics of transformer oils

*stricted*. Therefore, a time schedule has been defined for the disposal of these products[14]. Products containing these chemicals are still being discarded, and so this type of waste must be handled with great care [14].

### 1.2.2. New Environmentally Friendly Liquids

The development of new insulating liquid materials is driven by various factors, including environmental requirements, safety concerns, and economic considerations. Consequently, transformer manufacturers are encountering new specifications aligned with these evolving demands. Vegetable oil-based transformer fluids are increasingly supplanting mineral oil-based products in the market due to their superior performance and notable environmental and safety benefits.

In 1892, the feasibility of using ester oil extracted from seeds was tested; however, no significant efforts were undertaken until the severe oil crisis of 1970. Researchers once again turned their attention to the use of vegetable oils due to their high biodegradability ($> 95\%$), low toxicity, high flash points, and reduced flammability, making them more environmentally friendly. There are many important characteristics that different oils can be compared for use as transformer oil. but the most important characteristics that can be named for this purpose include electrical, physical, and chemical characteristics. Among these characteristics, there are some important ones like biodegradability, flash fire point, and price and production capacity.

Figure 1.1 and Table 1.1 show comparisons of some of the important characteristics between different types of transformer oils.
biodegradability is a two-sided matter. It is good to have a transformer oil that can last for longer, but on the other hand, if for any reason it spills into the environment, it is better to have a high biodegradability factor to dissolve quickly.

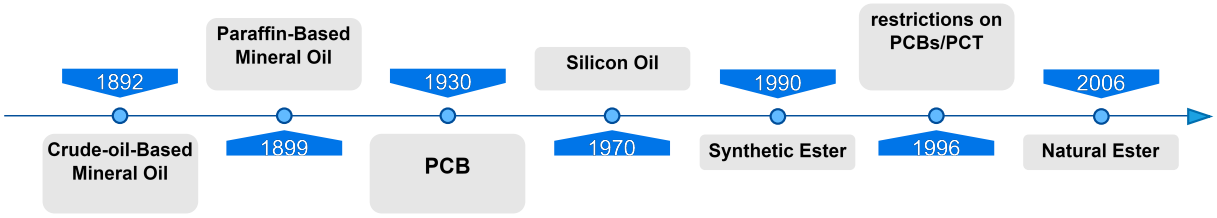


**Figure 1.2:** Histogram of development of the transformer liquids over time

## 1.3. Objectives of This Work

While various standards exist to assess the quality and properties of transformer oils [15, 16], there remains a significant question regarding whether these standards truly reflect the performance of these liquids when used as transformer oil. This uncertainty arises because each standard was developed based on the properties of the prevalent liquid at the time of its inception.
Initially, this approach was appropriate as it allowed for the differentiation between high-quality, functional transformer oil and inferior, unsuitable alternatives, thus establishing a means to regulate transformer oil quality. However, with the introduction of new liquids, such as synthetic ester, as relatively green transformer oils and newer candidates, these standards may no longer align with the characteristics of these newer liquids. In this study, our focus lies on examining the dielectric characteristics of different insulating liquids. The aim is specifically to investigate deeper into the partial discharge formation in dielectric liquids.
Experimenting with various liquids to observe their electrical behaviour under high voltage AC voltage with different frequencies is the main approach of this work. Careful investigation of the process of inception of partial discharge across different liquids and the role of space charges in initiating partial discharges within the liquids will be studied.
Partial discharge detection with different methods to evaluate the procedure of PD is one of the goals of this work. Assessing the accuracy and reliability of the evaluation process of standard based on insights garnered from experimental observations across different insulation liquids will be performed.
A schematic of the thesis outline can be found in Figure 1.3.

**Table 1.1:** Comparison transformer oils typical values [17]

| Property | Mineral oils | Silicone oils | Synthetic esters | Vegetable oils | Test method |
|---|---|---|---|---|---|
| Dielectric breakdown, kV | 30–85 | 35–60 | 45–70 | 82–97 | IEC 60156 |
| Relative permittivity at 25°C | 2.1–2.5 | 2.6–2.9 | 3.0–3.5 | 3.1–3.3 | IEC 60247 |
| Viscosity at 0°C, $mm^2\ s^{-1}$ | 76 | 81–92 | 26–50 | 143–77 | ISO 3104 |
| at 40°C | 3–16 | 35–40 | 14–29 | 16–37 | |
| at 100°C | 2–2.5 | 15–17 | 4–6 | 4–8 | |
| Pour point, °C | $-30$ to $-60$ | $-50$ to $-60$ | $-40$ to $-50$ | $-19$ to $-33$ | ISO 3016 |
| Flash point, °C | 100–170 | 300–310 | 250–270 | 315–328 | ISO 2592 (1) |
| Fire point, °C | 110–185 | 340–350 | 300–310 | 350–360 | |
| Density at 20°C, $kg\ dm^{-3}$ | 0.83–0.89 | 0.96–1.10 | 0.90–1.00 | 0.87–0.92 | ISO 3675 |
| Specific heat, $Jg^{-1}\ K^{-1}$ | 1.6–2.0 | 1.5 | 1.8–2.3 | 1.5–2.1 | ASTM E1269 |
| Thermal conductivity, $Wm^{-1}\ K^{-1}$ | 0.11–0.16 | 0.15 | 0.15 | 0.16–0.17 | DCS |
| Expansion coefficient, $10^{-4}\ K^{-1}$ | 7–9 | 10–6.5 | 10–5.5–5.9 | | ASTM D1903 |

(1) Cleveland open cup procedure.

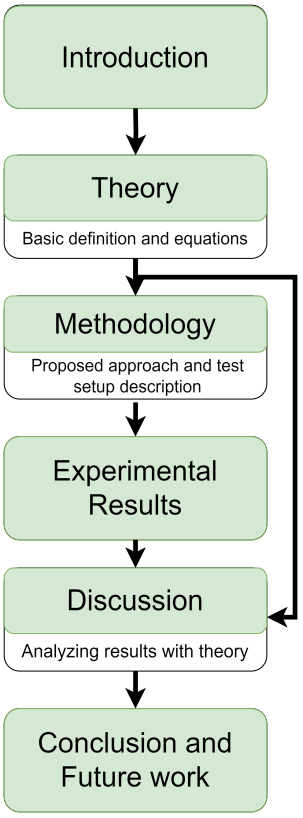


**Figure 1.3:** Flowchart illustrating the thesis outline

# 2

# Theory

## 2.1. Electrical Standards Related to Transformer Oils

The International Electrotechnical Commission (IEC) is a worldwide organization that standardizes electrical and electronic equipment in close cooperation with ISO. IEC has defined different standards for evaluating the electrical characteristics of transformer oils.
Some important standards with their release date have been listed in Table 2.1. By examining the years of release of the standards along with the histogram depicted in Figure 1.2, it becomes evident that certain standards were established before introducing newer environmentally friendly transformer oils. A careful focus specifically on the IEC 61294 standard is required, which outlines the inception voltage of partial discharges in transformer liquids.
However, revisiting some basic physical concepts is crucial to prior to a technical discussion of the IEC 61294 standard.

**Table 2.1:** Standards related to transformer oil

| Standard Code | Year of Definition | Description |
|---|---|---|
| IEC 60156 | 1963 | Method for the determination of the electric strength of insulating oils |
| IEC 60270 | 1981 | Partial discharge measurements |
| IEC 60897 | 1987 | Methods for the determination of the lightning impulse breakdown voltage of insulating liquids |
| IEC 1072 | 1991 | Methods of test for evaluating the resistance of insulating materials against the initiation of electrical trees |
| ISO 5725 | 1986 | Precision of the test methods - Determination of repeatability and reproducibility for a standard test method by inter-laboratory tests |
| IEC 61294 | 1993 | Insulating liquids - Determination of the partial discharge inception voltage (PDIV) - Test procedure |
| SS-EN 60455-3-1 | 2003 | Resin-based reactive compounds used for electrical insulation - Part 3: Specifications for individual materials - Sheet 1: Unfilled epoxy resinous compounds |
| SS-EN 61100 | 1993 | Classification of insulating liquids according to fire point and net calorific value |
| SS-IEC 628 | 1986 | Insulating oils - Gassing of insulating liquids under electrical stress and ionization |

### 2.1.1. IEC 61294 Standard for Determining PDIV

IEC 61294 is a technical report that states the progress of a method to measure PDIV [15]. According to [15], PDIV of an insulating liquid is the lowest voltage at which a PD occurs of an apparent charge equal to or exceeding $100\,\mathrm{pC}$ when the sample is tested under the specific conditions. The purpose of the configuration of the test cell is to create a point-sphere gap. It consists of a $12.5\,\mathrm{mm}$ to $13\,\mathrm{mm}$ diameter steel ball bearing and a point electrode which should be $3\,\mu\mathrm{m}$ radius tip with a distance of $50\mathrm{mm} \pm 1\mathrm{mm}$ between two electrodes. The volume is about $300\,\mathrm{ml}$ [15]. The high voltage circuit shall provide an AC voltage frequency $48\,\mathrm{Hz}$ to $62\,\mathrm{Hz}$ fully sinusoidal and PD free [15]. The PD measuring device shall be in range of $10\,\mathrm{kHz}$ to $300\,\mathrm{kHz}$ [15].
test liquid shall be filtered through the vacuum by a $5\,\mu\mathrm{m}$ sintered glass [15]. the procedure includes filling the test cell and waiting for some time, then increasing the voltage with the rate of $1\,\mathrm{kV/s}$ until a $100\,\mathrm{pC}$ partial discharge is observed and rapidly bringing the voltage to zero and repeat it for $10$ times with the same test sample and after that do the test once again with a new needle and also renew the liquid and execute the same test. Then calculate the mean value of two inception voltages [15].
the proposed test cell in this standard has been shown in the Figure 2.1.

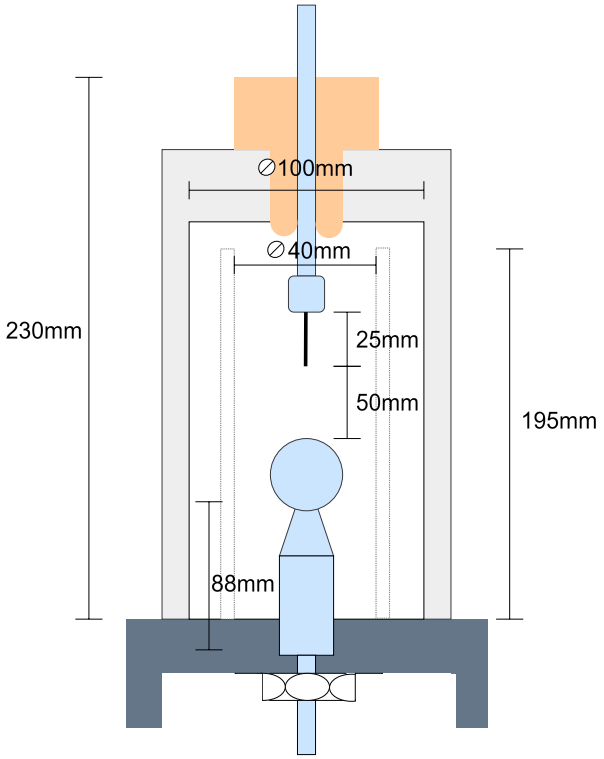


**Figure 2.1:** Dimensions of an IEC 61294 standard test cell for PDIV test implemented from [15]

## 2.2. Needle-Plane Geometry in Electrostatics

Point-plane geometry is a configuration in electrostatics that involves analyzing the electric field produced by a point electrode in the vicinity of an infinite conducting plane. In this setup, a singular point electrode is positioned at a certain distance above or below an infinitely large, flat conducting surface. The primary objective of studying point-plane geometry, which is also known as needle-plane geometry (will be mentioned as needle-plane after this), is to understand the distribution of electric field and the resulting electric potential in the space between needle and plane.

The resulting nonlinear electric field in the space between the point and the plane is according to the Laplacian field. This configuration can go up to $1000\,\mathrm{kV/mm}$ without breaking down in a reasonable test volume.
Various analytical methods exist for calculating the electric field in a needle-plane configuration. There are two main approaches to approximating the needle tip curve. It can be considered as a hyperboloid or as a cone.

Radu has shown in a comparative study [18] that the hyperboloidal model of the needle is more precise for calculating the field strength at the tip of the needle (the maximum field) and along the symmetrical axis. However, this model leads to significant errors in calculating the field for other points, especially for the points neighbouring the area of the conical surface of the needle.

### 2.2.1. Hyperboloidal Model of the Needle Tip

By considering the prolonged ellipsoid system of coordinates $(\mu_z, \nu_z, \phi_z)$, Durand [19] and Mason [20] obtained a general relation of the electric field in every point inside the domain $D$ which is axially symmetrical.

$$E_{M,N}(\mu_z, \nu_z) = \frac{2U}{Ac} \frac{1}{\sqrt{(\mu_z^2 - \nu_z^2)(1 - \nu_z^2)}} \tag{2.1}$$

where $U$ is the difference in potentials of the electrodes ($U = V_1 - V_2$, in Figure 2.2), $d$ is the distance between electrodes, $c = \sqrt{d^2 + dr_0}$ the focal distance of the homo focal hyperboloid and ellipsoids,

$A = ln((c+d)/(c-d))$ is a constant, and the axis domains are $\mu_z \in [1, \infty),\ \nu_z \in [0, d/c],\ and\ \phi_z \in [0, 2\pi]$

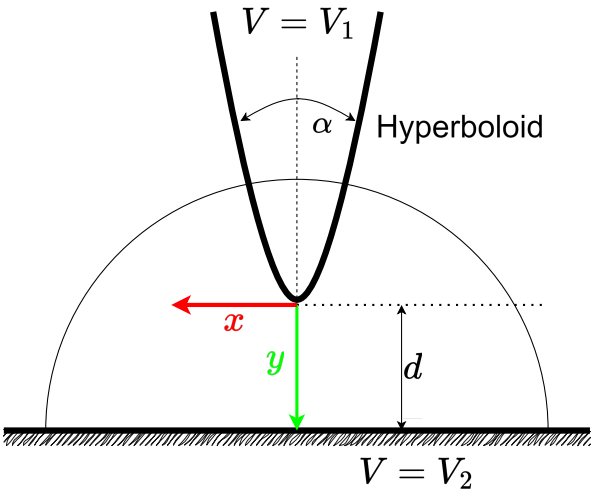


**Figure 2.2:** Hyperboloidal needle-plane geometry adopted from [18]

Bamji in [21] investigates the use of the boundary element method to calculate electric field profiles at needle tips. The study compares the boundary element method with the finite difference and finite element methods. The paper discusses the importance of accurately determining local electric fields in polymeric insulation to prevent degradation and failure of high-voltage devices. It explains the limitations of the finite difference and finite element methods and introduces the boundary element method as an alternative approach. The relation for the electrical field at the needle tip, which is placed at the coordinate origin, is [21]:

$$\begin{aligned} E(y) &= E_{max} \frac{dr_0}{dr_0 + 2dy - y^2} \\ E_{max} &= \frac{2U}{r_0 \cdot \ln(1 + 4d/r_0)} \end{aligned} \tag{2.2}$$

In [18], Radu has used this method to estimate the electrostatic field in a needle plate arrangement with the characteristics as ($r_0 = 10\mu\mathrm{m}, d = 2.5\mathrm{mm}, U = 5\mathrm{kV}$. This analytical model has been compared with a numerical model based on the finite element method using a Cartesian system of coordinates, using $n = 14000$ nodes and a $m = 27492$ finite elements network. The errors of the analytical method compared to the numerical method have been concluded in the Table 2.2. The difference reference is:

$$\epsilon_{an} = (E_n - E_a)/E_n \tag{2.3}$$

Radu has considered the deviation of the numerical method to be less than 1% at the needle tip and below 0.1% for the points located at more than $10\,\mu\mathrm{m}$ from the needle tip. It is obviously a deviation of 0.22% at the closest point that, if added to the possible deviation of the numerical method, could result in a total deviation of 1.22% from the real electric field at the needle tip.

### 2.2.2. Sensitivity of Electric Field to the Geometry

Meanwhile, the hyperboloidal model might give a good approximation for the electric field at the needle tip. However, the Laplace equation is a useful tool for approximating the electric field in the points with distance to the needle tip. According to Moon and Spencer [22], the voltage over the gap can be defined as:

$$V(\eta) = B \ln \tan(\eta/2) \tag{2.4}$$

therefore, the electric field can be defined as

$$E = \frac{1}{a\sqrt{\sinh^2 \zeta + \sin^2 \eta}} \frac{B}{\sin \eta} \hat{\eta} \tag{2.5}$$

**Table 2.2:** Comparison of the Laplacian electrical field on the needle axis by analytical ($E_a$) and numerical($E_n$) approaches adopted from [18]

| $y(\mu m)$ | 0.2 | 1 | 4 | 10 | 30 | 50 | 100 | 400 | 1500 | 2400 |
|---|---|---|---|---|---|---|---|---|---|---|
| $E_a(\mathrm{kV/mm})$ | 139.8 | 121.1 | 80.75 | 48.42 | 20.82 | 13.3 | 7.04 | 1.94 | 0.687 | 0.579 |
| $E_n(\mathrm{kV/mm})$ | 139.5 | 121.2 | 80.99 | 48.71 | 20.97 | 13.4 | 7.09 | 1.96 | 0.689 | 0.579 |
| $\epsilon_a n(\%)$ | -0.22 | 0.08 | 0.3 | 0.58 | 0.71 | 0.7 | 0.69 | 0.62 | 0.31 | 0.05 |

Where a and B are defined as follows:

$$B = \frac{V}{\ln(\tan(\frac{\pi}{2} - \sqrt{(1-\frac{d}{a})/2}))} \tag{2.6}$$

$$a = d + \frac{r_p}{2} \tag{2.7}$$

Based on the above relation, the sensitivity of the electrical field to the parameters can be obtained from equation Equation 2.8 [23].

$$\frac{\Delta E_{tip}}{E} = \frac{\Delta V}{V} + \frac{\Delta r_p}{r_p}\left(1 + \frac{1}{\ln\frac{4d}{r_p}}\right) + \frac{\Delta d}{d}\left(\frac{1}{\ln\frac{4d}{r_p}}\right) \tag{2.8}$$

According to this equation, any change in the voltage will change the field with the same amount. A change in the magnitude of $1\,\mu\mathrm{m}$ of the tip radius of the needle around $5\,\mu\mathrm{m}$ will change the electrical field by 22%, and a change in the magnitude of $1\,\mathrm{mm}$ over $d = 20\mathrm{mm}$ will change the electric field by 0.5% [23]. Therefore, the electric field intensity changes drastically by any changes in the needle tip radius [23]. Figure 2.3 showing the results of Equation 2.2 for different voltage levels and different tip radii in range with the values that will be used in this work. They clearly show the exponential increase in the field strength by decreasing the distance to the needle tip.

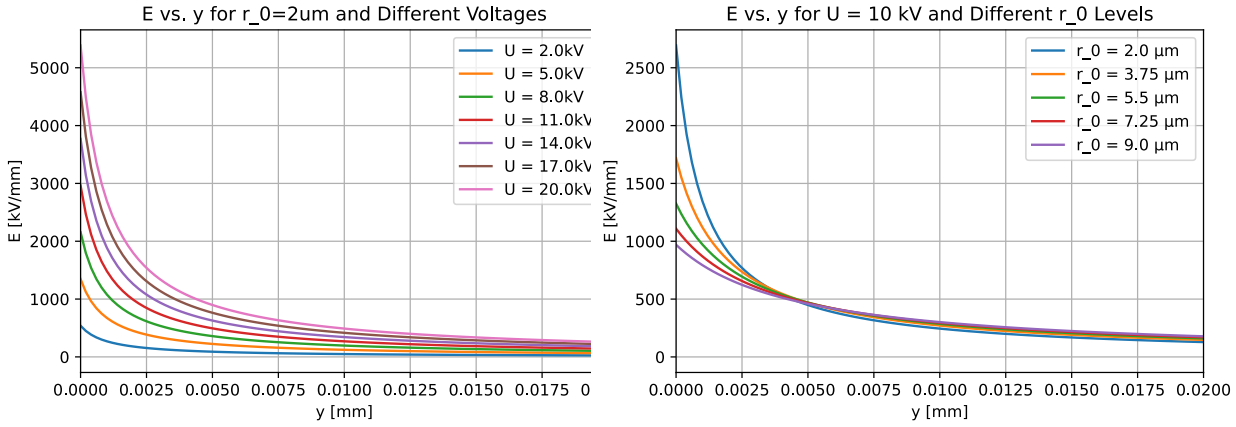


**(a)** Different voltages with $r_0 = 2\mu\mathrm{m}$

**(b)** Different tip radii with $U = 10\mathrm{kV}$

**Figure 2.3:** E versus y in Laplacian electric field with different tip radii and voltages

it can be resulted from the studies explained that the electric field varies linearly with distance. This is also in accordance with experiments of Lesaint and Top [24], which showed that different distances do not affect PDs significantly according to Equation 2.8.

## 2.3. Dielectric Liquids

A *dielectric liquid* is a liquid substance characterized by its poor conductivity of electric current. It serves the purpose of insulating electrical components and systems. The historical adoption of petroleum-based mineral oil as an insulating agent in transformers dates back to the introduction of transformer usage. In 1892, "General Electric" initiated the use of the first petroleum-based oils as insulating liquids in transformers [25]. The same reference has given a comprehensive review of the historical use of petroleum-based mineral oil as an insulating liquid in transformers and the recent focus on renewable and biodegradable alternatives.
The environmental impact of nonrenewable mineral oil is highlighted. This has led researchers to direct their attention to renewable and biodegradable alternatives.
The objective of this project is to evaluate the partial discharge (PD) behaviour of different types of transformer oils. To achieve this, two liquids representing different types of commonly used transformer oils were selected. One candidate, *Nytro 10XN*, is a mineral oil. The second candidate belongs to the synthetic ester group, known as *MIDEL 7131*.
Meanwhile, tests have also been conducted on *Cyclohexane*, a well-known stable and nonpolar liquid commonly used as a model fluid with good characteristics for spectroscopy applications.

### 2.3.1. Cyclohexane

Cyclohexane is a cyclic hydrocarbon with the molecular formula *C6H12*. It is a colourless, flammable liquid with a distinctive odour. The molecule consists of a ring of six carbon atoms, each bonded to two hydrogen atoms. Cyclohexane is a type of *cycloalkane*, which is a class of *aliphatic hydrocarbons* containing only single bonds [26].

One of the key characteristics of Cyclohexane is its stability due to its symmetrical structure. The carbon-carbon bonds in the Cyclohexane ring have a tetrahedral geometry, which minimizes the strain in the molecule and makes it relatively stable compared to other cycloalkanes with smaller or larger ring sizes.
Cyclohexane is a nonpolar liquid that does not dissolve well in water but is soluble in many organic solvents. It is commonly used as a solvent in various industrial processes, including the production of pharmaceuticals, plastics, and other chemicals. Additionally, Cyclohexane is often employed in the laboratory for reactions that require a nonpolar solvent.

While Cyclohexane is relatively stable due to its symmetrical structure (see Figure 2.4), its flammability is a property shared by many hydrocarbons. The presence of carbon and hydrogen, combined with the availability of oxygen in the air, allows for the initiation of combustion reactions. This is why hydrocarbons, including Cyclohexane, are considered flammable.

Cyclohexane is commonly used in spectroscopy for several reasons: Lack of Absorption: Cyclohexane has minimal absorption in the ultraviolet (UV) and visible regions of the electromagnetic spectrum. This property makes it suitable as a solvent for UV-visible spectroscopy, allowing accurate measurements of samples dissolved in it. High Transparency: Cyclohexane is transparent to light in the UV and visible regions, enabling clear transmission of light through the sample. This transparency is crucial for obtaining reliable spectroscopic data. Chemical Inertness: Cyclohexane is relatively inert chemically, meaning it does not readily react with most substances. This inertness reduces the likelihood of interfering chemical reactions with the sample, ensuring the integrity of the spectroscopic measurements. Low Fluorescence: Cyclohexane exhibits low fluorescence, which can be advantageous for fluorescence spectroscopy experiments. A low fluorescence background minimizes interference with the emission spectra of fluorescent samples. Table 2.3 shows Characteristics of used liquids. More details and datasheet have been given Appendix B.

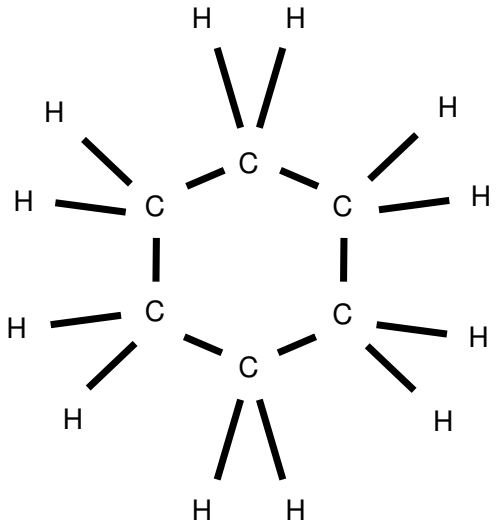


**Figure 2.4:** Cyclohexane molecule structure implemented from [27]

### 2.3.2. Nytro 10XN

*Nytro 10XN* is a naphthenic oil provided by the Swedish company *Nynas*. (see Figure 2.5) A mineral oil commonly employed in transformer insulation due to its transparent and colourless nature, consisting of various hydrocarbons [28]. Nytro 10XN is a type of mineral oil specifically designed for use in electrical transformers. Mineral oils like Nytro 10XN are commonly used as insulating fluids in transformers to help dissipate heat and prevent arcing between components [29].
Nytro 10XN is an excellent mineral oil that conforms to both *ASTM D3487-16* and *IEC 60296 Edition 5.0* boasts remarkable heat transfer properties owing to its low viscosity and viscosity index [29].
Leveraging naphthenic properties, this oil enables the transformer to initiate operation at exceptionally low temperatures without requiring the use of pour point depressants.
Meeting and surpassing stringent requirements for dielectric strength, this insulating oil delivers optimal performance when stored and handled appropriately.(see datasheet of this liquid in Appendix B)

### 2.3.3. MIDEL 7131

*MIDEL* is the world's leading brand of ester transformer fluid. Since the 1970s, MIDEL has been used in hundreds of thousands of installations worldwide [31].
MIDEL 7131 is a biodegradable synthetic ester dielectric liquid designed to provide an alternative to mineral oil, silicone liquid and dry-type transformers [32].
It has a relatively high fire point of $316°C$, significantly increasing the fire safety of transformers and reducing the need for fire protection equipment [25]. MIDEL 7131 has an extremely low pour point of $-56°C$, making it a highly effective solution in colder climates.
MIDEL 7131 has exceptionally high moisture tolerance. This characteristic enables the extension of cellulose insulation life [33]. It is currently used in a wide range of transformer applications and is proven up to $433\mathrm{kV}$. Perfectly suited for non-free-breathing and free-breathing transformers (due to their excellent oxidation stability) located indoors or outdoors [31].

In Wang's doctoral study in[33], valuable insights were gained regarding the performance of MIDEL 7131 as an insulating liquid compared to the mineral oil *Gemini X*. A significant portion of the thesis is dedicated to investigating the Partial Discharge Inception Voltage (PDIV) [33].
Employing a Needle-Sphere electrode configuration and incrementally increasing the $50\,\mathrm{Hz}$ AC applied voltage by $1\mathrm{kV}_{\mathrm{peak}}/\mathrm{step}$, both the PD repetition rate and the maximum PD amplitude were documented, as depicted in Figure A.1 in Appendix A. The electrode separation distance was 50 mm, with the spherical electrode possessing a diameter of 12.5 mm. Notably, for both Midel and Gemini X, the

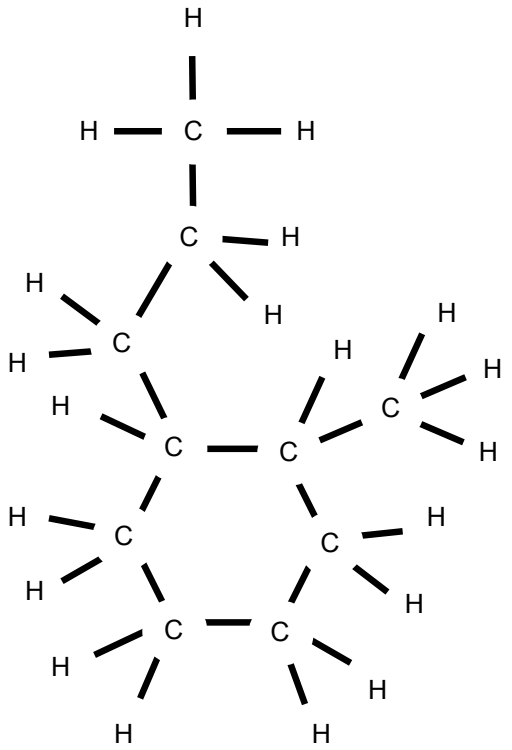

**Figure 2.5:** Naphthenic oil structure implemented from [30]

**Table 2.3:** Characteristics of the liquids

| Parameter | unit | Cyclohexane | Nytro 10XN | MIDEL 7131 |
|---|---|---|---|---|
| Relative Permittivity | $[1]$ | 1.9 | 2.17 | 3.17 |
| Conductivity | $[\mathrm{pS_{DC}/m}]$ | 2.9 | 0.60 | 23.61 |
| Density | $[\mathrm{kg/m^3}]$ | 779 | 876 | 970 |
| Viscosity | $\mathrm{mm^2/s}$ | $1.309@17°C$ | $7.6@40°C$ | $28@40°C$ |

maximum PD amplitude exhibits a similar trend across various voltage levels, demonstrating a linear increase [33, 34]. The datasheet of MIDEL 7131 is given in Appendix B.

## 2.4. Polarization of the Liquid in the Electric Field

Polarization of the insulating liquids in an electric field is not an instantaneous phenomenon. There are four different mechanisms responsible for polarization: electronic, ionic, molecular orientation, and inter-facial.
Electronic and ionic are relatively faster and instantaneous, but the latter two are slower and will take some time, from seconds to hours [35].
In non-polar liquids, the conduction relaxation time ($\tau = \frac{\epsilon}{\sigma}$) is a measure that shows how slow or fast this process can be [36].
*Electronic polarization* occurs due to the tendency of electrons orbiting more at one side of the atomic nuclei of the atom. This results in a temporary dipole effect within the atom induced by the electric field. Relative permittivity is a measure of how a material can resist the electric field compared to the vacuum. In other words, relative permittivity defines how much the material can be polarized. The permittivity of

the vacuum is a constant with a value of

$$\epsilon_0 = 8.854 \times 10^{-12} \frac{F}{m} \tag{2.9}$$

There are three phases with real and imaginary parts of the relative permittivity change with frequency that have been shown in Figure 2.6. The are three mechanisms involving these nonlinearities of the real and imaginary parts of the relative permittivity. The tree polarisation mechanisms involved from high frequency to low include atomic deformation ($\tan\delta_{De}$), then dipole orientation ($\tan\delta_{Or}$) in which the application of an electrical field encourages molecules to align. Dipoles in liquids generally rapidly orient themselves in response to the electrical field. This is while the thermic noises will reduce the dipole orientation [23] and interfacial polarization ($\tan\delta_{Pol}$).
An approximate demonstration of different effects and the change in the real and imaginary parts of the permittivity that is due to electric polarization has been shown in Figure 2.6.
Polarization is not an instantaneous effect, and there is a relaxation time after an AC voltage is applied

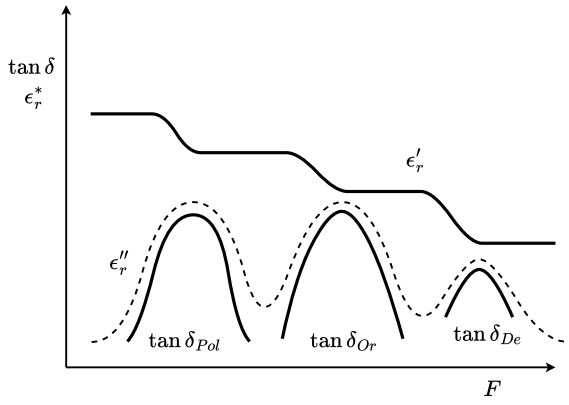


**Figure 2.6:** Approximate trend of the relative permittivity as a function of frequency

to the insulator for the dipoles to start to form from one direction and disappear from the opposite direction. This is being done with certain inertia due to the relaxation time, and when the change of the AC electric field is faster than the polarization of the material in any of the mechanisms, it results in a nonlinear trend in both components of the relative permittivity.
The connection between the electric field and displacement in an insulating material with a permittivity of $\epsilon_r^*$ may be defined as [23]:

$$D^* = De^{-j\delta} = \epsilon_r^* \epsilon_0 E \tag{2.10}$$

In which the $\epsilon_r^*$ is the complex relative permeability, it can be isolated as:

$$\epsilon_r^* = \frac{D\cos\delta}{\epsilon_0 E} - j \cdot \frac{D\sin\delta}{\epsilon_0 E} = \epsilon_r' - j\epsilon_r'' \tag{2.11}$$

where it is common to write

$$\frac{\epsilon_r''}{\epsilon_r'} = \frac{\sin\delta}{\cos\delta} = \tan\delta \tag{2.12}$$

This term has been widely used as the *Loss factor*.

## 2.5. Electric Discharge Mechanism in Liquids

discharge mechanism in the liquids includes complex interactions between electric fields, charged particles, and liquid molecules.
There are different stages in the discharge mechanism, such as initiation, avalanche ionization, formation of channel, current flow and breakdown, recombination and aftereffect. However, in this study, the main focus is on the initiation stage.
There are pivotal factors influencing electric discharge in liquids, which are:

- Type of the liquid: because different liquids have different ionization energies
- Electrode material: electrode material can affect the initiation and development of the discharge
- Electric field strength: increasing the field strength can increase the chance of ionization and formation of conductive channels
- Temperature: A higher temperature can enhance electron emission and reduce the viscosity of the liquid.
- Impurities and bubbles: The presence of impurities or gas bubbles in the liquid can provide nucleation sites for discharge

In some liquids, which primarily contain dissolved ions or electrolyte solutions like impure water, for example, upon the application of a voltage across the solution, positively charged ions (cations) migrate towards the negative electrode (cathode) and vice versa. This motion of ions causes the flow of electric current.
In metals and other conductive liquids, like mercury, free electrons are the principal carriers of charge. Meanwhile, in non-polar insulator liquids, partial discharges and, subsequently, complete discharges occur primarily due to the presence of charge carriers [1]. This region always present in gases, However it might not present in dielectric liquids [37]. Without these charge carriers, no discharge would take place in the liquid. A question might arise: What are these charge carriers, and what is their source?

### 2.5.1. Ionisation

*Ionization mechanism* in insulating liquids refers to the process by which molecules within the liquid break apart into atoms, ions, or particles. Ionization typically occurs in polar insulating liquids, where the molecules possess an uneven distribution of electrical charge, resulting in a dipole moment. When subjected to an electric field or other forms of energy, these polar molecules may separate into positively charged ions (cations) and negatively charged ions (anions).

### 2.5.2. Electron Emission Mechanism

Electron emission mechanism refers to a phenomenon where electrons are emitted from the surface of a material when subjected to certain conditions. Here are the key emission effects. Thermionic emission happens when a material is heated to a high temperature. Electrons gain enough energy to overcome the work function (the energy barrier) and escape from the surface. When the same mechanism happens by gaining energy from the electric field, it is known as *field emission*. In a strong electric field, The electrons can gain enough energy to leave the cathode and push into liquid. The required field strength is often in the order of $10^7 - 10^8\,\mathrm{V/cm}$ [38].
There are also other forms of electron emission, such as photoelectric emission and secondary electron emission. Figure 2.7 shows the field emission and field ionisation happening due to the tunnelling effect.

In [39], a model of the transformer liquid with the capability of showing the electron emission mechanism in an electrical field has been developed by using the tunnelling theory in COMSOL. the test sample used is a needle plain with $1mm$ gap. Electron density has been investigated in the gap in positive and negative voltage.

#### Tunneling Effect

As explained in the electron emission mechanism, there is an energy barrier for the electrons inside the contacts to release into the liquid, known as the work function.
Surprisingly, some electrons are emitted into the liquid, or the molecules are ionized by the field-emitting electrode to the anode without having enough energy field. This phenomenon is known as *Tunneling effect*.
The tunnelling effect is a phenomenon in quantum mechanics where particles, such as electrons, can pass through potential energy barriers even though classical physics would suggest they don't have enough energy to do so.
Classically, if a particle encounters a barrier that is higher than its energy level, it cannot pass through it and would be reflected back.

[1] charge carriers are moving charged ions and free electrons in a liquid

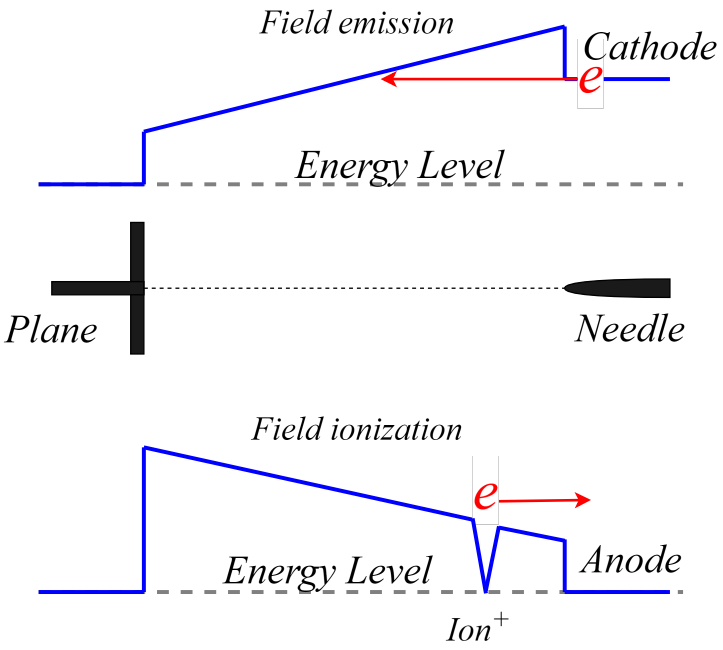


**Figure 2.7:** field emission and field ionisation happen due to tunnelling effect implemented from [23]

However, according to quantum mechanics, there is a finite probability that the particle can tunnel through the barrier, appearing on the other side without having enough energy to surmount the barrier as classically expected.

### Blocking Effect

In the needle-plane geometry, the *blocking effect* refers to the phenomenon in which the strong electric field at the needle tip causes the creation and accumulation of space charges in the region close to the needle.
These charges block the influence of the plane, and field distribution is highly localized around the needle tip. (see Figure 2.8) The blocking effect covers the electrode with a thin charged layer. Findings in [40] show that the blocking effect strongly impacts the current flow.

At higher electric fields, the conductivity is affected by ionization in the liquid. Poole-Frenkel and hopping model [41, 42] and thermionic (Schottky) injection and tunnelling (Fowler-Nordheim) mechanisms of the electrons jumping between different energy levels. These are theories explaining the mechanism of space charge forming in the liquid in the presence of a High electric field [43]. Electronic transport in organic and polymer devices, primarily light-emitting diodes. Thermal processes such as thermionic and field emission are described in [42],

## 2.6. Space Charges

Charge carriers within a dielectric liquid are named *Space Charges*. This can occur in vacuum tubes, semiconductors, or insulating materials. They play a crucial role in the discharge process. The established mechanisms for generating these charge carriers are named in [44] as:

- Electrons are emitted from the cathode by the electron emission.
- Electrons and positive ions are formed by ionization.

These mechanisms invariably result in residual charged particles remaining within a liquid. The phenomenon is mitigated by additional processes like *recombination*. These two opposing processes es-

tablish a balance of charge carriers within the liquid, where particles are in constant motion, either parallel or opposite to each other, ensuring an overall constant charge.

The quantity of these carriers may vary with temperature or electric field strength changes.
The mobility of charge carriers in a dielectric liquid is not only an intrinsic parameter of the conduction process but also very important for explaining the pre-breakdown process. The charge carriers' mobility also affects the electrostatic behaviour of fine and ultra-fine (micrometre and sub-micrometre) floated particles in the fluid [45].

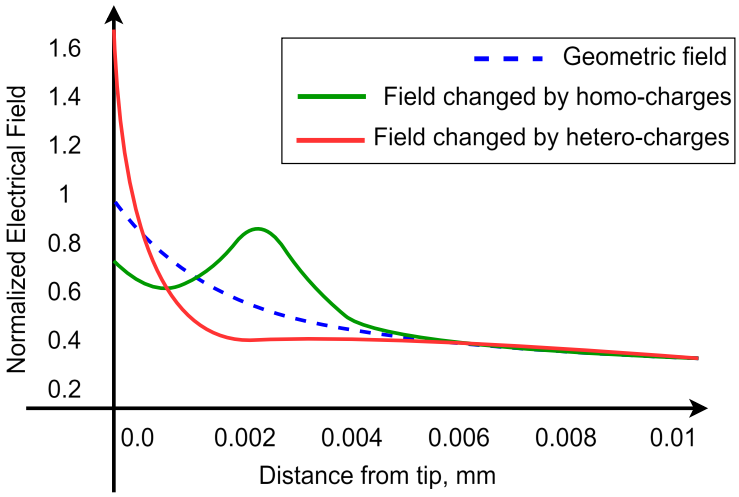


**Figure 2.8:** Effect of homocharges and heterocharges on the electric field locally. Implemented from [23]

### 2.6.1. Space Charge Limited Current

Due to the low mobility of the ions in an insulating liquid, the current is limited by the movement of the charge carriers, which are moving slower than charge carriers in gases.

### 2.6.2. Shokley-Ramo Theory

The Shockley–Ramo theorem is a method for calculating the electric current induced by a charge moving in the vicinity of an electrode [46, 47]. The Shockley-Ramo theorem states that the current flowing out of an electrode because of charge carriers is as follows:

$$i = E_\nu \cdot q \cdot \nu \tag{2.13}$$

where $q$ is the amount of charge of the charge carrier, $E_\nu$ is the electric field in the direction of movement, and $\nu$ is the instantaneous velocity.

### 2.6.3. Child's Law

Child's law was proposed by Clement D. Child in 1911 [48]. This law states that the current density due to space charge limited current (SCLC) between two parallel plane contacts of a vacuum chamber can be obtained by

$$J = \frac{4\epsilon_0}{9}\sqrt{\frac{2e}{m_e}}\frac{v^{\frac{3}{2}}}{d^2} \tag{2.14}$$

In this case, $J$ is the current density, $d$ is the distance between the cathode and anode, $e$ is the amount of the charge of an electron, and $m_e$ is the mass of an electron.

### 2.6.4. Drift Regime (Mott-Gurney's Law)

A more general form of the Child's Law that gives the current density between two plane contacts with an insulating material as a medium is Mott-Gurney's law [49, 50].

$$J = \frac{9}{8}\epsilon\mu\frac{V^2}{d^3} \tag{2.15}$$

Where $J$ is the current density, $L$ is the thickness between two contacts, $\epsilon = \epsilon_0 \cdot \epsilon_r$ is the permittivity, $V$ is the applied voltage, and $d$ is the distance between contacts. $\mu$ is defined as electrical mobility or charge carrier mobility in Mott-Gurney's law. Frenkel's model for fixing the reduced form of Mott-Gurney's law is accessible at [50].
Electrical mobility ($\mu$) is related to the strength of the field ($E$) and drift velocity ($\nu_d$), which is defined as:

$$\mu = \frac{\nu_d}{E} \tag{2.16}$$

A charged particle in gas or liquid will accelerate in a uniform electric field until it reaches a certain speed. This speed is defined as drift velocity.

Electrical mobility is proportional to the net charge of the particle. It is inversely proportional to the Stokes radius of the ion. Considering a charge density of $\rho_0$ of the residual charge carriers in the region[2]. From Shockley-Ramo theory, The current density of charges with a charge density of $\rho_0$ of residual ions is as follows [23]:

$$j_0 = \rho_0 \mu \frac{V}{d} \tag{2.17}$$

By comparing two equations Equation 2.17 and Equation 2.15 a condition can be resulted as:

$$\frac{d^2}{V} > \frac{\epsilon \mu}{\sigma} \tag{2.18}$$

In which $\sigma$ is the conductivity of the liquid. this inequality shows a condition in which the SCLC is limiting the flow of charges between contacts. Therefore, the relation between the electric field strength and conductive current[3] changes from linear to nonlinear when this condition applies.
It is important to note that this inequality is based on the plane-plane geometry. However, it can give a good perspective on the relation of conductivity with space charge limited current.
The current density resulting from the drifting of charged particles can be calculated from the mobility.

$$J = en\mu E \tag{2.19}$$

In which $n$ is the number of charged particles, Ohm's law can be written in the form of

$$J = \sigma E \tag{2.20}$$

where conductivity is

$$\sigma = en\mu \tag{2.21}$$

### 2.6.5. Influence of Space Charges on the Electric Field

The electric field is not only affecting the movement and presence of space charges in the gap, but space charges also affect the electric field locally [51].
The maximum electrical field at the needle tip is enhanced in the presence of heterocharges and reduced slightly by homocharges.
The following formula has been suggested by Atten [52] for the point-plane geometry in the presence of space charges:

$$E_{th} = \frac{2V}{r_0 ln(\frac{4d}{r_0})} - \left(\frac{\eta I}{8\pi\epsilon^2}\right)^{0.5} \int_0^d \frac{g(x)}{\sqrt{E(x)}} dx \tag{2.22}$$

In this equation, the influence of the charge $Q(x)$ has been defined as $g(x)$, and $\eta$ expresses the dynamic viscosity. There is no practical way to measure $g(x)$; therefore, the electric field's quantitative evaluation is impossible.

[2] The active region with extremely high electric field around the needle tip
[3] Conductive current: The AC component of the current waveform which is in phase with voltage

## 2.7. Conductive Current in Dielectric Liquid

One of the significant phenomena resulting from the motion of space charges in a dielectric liquid is conductive current. However, the initial step in understanding this is knowing the conductivity in dielectric liquids.
The current flowing between two contacts connected to a high-voltage AC is almost always leading in phase. If it is modelled by a capacitance, which is not far from the nature of an insulator, then based on the polarization theories in section 2.4, the complex capacitance of the test liquid and loss factor relation with capacitive and conductive current values are as follows:

$$\begin{aligned} \bar{C} &= (\epsilon_r' - j\epsilon_r'') \cdot C_0 \\ \tan(\delta) &= \frac{1}{R\omega\epsilon_r' C_0} + \frac{\epsilon_r''}{\epsilon_r'} \\ \tan(\delta) &= \frac{I_r}{I_c} \end{aligned} \tag{2.23}$$

The capacitive component of the current ($I_c$)is due to different mechanisms of polarization. The resistive or conductive component of the current ($I_r$)is primarily associated with space charges and SCLC within the liquid. in other words, the conductive part of the current, which is in phase with voltage, is markedly influenced by both the number of space charges and their mobility.
The general form of the conductivity characteristics for gases and dielectric liquids for a plane-plane electrode geometry may be presented as in Figure 2.9 according to the molecular configuration of liquids [37].

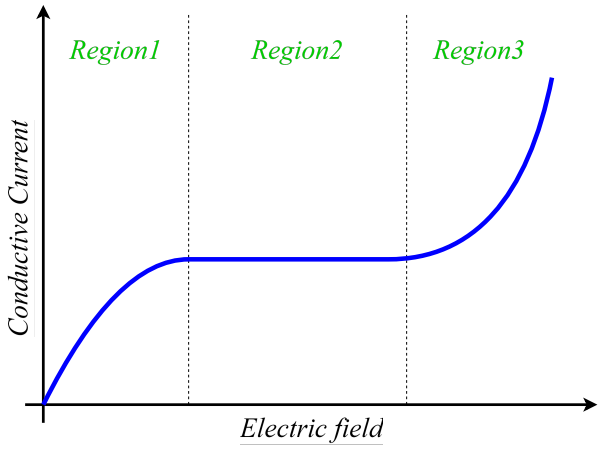


**Figure 2.9:** General relationship between current and field strength for liquid dielectrics. Implemented from [35]

It comprises three regions. Region 1 in which the liquid primarily exhibits Ohmic behaviour. At low electric fields, the conductive current has a linear relation with the electric field.

Region2 is around $1\,\mathrm{kV/cm}$ to $10\,\mathrm{kV/cm}$. Another name for this region is a subohmic region. It demonstrates that most ions in the insulator have been depleted due to electric field stress. However, this stress isn't sufficient to cause ionization in the insulator. Thus, there are no additional charge carriers formed. As a result, the current is saturated by increasing the voltage stress.

A source of charge carriers must exist for a continuous current to flow through the liquid. In the ohmic and subohmic regions, natural ionization of ionic impurities (uncontrolled chemical impurities) can be presented as the charge carriers [37]. The simplest assumption of these impurities is to consider them as ion pairs moving freely inside the liquid.

In Region 3, a new source of charge carriers emerges in the insulator liquid. This corresponds to ionization, occurring at higher voltage stresses, and is characterized by an exponential relation. At higher field stress, the current increases rapidly and at $40 - 100\mathrm{kV/cm}$, a breakdown may occur [37].

There are two standards used for measuring conductivity in liquids for electrotechnical purposes. IEC 61620 recommends applying a low-frequency square voltage, resulting in a field below $0.1\,\mathrm{kV/mm}$. On the other hand, IEC 60247 [16, 53] utilizes an AC voltage, leading to an applied field ranging from $0.05$ to $0.25\mathrm{kV/mm}$.

In [23], different liquids have been tested under sinusoidal AC high voltage (below PDIV) with low frequency ($0.1\,\mathrm{Hz}$) and a pulse waveform with $50\,\mu\mathrm{s}$ duration. The results for the AC voltage tension show different behaviour between the positive and negative sides of the cycle, which has been explained to be because of the lower barrier for injection of electrons other than an injection of holes [23]. It also has been explained that this level of conductivity, in theory, leads to a non-physical electric field to obtain from $j = \sigma \cdot E$; therefore, there must be homocharges in the vicinity of the tip to lower down the field to a lower value.

Distinguishing between bulk ionization and electrode emission phenomena can be challenging, especially in higher fields. Nonetheless, experimental observations indicate that at low fields, bulk liquid Ionization due to Thomson-Onsager phenomena is dominating.
On the other hand, for higher fields, the main source of current carriers is due to ion injection from the interfaces [54].

### Low Field

By increasing the voltage, charge carriers move relatively to the applied field. In a liquid at thermodynamic equilibrium, conductivity depends on the number of charge carriers [23]. The ohmic behaviour is up until the ion transport time exceeds the relaxation time. (ionic relaxation time which is $\tau = \frac{\epsilon}{\sigma}$.
After the whole charge carriers have been swept out of the bulk volume, the current will no longer increase proportionally to the voltage [23], and there will be a nonlinear saturation trend between conductive current and applied electric field (Region 2 in Figure 2.9. Accumulation of these charges around the one contact additionally, affects the electric field, lowering it down than the Laplacian field. (see subsection 2.6.5)
The current density in the plane-plane geometry can be obtained by the following relation

$$\epsilon_r \epsilon_0 \frac{dE}{dx} = \rho(x) \tag{2.24}$$

In which $\rho$ is the charge density in 1 dimension, $E$ is the electric field. Considering Mott-Gurney's law (Equation 2.15), conductive current can be described as [54] :

$$I^{0.5} = K(V - V_0) \tag{2.25}$$

$$K \approx 1.06\sqrt{\frac{\epsilon\mu}{d}} \tag{2.26}$$

$$V_0 = 0.5 E_p r_p ln(\frac{4d}{r_p}) \tag{2.27}$$

Where $V$ is the applied voltage and $V_0$ is the threshold voltage, While $\epsilon$ and $\mu$ are permittivity and mobility, and $E$ is the electric field of the needle. $d$ is the needle-plane distance. There is no better model available for the needle-plane geometry currently to predict the electric current in high electric fields ($> 5.10^4\mathrm{V/mm}$)

### High Field

The conductivity at the higher fields has been observed to increase exponentially with the electric field. This is due to the formation of new space charges in the region. Results from the impulse voltage show a linear increase of charges during the voltage pulse, suggesting the high rate on initial charge carriers followed by drift; however, it's not the case for all of the liquids in all polarities.
A threshold has also been obtained for the space charge limited current. The threshold is likely to be

linked with charge injection [23]. In another way, for the mobility of the charge carriers, the calculated mobility speed for the sinusoidal voltage has been lower than the calculated one for the pulse voltage by an order of magnitude.
It has been explained in [23] that under AC, there is a slow formation of local charges during a long sequence, whereas for the pulse voltage, this charge formation is counter-balanced with the charge drift that is established momentarily. This has been the main cause of the higher conductivity in a specific electric field over time.
Even though the microscopic electric field is below what is expected for the electron process, the local field at the molecular level can be higher than the Laplacian field [23]. The exact field is also dependent on the molecular orientation in the electric field [55, 56].

## 2.8. Partial Discharge

As defined by IEC 60270, a *Partial Discharge* (PD) is a localized dielectric breakdown of a portion of a solid, liquid or gaseous electrical insulation system under high voltage (HV) stress, which may or may not occur adjacent to a conductor [57].
Major insulation breakdowns in gaseous, liquid or solid insulation are usually initiated by partial discharges. Thus, knowing the partial discharge phenomena gives a lot of information about assessing the dielectric strength of the liquid [44]. One theory about PD formation is the concentration of charges, which increases at one point, causing an increase in temperature. This high temperature may cause *micro-bubbles* or electron avalanches to form within the insulating, which is a mechanism suggested by J.Lehr. it is more likely that PD starts within these micro-bubbles [58].
However, new findings also strengthen the second theory that the electron avalanche formation is prior to micro-bubble creation, as the previous theory can not explain the large difference between positive and negative polarity.

PDs are inherently a stochastic phenomenon. Thus, it is important to consider the PD probability distribution. Given their random nature, individual PD events lack straightforward fixed parameters for prediction. It is notable that numerous small negative PDs exist alongside a limited number of large positive PDs. This observation indicates an inherent asymmetry in the PD phenomenon [23].

## 2.9. Electrical Measurement of the PDs

The electrical circuit for detecting PD functions is based on a fundamental principle known as the ABC-equivalent model [34] or PD measurements based on charge acquisition. In this model, a void within the insulation is represented by a small capacitance, $C_c$, connected in series with a larger capacitance, $C_b$, symbolizing the insulation between the void walls and the electrodes. The remaining insulation is represented by $C_c$, which exhibits the highest capacitance. This ABC-equivalent circuit is illustrated in Figure 2.10.

Through voltage division, the voltage across the void ($V_c$) follows the applied voltage but is reduced by a factor determined by $\frac{C_b}{(C_b+C_c)}$. If the applied voltage surpasses the withstand capability of the void, a local transient current flows between its walls, marking the onset of partial discharge, known as the *partial discharge inception voltage* (PDIV). The voltage corresponding to this event over the void is termed the ignition voltage. Upon discharge, $V_c$ rapidly drops to nearly zero. To counteract this voltage drop, the external circuit delivers a transient current to the test object, denoted as $I$ in Figure 2.10. Typically, this charge injection is primarily supplied by a relatively large *coupling capacitor* ($C_x$) connected in parallel with the test object. The charge carried by $I$, known as the apparent charge, can be detected by placing a suitable *measuring impedance* ($Z_M$) in series with the coupling capacitor. It is an apparent charge because it doesn't directly represent the actual discharge current within the void but is proportionate to it and can be calculated through proper calibration [59, 60].

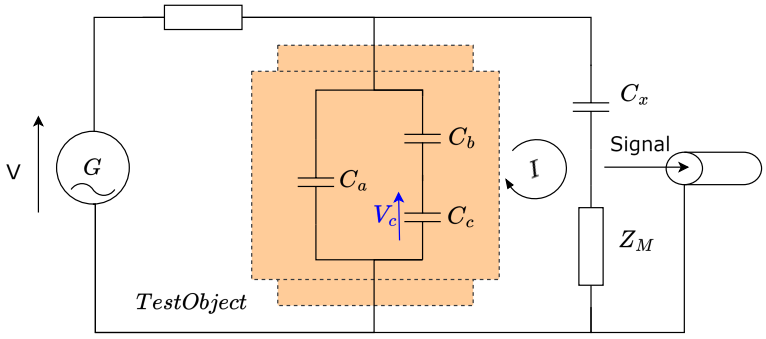


**Figure 2.10:** the ABC-equivalent circuit

## 2.10. Definition of PDIV

The PDIV concept, or Partial Discharge Inception Voltage, isn't a straightforward threshold because it also depends on time, with several definitions existing. These definitions also vary depending on whether the measurement is conducted under DC or AC voltage regimes. Experiments in [61] demonstrate that PDIV voltages differ based on the criteria used, making it challenging to establish a single meaningful threshold for assessing the quality of insulating liquids. To address this, a specific definition for PDIV testing is necessary.
A simple definition of partial discharge inception voltage can be the voltage at which partial discharge starts. However, since partial discharge is a random phenomenon, it is related to the chances of happening at some voltage level. In other words, the chance of a partial discharge incident increases by an increment of the voltage, but there is no exact point for starting the partial discharges. Giving more time to the insulator liquid under test will also increase the chance of a PD incident happening. Therefore, a clear definition of PDIV voltage should be taken. It should be accurate and repeatable.
In the previous works in the master thesis by Skirbekk [62]. Her definition of the PDIV was the voltage step in which the first PD happens. The voltage has been increased stepwise by $V_{peak} = 1\mathrm{kV}$ per step, and the length of each step was 1 minute.

In another study by Fagerli [34], PDIV has been defined as a chance of a PD incident by considering the PD repetition rate versus voltage.
However, the IEC has defined the PDIV differently, which is explained in subsection 2.1.1.

## 2.11. Needle Tip Erosion Over Time

The tip radius of the needle is not constant when it is being tested under HV tension. Previous studies show that the needle becomes dull over time, and, therefore, a time-dependent electrical field is created between the needle-plain area [23].
T.G.Aakre has quantified the rate of change of the needle tip radius over time for a tungsten needle at $d = 20\mathrm{mm}$ in MIDEL 7131 under $18\,\mathrm{kV}$ voltage as a function of time by fitting a cubic root function in the form of Equation 2.28 to the test results.

$$r_p(t) = \sqrt[3]{\frac{3A}{2\pi}t} \tag{2.28}$$

And the calculated value of the constant in [23] is:

$$A \approx 400\frac{\mu\mathrm{m}^3}{\mathrm{h}} \tag{2.29}$$

## 2.12. Light Emission From PD

Energy is released in electron avalanches during the partial discharge. This energy can transform into the form of heat, light, and sound. The heat release during the PD has been shown by Lesaint et al.

[63]. Lundgaard et al. showed that streamers also emit light [64]. The source of light emission from PD is the recombination process. However, the light spectrum of different types of discharge is not the same [65]. In addition to that, The spectrum of surface discharges along a solid dielectric is more complex and influenced by many factors such as solid material, surface condition, and the composition of material [66]. Transformer oil exhibits emission in the range from $350\,\mathrm{nm}$ to $700\,\mathrm{nm}$, depending on oil composition. (Figure 2.11) The emitted light's frequency is predominantly formed by hydrogen and hydrocarbon mixtures such as Methane, Ethane, and Ethyl [65].

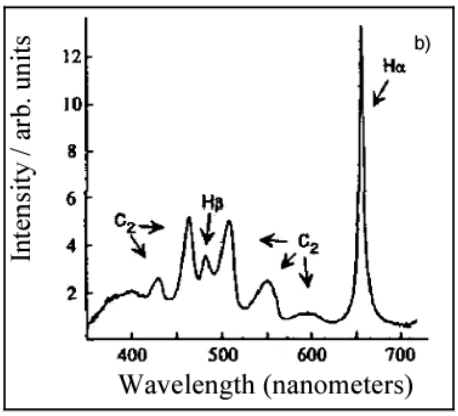


**Figure 2.11:** Typical emission spectra, discharge in liquid. Adopted from [65]

A small fraction of recombination energy ($\approx 1\%$) is emitted as light in gasses; for liquids and solids, the fraction is even smaller [67]. The amount of the emitted light and its frequency depends on the type of the material (gas, liquid) and other factors like temperature or pressure. Therefore, the spectrum of the emitted light from the PD extends from ultraviolet over the visible range to infrared [65]. Different optical PD detectors can be used depending on the wavelength and the strength of the light emission. Common optical systems for this purpose are UV corona scopes, night vision cameras, low-light enhancers, photo-diodes, and photo-tubes.
The categories of detection are also important: imaging, quantitative, or non-imaging detection sensors. In [65], M.Muhr used two approaches for measuring the light emission from PD of a needle-plate configuration in transformer oil. The voltage range is from $0\,\mathrm{kV}$ to $100\,\mathrm{kV}$, and the distance between the needle and plane is adjustable in the range of $1 - 20\mathrm{cm}$. The oil is at the normal pressure, and the experimental setup is in a darkened and shielded HV chamber. Experiments have been done by two arrangements. The first arrangement is called Fluorescent optical fibre, in which the needle is positioned perpendicular to a fluorescent optical fibre, which is attached to a conventional optical fibre and then to the sensor. In the other arrangement, which is called a lens, a lens is attached to the end of a conventional optical fibre, and the needle is placed in front of the lens at a distance called the observation area. This PD detection method is tested using air as a medium and compared with the conventional method, which has been proven to be correct. After that, it was used to measure the PD in oil. The detected discharges in oil have been reported to be scattered in amplitude and shape, and positive streamers have shown a superposition of fast pulses of growing intensity. The obtained results are shown in Figure A.2 in Appendix A.
The results show that the electrical PD measuring system is not fast enough to show the fast PD impulses happening in oil due to limited bandwidth.
Schwarts et al. also show that different spectral regions of the radiated light are absorbed from different magnitudes of PDs. (Figure A.3 in Appendix A)

# 3

# Methodology

## 3.1. Measurement Setup

The nonuniform electric field can be found in electrical installation. The electric field can increase intensely at the sharp edges of the busbar and sharp conductors at the HV side in transformers. The localized strong electric field facilitates the localization of PD events. Therefore, The needle-plane configuration has been selected to produce a nonuniform electric field.
The needle-plane setup offers a known electrical field distribution, making it preferable for studying PD mechanisms. However, in the IEC 61294 standard, a needle-sphere geometry has been suggested for PD inspection, which is explained in subsection 2.1.1.

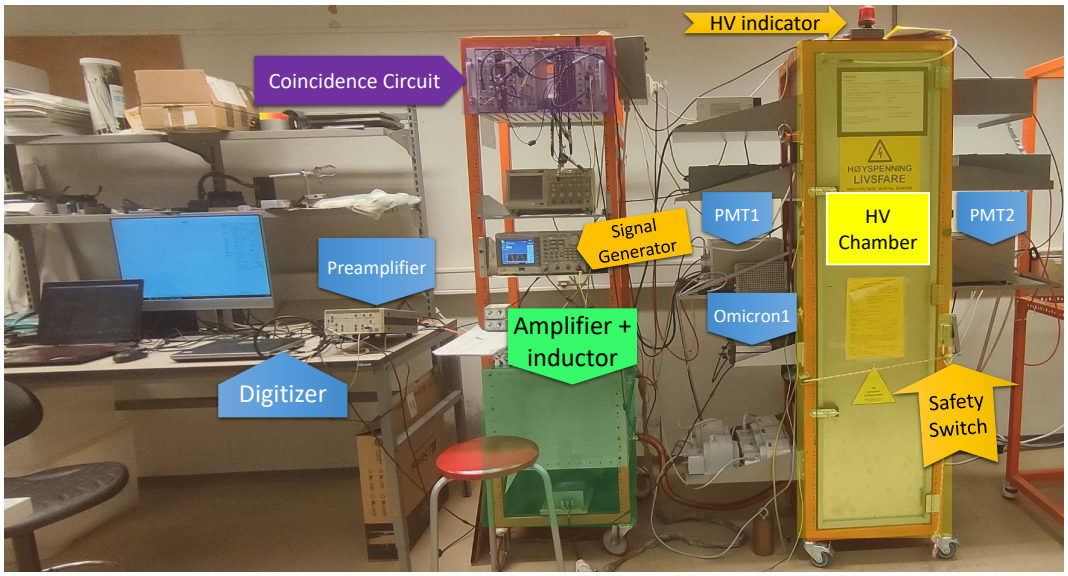


**Figure 3.1:** The photo of the test setup with placement of different parts

Furthermore, The measurement instruments were susceptible to electrical interference by the electric wiring system, but previous studies helped for proper shielding and filtering of the PD signal [23].
Therefore, the test cell is positioned within a Faraday cage to adequately shield it from external influences. A sinusoidal AC voltage of up to $22\,\mathrm{kV}$ is applied to the plate, and the needle has been grounded. Figure 3.1 demonstrates the full setup arrangement and Figure 3.2 shows the inside of the HV chamber. The equivalent electrical circuit of the test setup has been shown in Figure 3.4.

### 3.1.1. Setup Description and Safety Precautions

The test setup comprises an enclosed chamber housing a step-up transformer at its lower section. (High voltage source in Figure 3.2) Using a chamber to isolate the complete HV parts minimized electromagnetic noise and light interference.
All corners of the chamber have been sealed with conductive tape, and all incoming cables used grounding shields, but making current loops has been avoided.
Inside the HV chamber in Figure 3.2, the test cell (test sample) can be conveniently mounted and dismounted on the upper side of the chamber. The test cell (test sample) has been placed on an insulated plastic mount. The lower side of the test cell has been connected to the capacitors $C_1$ and $C_2$, which are connected to the electrical PD measurement device using an ABC circuit (see section 2.9 and section 3.2). It has been shown in Figure 2.10 as $C_x$.
There is also a manual grounding device for safe visible grounding while working in the HV chamber. There are also two micro switches and a semi-automatic grounding system attached to different parts of the door of the HV chamber to automatically disconnect the high voltage feed and connect ithe high voltage arm to the ground when opening the door.
The entire high-voltage connection inside the HV chamber has been made by using round brace rods with $r_b = 1\mathrm{cm}$ that are screwed together for the least possible PD. A shielded coaxial cable connects the

needle to the preamplifier through a safety gas fuse (EMP protector) and two voltage-sensitive diodes (protection diode) to limit the voltage on the measuring side in case of a breakdown inside the test cell. (see Figure 3.3)

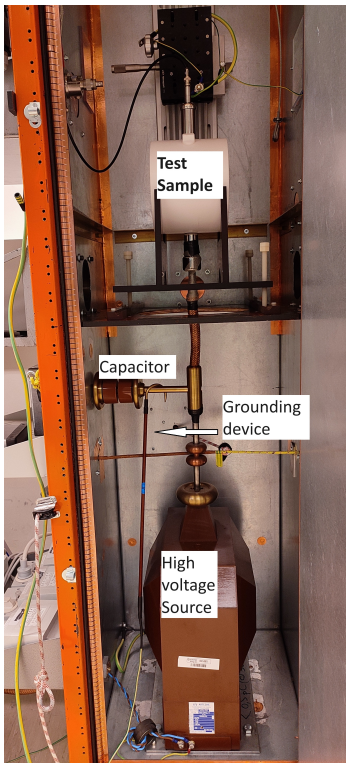


**Figure 3.2:** Inside HV chamber of the test setup

### 3.1.2. AC Voltage Circuit

The *Tektronix AFG3052C* signal generator is utilized to generate a pure sine wave with the desired frequency and amplitude for the test. This pure sine wave is directed to a voltage amplifier, and the output feeds an AC transformer.
This transformer has been labelled in Figure 3.3 as an Isolation transformer because it galvanically isolates between the two parts of the circuit. Subsequently, it is supplied to a single-phase step-up HV transformer. (see Figure 3.1 and Figure 3.3)
This section of the circuit operates primarily based on resonance between the capacitance of the high-voltage segment and the inductors added to the primary winding of the final step-up transformer. (see Figure 3.3)

## 3.2. Discharge Acquisition System

The discharge acquisition system is a system based on an ABC circuit, which has been explained in section 2.9. This system comprises two optically connected parts. The used device has different modules such as *MPD600, MPP600* and *MCU502, CPL542* along with two known capacitors $C1 = 1700\text{pF}$ and $C2 = 1700\text{pF}$ which are part of a capacitive voltage divider with the capacitance inside CPL542. Characteristics of the CPL542 are given in the Table 3.1. This system quantifies current and calculates charge through numerical integration. It is specifically optimized to provide precise measurements of the number and magnitude of partial discharges.

The device enables data storage and the generation of histograms depicting the magnitude and phase of PDs over extended time periods. It is known for its q(v) measuring for the PDIV. The Omicron PD measuring system diagram from its user manual has been illustrated in Figure 3.5. Two discharge

acquisition systems have been used during experiments, which are named *Omicron1* and *Omicron2*; therefore, these names have been used for the 1discharge acquisition system in the next parts.

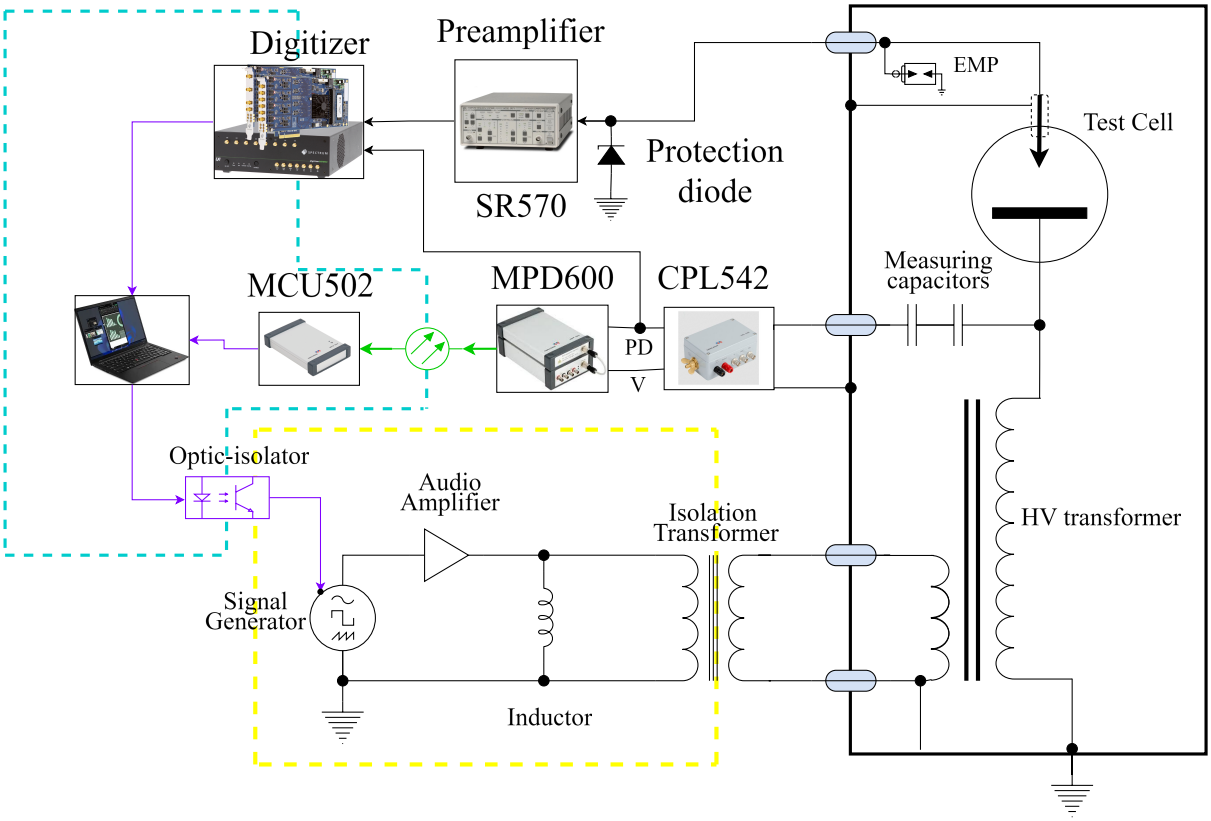


**Figure 3.3:** Test setup diagram for AC test setup with charge acquisition and current measurement

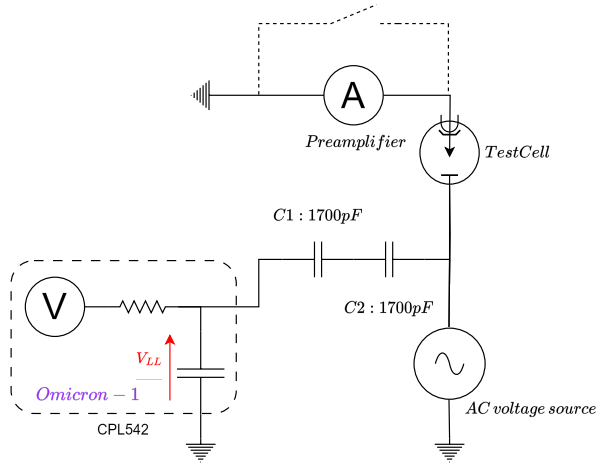


**Figure 3.4:** Equivalent circuit of the test setup

The expected low-arm voltage has been calculated based on the given information in Table 3.1. Since the highest possible voltage on the low arm is important, The lowest capacitance has been taken into account.

$$V_L = V_{AC} \cdot \frac{C_{measure}}{C_{CPL542} + C_{measure}} \tag{3.1}$$

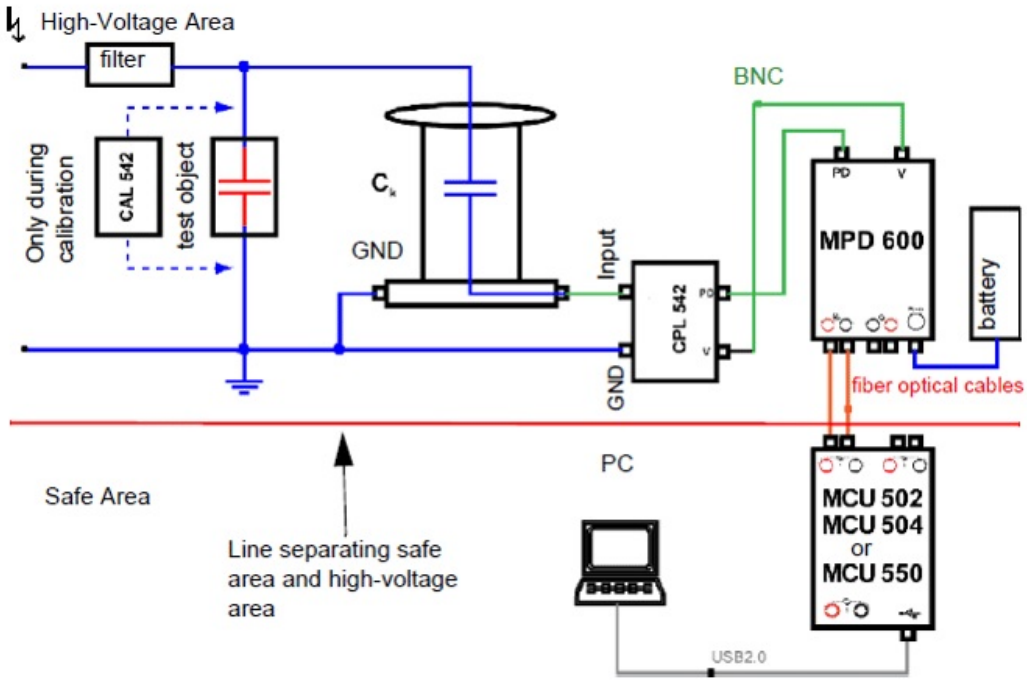


**Figure 3.5:** Electrical measurement diagram of omicron PD measurement system adopted from [68]

Considering the Highest peak voltage for the test and smallest capacitance available for CPL542, the low voltage side of the capacitive voltage divider is calculated in Equation 3.2

$$V_L = 25000 \cdot \frac{850 \times 10^{-12}}{850 \times 10^{-12} + 30 \times 10^{-6}} = 708\text{mV} \tag{3.2}$$

This voltage is in the range for the CPL542.
The diagram of the rectified AC test setup with two omicron measuring devices and current measurements has been shown in Figure 3.8.

**Table 3.1:** CPL542 Types and characteristics

| MAX Current | 0.5A | 2A | 5A |
|---|---|---|---|
| Low-arm capacitance | 30 µF | 120 µF | 272 µF |

### 3.2.1. Calibration of the Omicron

For correct PD measurement with Omicron, calibration is necessary. a calibration charge injector shown in Figure 3.6 has been used for this purpose. The trigger source has been set to $f = 50\text{Hz}$. then the amount of charge has been set to $q = 20\text{p}$ and the adjacent frame in the Omicron software under Q-tab>calibration settings>QIEC(target) has been set to the same value. The calibrator contacts have been connected between the HV part of the circuit and the ground of the HV. During calibration, the safety grounding connection has been temporarily disconnected from the HV part.

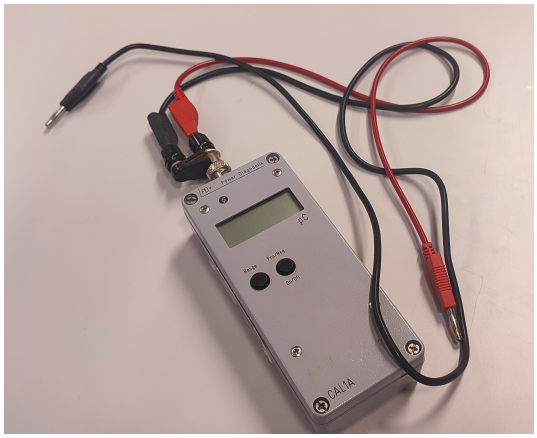

**Figure 3.6:** Calibrating charge injector

### 3.2.2. Rectified Half-cycle Voltage Source

To have a deeper understanding of the nature of space charges and test the polarity of the space charges, some tests have also been taken with half-cycle high-voltage AC. Some modifications have been made to the test setup to make the new waveform. Waveform has been mainly rectified by an HV diode. A resistor has also been added to it to control the output voltage of the diode. After the diode, another set of Omicron measurements has been added to the upper side of the high voltage. The equivalent circuit of the modified test setup has been shown in Figure 3.7.

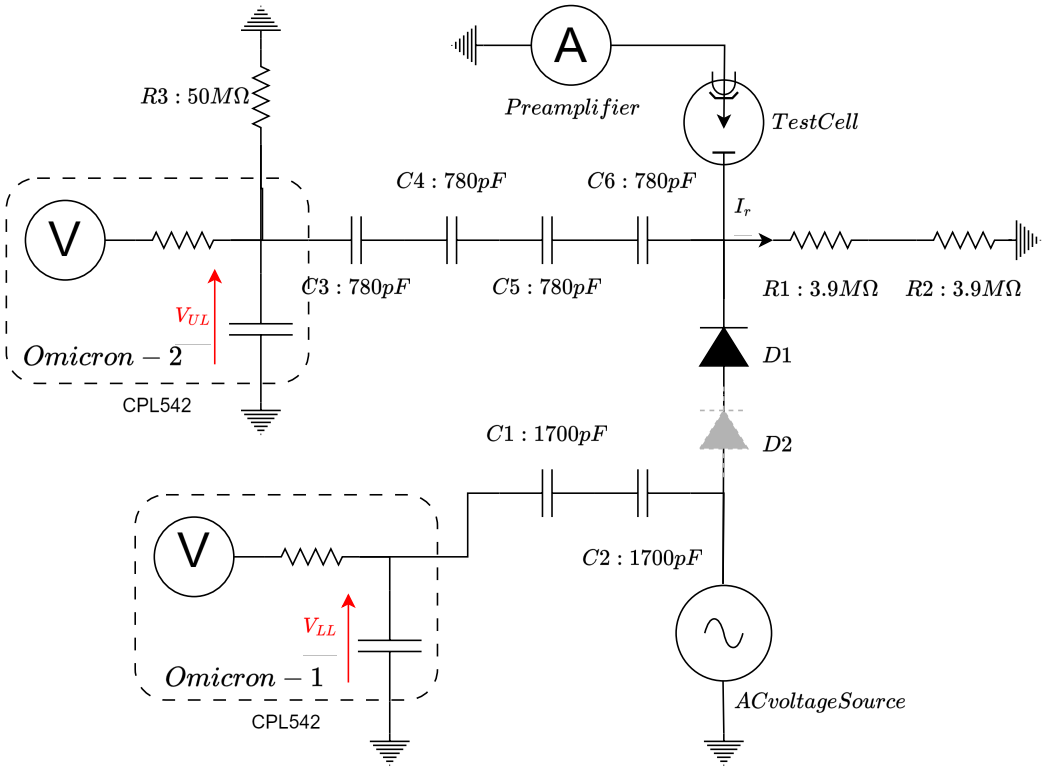


**Figure 3.7:** Equivalent circuit of the test setup for half-cycle test

The characteristics of the components shown in Figure 3.7 have been given in Table 3.2.
The voltage at the Omicron side of the capacitive divider in the upper Omicron device has been calcu-

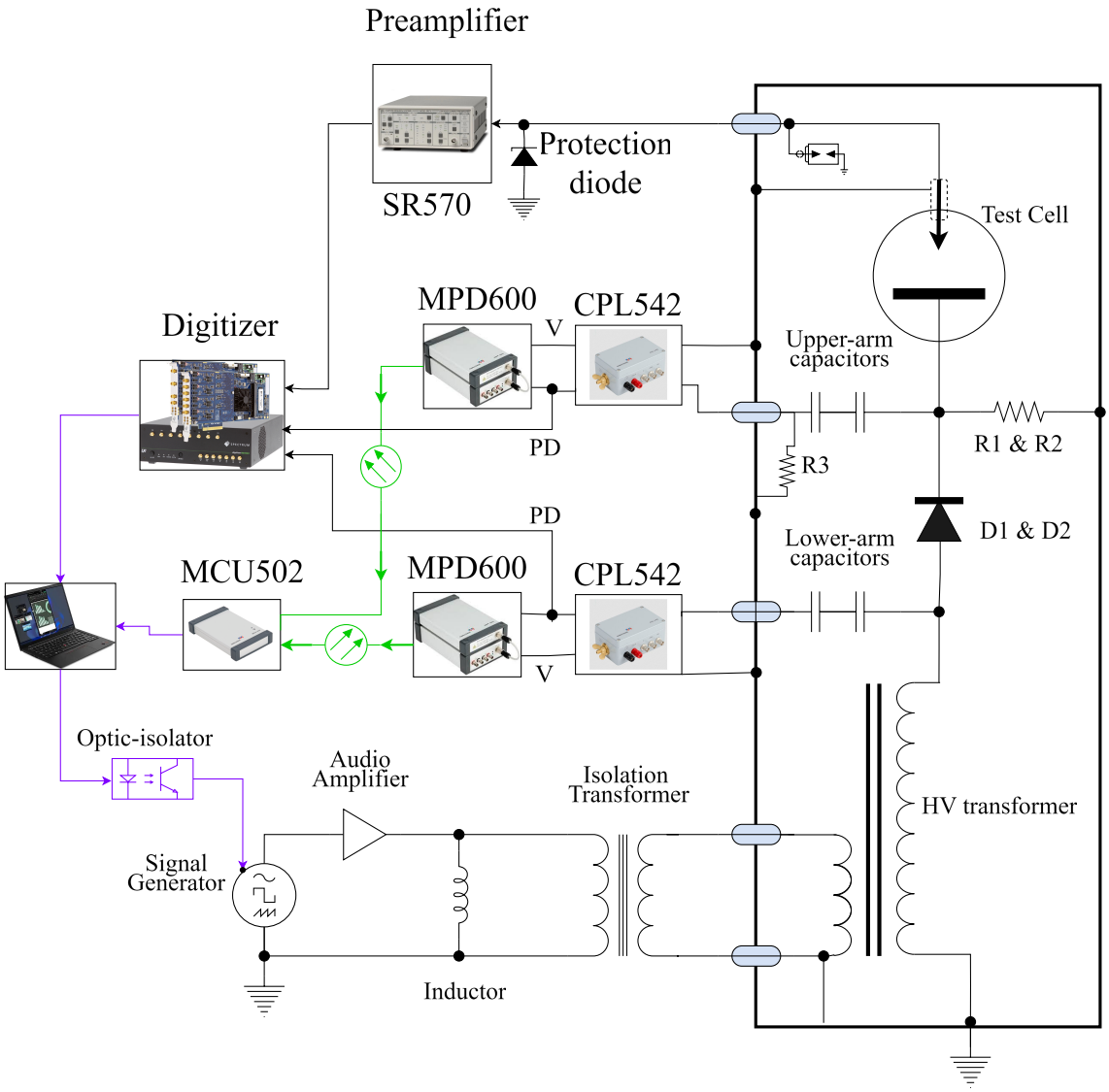


**Figure 3.8:** Test setup diagram for rectified AC test setup with two omicron devices and current measurement

lated for the worse case in Equation 3.3

$$V_L = 25000 \cdot \frac{780 \times 10^{-12} \times \frac{1}{4}}{780 \times 10^{-12} \times \frac{1}{4} + 30 \times 10^{-6}} = 162.5\text{mV} \tag{3.3}$$

Therefore, the voltage is in the range for CPL542 in the upper arm. because the voltage of the lower side of the voltage divider is relatively small; therefore, it might be vulnerable to noise [38].
The next important quantity to be calculated is the max current through $R1$ and $R2$ and dissipated power. Therefore, the half-cycle's root mean square voltage needs to be calculated to obtain power.

**Table 3.2:** Details of the elements in Figure 3.7

| # | ID | Component | Name | Characteristics |
|---|---|---|---|---|
| 1 | D1,D2 | High Voltage Diode | $UGE3126AY4$ | $V_{RRM} = 24\text{kV}$, $I_F = 0.8\text{A}(air\ self\ cooling)$, $V_F = 15\text{V}$ |
| 2 | R1,R2 | High Voltage Resistor | $MG815 - 3.90MEG - 1\%$ | $R = 3.9\text{M}\Omega$, $V_{MAX} = 30\text{kV}$, $P_{MAX} = 15\text{W}$ |
| 3 | R3 | High Voltage Resistor | $HTE152 - 50M\Omega$ | $R = 50M\Omega$, $V_{isol} = 45\text{kV}$, $P_{MAX} = 15\text{W}$ |
| 4 | C3,...,C6 | High Voltage Capacitor | $780C40DKT78$ | $C = 780\text{pF}$, $V_{DC} = 40\text{kV}$, $tan\delta = 20 \times 10^{-3}$ |
| 5 | C1,C2 | High Voltage Capacitor | $UHV - 12A - 172K$ | $C = 1700\text{pF}$, $V_{DC} = 50\text{kV}$, $tan\delta = 0.1\%(max)$ |

$$
\begin{aligned}
V_{RMS} &= \sqrt{\frac{1}{\tau}\int_0^{\tau} V^2(t)dt},\ V = V_P sin(\omega t) \\
&= \frac{V_P}{\sqrt{\tau}}\sqrt{\int_0^{\frac{\tau}{2}} sin^2(\omega t)dt} \\
&= \frac{V_P}{\sqrt{2\tau}}\sqrt{\int_0^{\frac{\tau}{2}} 1dt - \int_0^{\frac{\tau}{2}} cos(2\omega t)dt} \\
&= \frac{V_P}{\sqrt{2\tau}}\sqrt{\frac{\tau}{2} - \frac{1}{2\omega}(sin(\omega\tau) - 0)} \\
&= \frac{V_P}{\sqrt{2\tau}}\sqrt{\tau - \frac{1}{2\pi f}(sin(\omega\tau))} \\
&= \frac{V_P\sqrt{f}}{2}\sqrt{\frac{1}{f} - \frac{1}{2\pi f}sin(2\pi)} \\
&= \frac{V_P}{2}
\end{aligned}
\tag{3.4}
$$

Based on Equation 3.4 if the maximum possible voltage is considered $V_p = 25\text{kV}$, then the continuous current flowing through resistor R1 and R2 is as follows

$$I_{R1,R2} = \frac{V}{R1 + R2} = \frac{12.5kV_{RMS}}{7.8M\Omega} = 1.60\text{mA} \tag{3.5}$$

The maximum power dissipation capability of $R1$ and $R2$ in continuous mode has been given in Table 3.2 by calculating the maximum dissipated power and comparing it with Table 3.2

$$W_{R1,R2} = RI^2 = 3.9M\Omega \cdot (1.60mA)^2 = 9.95\,\text{W} \tag{3.6}$$

It is in the range of allowed continuous power dissipation in resistors. The next parameter to consider is the time constant of the resistor $R1$ and $R2$ with $C3, ..., C6$ and the capacitance of the test cell. Later from The next quantity is the power quality or the power factor of the connected load to the diode. Considering Figure 3.7, the load connected to the diode is a resistive and capacitive load. The power factor of this load is an important quantity that can change the output waveform. The output will be pinned to the maximum in the large capacitive loads; Therefore, the load should be kept resistive with a low time constant to produce the desired waveform. Considering the voltage to be at maximum value of $V_{rms} = 12.5\text{kV}$

$$I_R = \frac{V_{RMS}}{R} = \frac{12500}{3.9M\Omega \times 2} = 1.6\text{mA} \tag{3.7}$$

It should be explained here that the range for the capacitive current flowing in the test cell can be calculated by simulating the test cell and obtaining the capacitance value in $50\,\mathrm{Hz}$. But since, at this stage of the work, the setup was made and the test cell was already tested in full cycle mode therefore, the range of the capacitive current was known.

$$I_C \approx 20\mu\mathrm{A} \implies Q = \frac{I_R}{I_C} = 80 \tag{3.8}$$

The electrical behaviour of the test cell will be explained in the next section. based on the explanation in section 2.4 and Figure 2.9, it is easy to understand that the test cell can be considered as a capacitance in parallel with a nonlinear resistance and the quality factor shows that the capacitance is larger. therefore, the test cell has been approximated as only a capacitance, and the value is obtained from the results of the practical experiments over the full-cycle AC setup.

$$C \approx 195\mathrm{pF} \implies \tau = R \times C = 2 * 3.9 * 10^6 * 195 * 10^{-12} = 1.52\mathrm{ms} \tag{3.9}$$

and since the maximum frequency of tests is $60\,\mathrm{Hz}$

$$\tau_{Mf} = 1/60 = 16.6\mathrm{ms} \implies \tau_{Mf} = 91 \times \tau \tag{3.10}$$

Therefore, the time constant is small enough not to distort the waveform too much.

## 3.3. Test Cell

The test cell has a multilayered complex needle design. A screw mechanism with O-ring sealants is incorporated to connect the needle to the test cell to allow removal and measurement of the needle tip without draining the liquid.

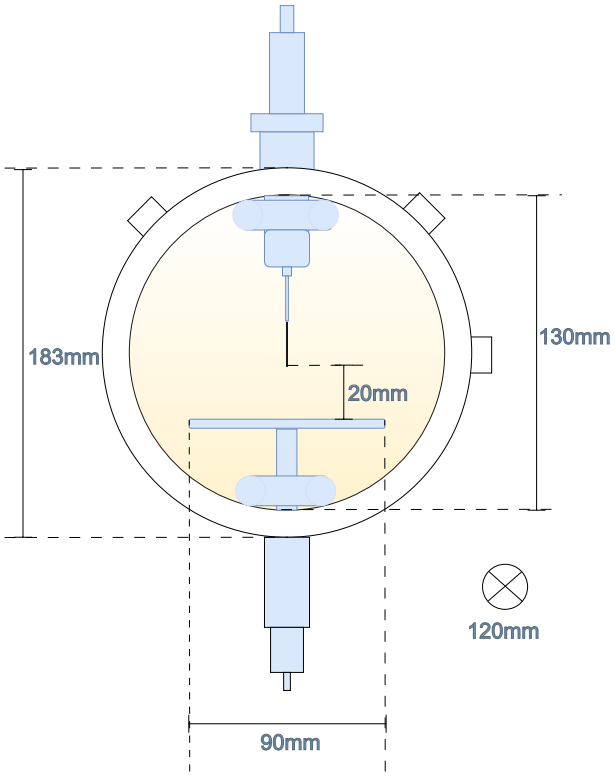


**Figure 3.9:** The test cell (test sample) [69]

The test cell comprises a cylindrical casing made of PTFE (polytetrafluoroethylene), which securely houses two glass walls on opposing sides. These glass walls are sealed together using O-rings and

serve to enclose the test cell. It has been shown in Figure 3.9. Within the casing, the plate and needle contacts are held in place. An adjustable mechanism located on the plate side regulates the gap between the two contacts.
Capable of containing approximately $800[ml]$ of liquid, the test cell features a mechanism designed to equalize internal pressure with the surrounding ambient pressure after filling. Multiple holes have been drilled into the PTFE casing to facilitate access, drainage, and filling of the test cell. These holes are sealed using caps fitted with O-rings and threads to ensure proper sealing and secure attachment.
The test cell is supported by a stand crafted from plastic.

### 3.3.1. Needle

Most metals have a boiling point which is relatively low. This can set a limit to the permissible temperature. Tungsten, however, can operate at a temperature of over $3000\,°\mathrm{C}$ [70]. Therefore, tungsten wire with a $100\,\mu\mathrm{m}$ diameter has been used for making the needle. There are multiple shielding and insulation layers added to it. It was designed and manufactured by L. Lundgaard, and G. Berg, in 2002.

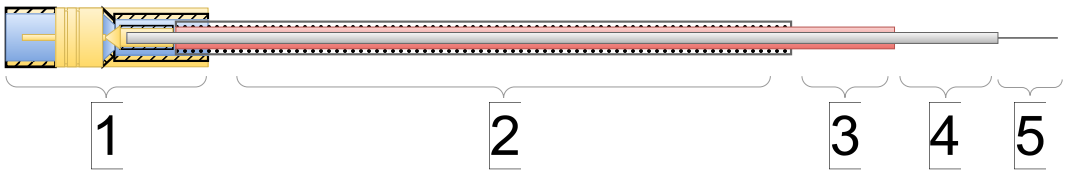


**Figure 3.10:** Configuration of the used needle (designed by L. Lundgaard, G. Berg)

According to the diagram in Figure 3.10, there is shielding for the wire against the surrounding ground, thereby minimizing noise interference.
A metal tube is holding the wire and taking the signal to the BNC connector at the end of the needle. The tip of the tungsten wire has been electrochemically etched using a $99\%$ NAOH to the desired radius. Different parts of the needle shown in the Figure 3.10 are:

1. (1) Huber Suhner 11 SMB-50-2-41/111NE
2. (2) threaded steel tube
3. (3) insulating plastic tube
4. (4) Teknolab chromatograph needle
5. (5) etched tungsten wire

Measuring the needle tip was performed using a microscope connected to a computer system. Specifically, *Carl Zeiss MicroImaging GmbH* equipment, including *AxioVision* software and an *AxioCam MRc5* camera connected to a *Discovery V12 SteREO* microscope with *100-1000x*, was employed for this purpose. the etched needle's tip can be approximated to a rotational hyperboloid at the tip, as illustrated in Figure 3.11. Given the critical significance of the tip radius in determining the electrical field, frequent measurements of the radius were conducted.

## 3.4. Conductive Current Measurement

The partial discharge causes small but rapid pulses in the current flowing through the needle, typically in the order of microamperes. These current pulses result from the presence and movement of the space charges and occur due to phenomena like avalanches or simultaneous ionization in the electric field.

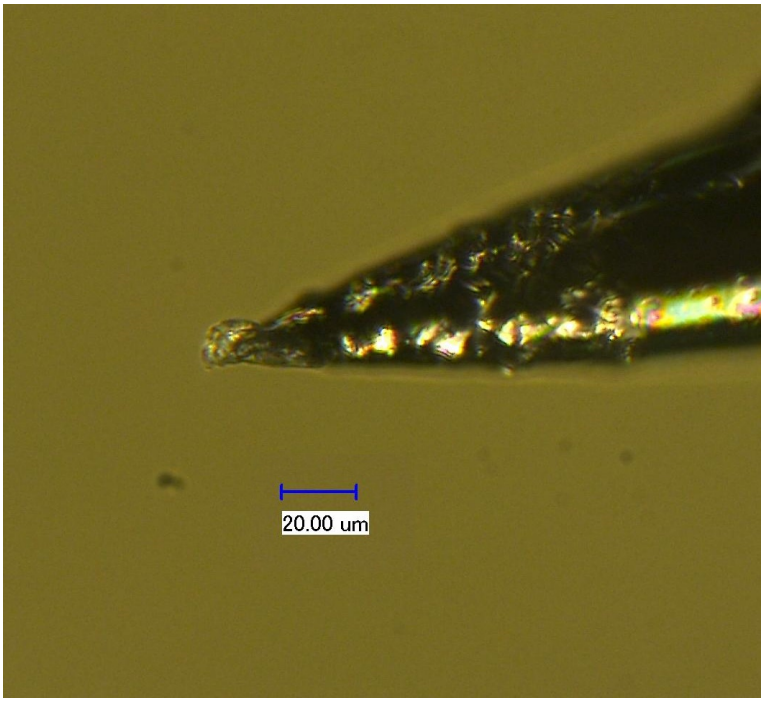


**Figure 3.11:** An example of etched needle tip under 1000 times magnification

according to the explanations in section 2.4 and explanations about the loss factor and Equation 2.12, the majority of the current flowing through the test cell is capacitive when an AC voltage is applied. There is also a limited nonlinear conductive current. This makes the test cell behave similarly to a parallel RC circuit, as demonstrated in Figure 3.12. Thus, a filtering system needs to be designed to separate out the capacitive current, ensuring that only the resistive component of the current, caused solely by space charges, is retained for accurate measurement. (see Figure 3.12 and Figure 3.20)
The current measurement is through an SR570 current preamplifier by Stanford (SR570) connected to the digitizer system. (see Figure 3.3)
This configuration enables accurate monitoring and recording of current and voltage data for analysis and assessment purposes. The preamplifier connects the needle to the ground. The voltage difference between the two ports of SR570 is negligible.

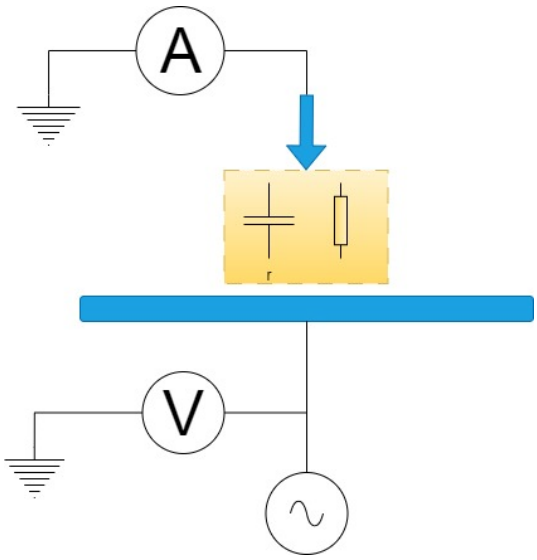


**Figure 3.12:** Equivalent circuit of the test cell

## 3.5. Optical Measurement of PDs

Previous studies show that PDs emit photons [57]. According to the theory explained in section 2.12. In order to monitor the radiant energy from the PD incidents at the needle tip, *Photomultiplier Tube*s have been used.

### 3.5.1. Photomultiplier Tube

A photomultiplier tube (PMT) is a vacuum tube that detects light. It has several applications such as scientific research, medical imaging, and industrial instrumentation. The structure and working mechanism of a photomultiplier tube are as follows: First, light (photons) enters through an incident window and strikes a photocathode (cathode), generating photoelectrons.

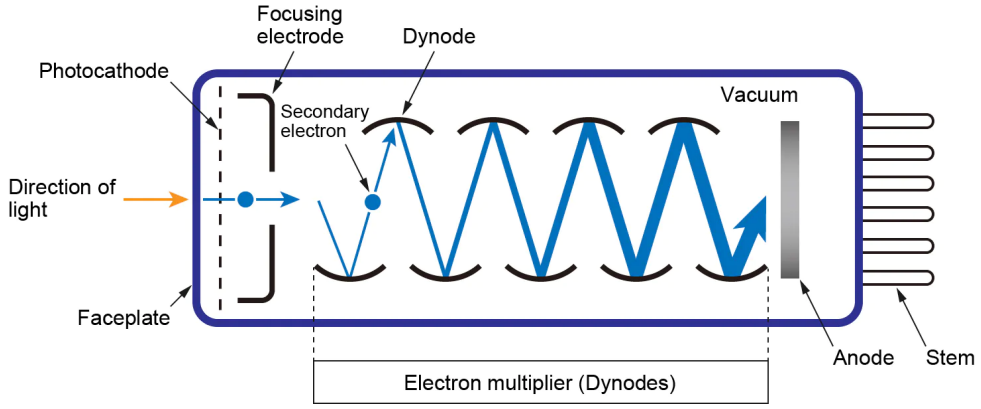


**Figure 3.13:** Photomultiplier tube structure implemented from [71]

reflected electrons are attracted by the high voltage applied to the cathode, electron multiplier (dynode) plates reflect and add to the electron flux multiple times inside the tube, and the anode is placed in the way of the last flux of electrons, which is the strongest. From the collision of the resulting electron flux to the anode plate a pulse of negative current in PMT's output. Most PMTs have 9 to 12 dynodes and amplify the photon impact by 10 to the power of 5th to 8th, depending on the applied voltage. Finally, the output is a detectable and measurable electric pulse.(Figure 3.13) A PMT is characterized by its ability to achieve an extremely high amplification rate, but this makes the output prone to *electrical noise* caused by *dark current*. Dark currents are distortions happening in PMT's answer due to unwanted photons reaching PMT from external sources or tunnelling effects that can occur in cathode or dynodes. The occurrence of dark current, whereby electrons are emitted from the photocathode due to thermal energy and subsequently strike the dynodes, results in electrical noise. Therefore, detecting the correct signal from the noise can be difficult.
There is a system designed for cooling down the contacts in PMT to minimize the electron emission due to the tunnelling effect.
Most photo multiplier tubes operate at a voltage range of $500 - 2000\mathrm{V}$. Therefore, the slightest fluctuation in the applied voltage to dynodes changes the magnifying ratio drastically. In order to accurately detect weak light, a low-noise and extremely stable voltage source is essential.
On the other hand, it poses a significant challenge. To address this issue, cooling systems are frequently employed to lower the temperature of the photocathode to sub-zero levels. This serves to reduce the likelihood of electron emission caused by thermal agitation, thereby minimizing the associated noise levels [71]. PMTs are from *Hamamatsu R943-02 EMI model* The optic PD detection system consists of two PMTs facing the test cell from the two opposite sides. Two windows of the test cell are made from tempered glass, which makes it hard to catch any ultraviolet light. However, PMTs are able to detect them. The cooling system is *Hamamatsu C4877* water-enhanced cooling system. A gain of approximately $g = 10^6$ has been set by applying $V_{DC} = 1700\mathrm{V}$ according to the gain versus voltage curve for PMTs in Figure 3.14.

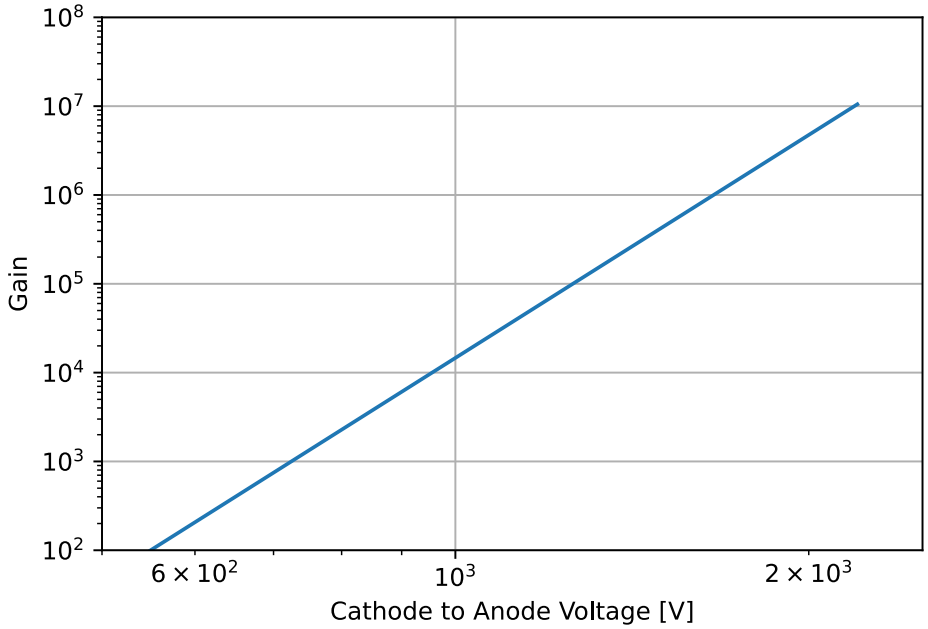


**Figure 3.14:** Gain versus voltage of PMT tube model R943-02 adopted from [72]

### 3.5.2. Coincidence Technique

There is always a level of light and thermal noise in the test. The goal of the experiment is to detect relatively small photon emissions of PDs. Therefore, the gain of the PMTs has been set around the maximum gain. The coincidence technique is an effective way to eliminate thermal and ambient light noise. Coincidence circuits have been widely used in particle detection experiments. the coincidence circuit used in this work includes two PMTs and standard coincidence instrumentation. The components of the coincidence circuit are

- Tennelec TC241 shaping amplifier
- Tennelec TC244 Shaping amplifier
- Ortec Quad 935 constant fraction discriminator
- Ortec CO4020 Quad 4-input logic unit
- Tennelec TC308 dual linear gate

Arrangements of the components have been shown in Figure 3.15. The output of PMTs is connected via a $50\Omega$ coaxial cables to amplifiers (TC241 and TC244) and then to a quad constant fraction discriminator (CFD) module. CFD is a module that sets a constant fraction timing for amplified pulses of PMTs [73].
The first channel has been checked, and the threshold has been adjusted by turning the multiturn potentiometer $T$ to $0.4\,\mathrm{V}$. After getting a reasonable signal from the output, they have been fed individually to an AND gate with *CO4020*. This gate detects the coincidence of the pulses coming from the CFDs. Since there is no internal AND gate with this device, the logic has been made with available logic gates

$$A \cap B = \overline{(\overline{A} \cup \overline{B})} \tag{3.11}$$

For a proper answer, The coarse gain of the amplifier TC241 has been set to $50\,\mathrm{a}$nd the input signal selector has been set to negative. The BLR switch is in the down position, and the signal from the unipolar output has been taken for the output. The other amplifier is TC244, and the course gain is set to $50$ The multiplier is set to unimode, and the delay of the pulse is the same as TC241.

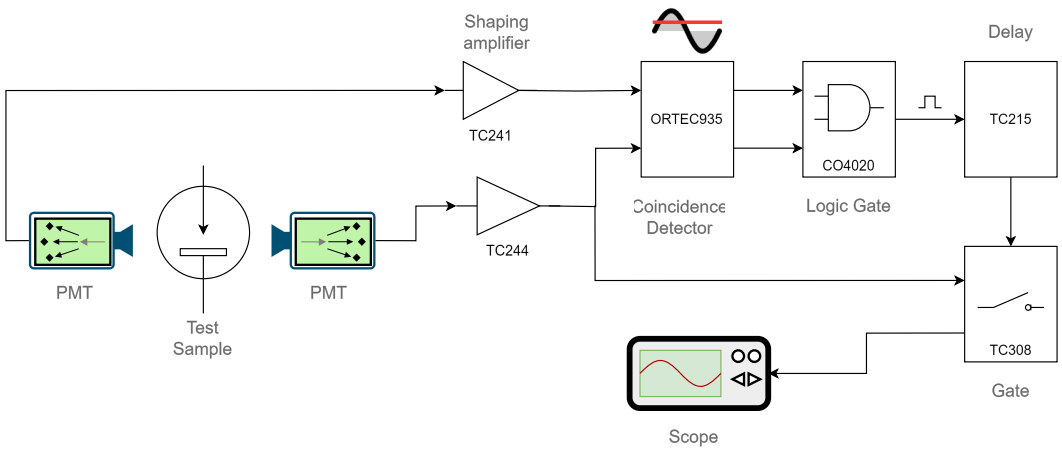


**Figure 3.15:** Arrangement of components of the coincidence circuit

The logic controller CO4020 DIP switch is critical. By choosing $L$ instead of $S$ for the last switch, longer outputs will be sent after detecting a signal. The gate has been switched by adjusting the DIP switch $G$ to the middle position. The output signal is taken from one of the $Y$ outputs on the device with a downside shape. The logic has been set to react to the increasing Edge instead of the decreasing edge of input signals to catch the moment of a new signal from CFD. After getting the output, the output pulse width is adjusted to $3\,\mu s$ by turning the $W$ potentiometer.
At this point, the coincidence circuit has been tested with a sample signal formed by the signal generator to both amplifier inputs; the output of CO4020 has been shown in yellow in Figure 3.16. The blue curve shows the input sample signal generated, and the violet and green curves show the output signals of amplifiers TC241 and TC244, which are being fed to CFD, and the yellow curve is the output logic pulse of CO4020, which is a standard NIM logic pulse.

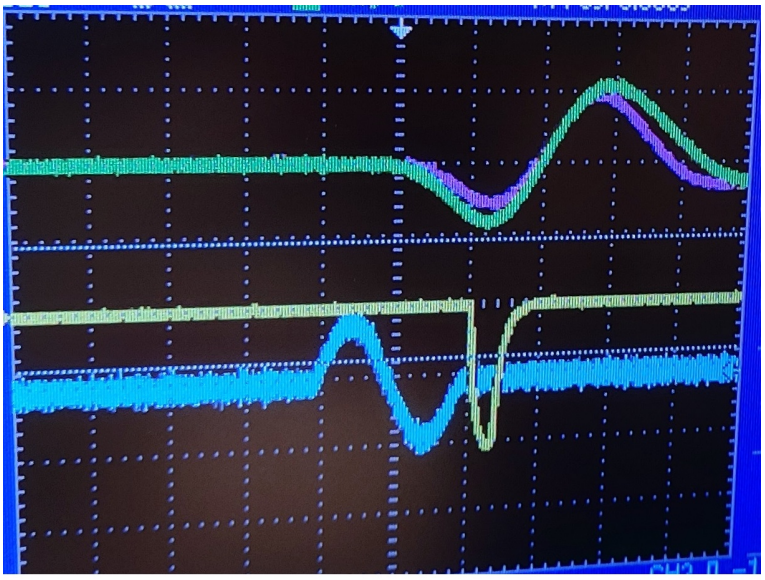

**Channel-1: Yellow, 2V , Channel-2: Blue, 10mV**
**Channel-3: Violet, 100mV , Channel-4: Green, 100mV**
**X-s/div : 500ns**

**Figure 3.16:** CO4020 output signal with amplifier output signals to a sample waveform

After testing the coincidence circuit, PMTs were connected, and the output of the CO4020 was given to the gate module TC308, and the output of one of the PMTs was given as input to the gate.

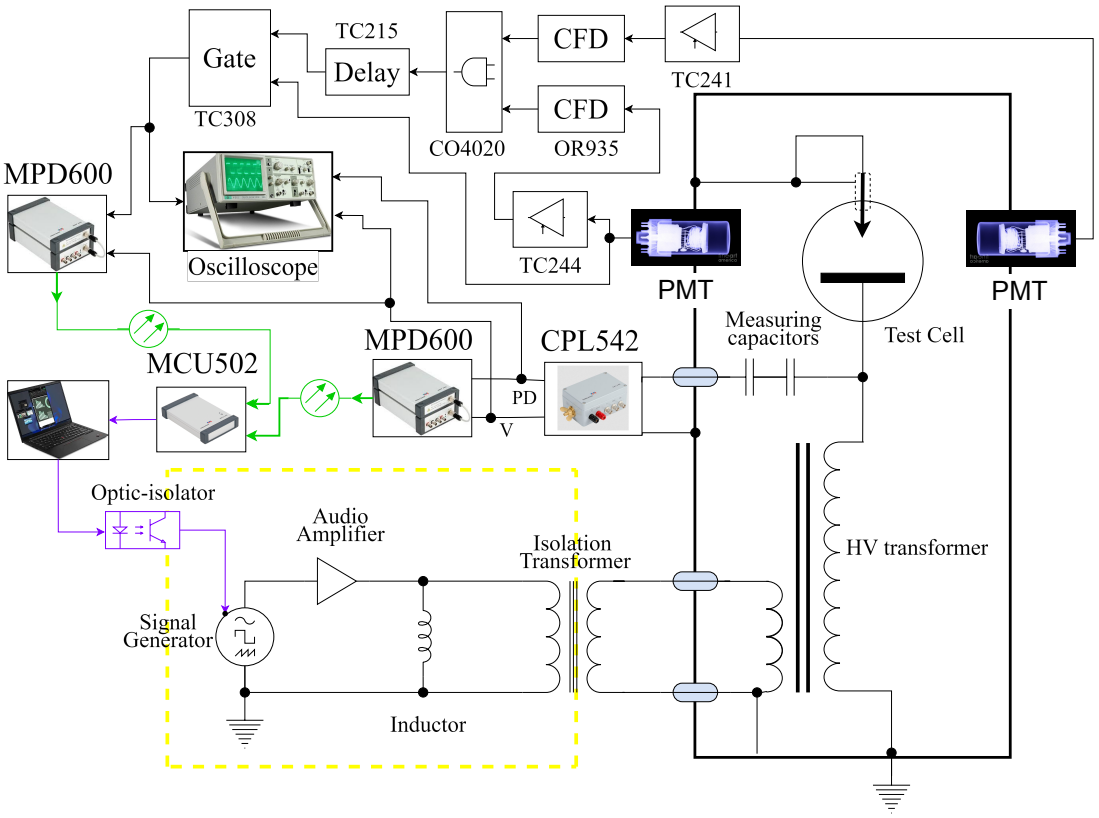


**Figure 3.17:** Diagram of the test setup for optical PD measurement

Thus, the output of the gate is the PMT signal only in small time intervals where a coincidence signal has been detected. Since it takes about $2\,\mu s$ for the whole process of coincidence circuit to detect until opening the gate, therefore a delay module TC215 with a $2\,\mu s$ delay has connected in the way of signal to output. The circuit is checked for being able to detect PDs in air from a sample wire connected to the high voltage. A diagram of the test setup has been shown in Figure 3.17.
PD in the air from a wire installed to the high voltage side has been detected electrically with omicron and optically using the described system. The output of the optical system has been shown in Figure 3.18. The yellow curve in this figure represents the voltage waveform; the violet curve shows the output of CFD of one of the PMTs, the green curve shows the output of the gate and the blue curve shows the PD output from omicron. (CPL542)
*Tektronix TDS2024C* Oscilloscope, which has been used for the experiments, is capable of triggering PD signals from omicron. based on this the capability of the optical circuit for detecting any coincidence at PD signals from Omicron has been investigated. Figure 3.19 shows the output of the gate module (green) with PD signal from omicron (Blue).
Obviously, the coincidence circuit detects the PD, which is also detected by omicron, and the signal has been used to trigger the oscilloscope. there is about $2\,\mu s$ delay from the head of the PD signal to the moment of opening of the gate, which is happening with a relatively fast impulse and then the output signal of the PMT, which has a negative polarity is visible for around $3\,\mu s$ and then the gate closes with another fast impulse.

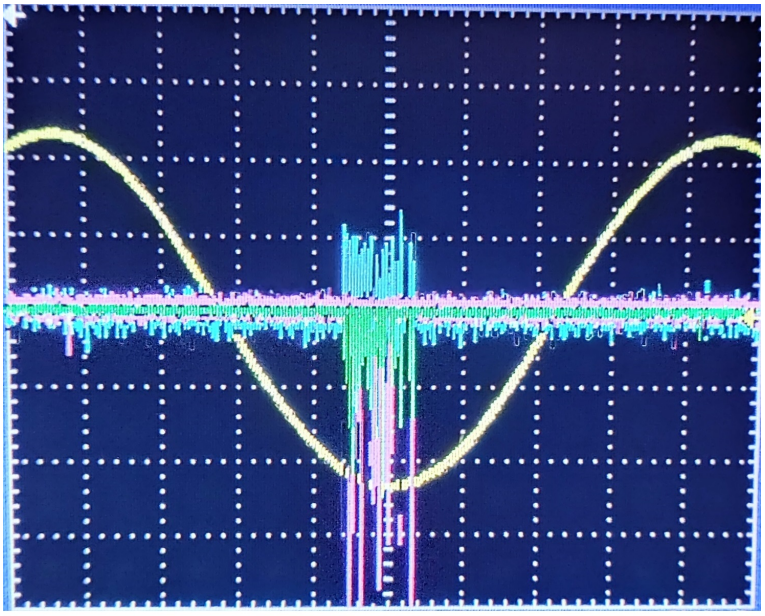


**Figure 3.18:** Coincidence circuit test results for PD in air

## 3.6. Selection of Liquids and Characteristics

Pure Cyclohexane sourced from *Uvasol* laboratory was standard for spectroscopy purposes. Prior to testing, the test sample underwent multiple washings with *Isopropanol* and was allowed sufficient time to completely vaporize under appropriate ventilation conditions. Following this preparation, the needle was sharpened to a tip radius of $1.77\,\mu\mathrm{m}$ using the specified etching process in subsection 3.3.1. Subsequently, the test sample was filled with Cyclohexane and subjected to PDIV testing according to the instructions outlined in chapter 2. Additionally, the current through the needle was measured during the experiment. characteristics of Nytro 10XN has given in product datasheet in Appendix B
MIDEL 7131 has passed through a $2\,\mu\mathrm{m}$ filter with the help of a vacuum pump, and a new set of equipment has been used to prevent impurities from entering the liquid. A special method has been used for washing the test cell, including:

1. dismantling the test cell
2. washing the parts with isopropanol
3. assembling parts
4. washing with MIDEL 7131

However, due to the high surface tension of MIDEL 7131, impurities remained inside the test cell. The test cell was inspected visually after filling up with $1.2\,\mu\mathrm{m}$ filtered MIDEL 7131, but there were impurities bigger than $1.2\,\mu\mathrm{m}$ visible within the liquid. The test cell has been relaxed for some time for the impurities to settle down away from the needle plane region inside the test cell before tests. Properties of MIDEL 7131 are in Appendix B.

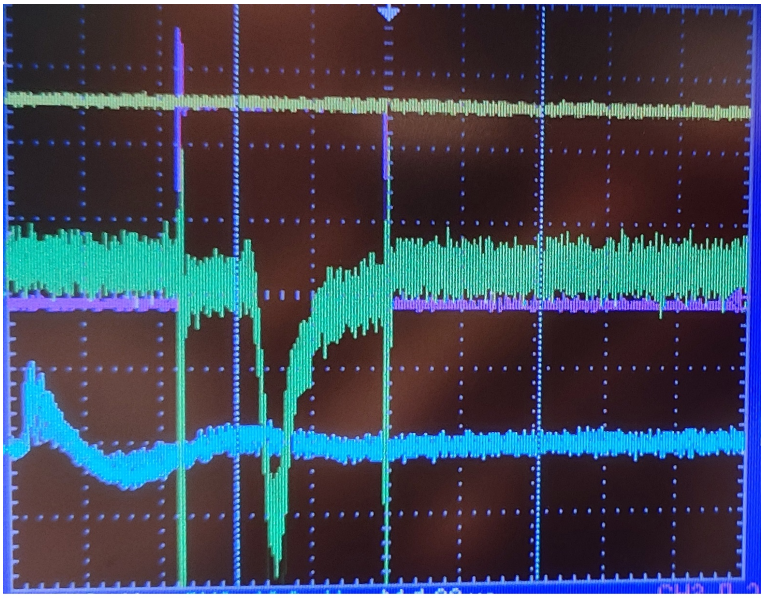


**Figure 3.19:** Coincidence circuit response to PD pulse in PD trigged scope

## 3.7. PDIV Definition

There are several definitions exist for the PDIV. It is important to know that there is not a straightforward threshold for it because it also depends on the measuring time. Definitions vary depending on whether the measurement is conducted under DC or AC voltage regimes. Experiments in [61] demonstrate that PDIV voltages differ based on the criteria used, making it challenging to establish a single meaningful threshold for assessing the quality of insulating liquids. To address this, a specific definition for PDIV testing is necessary.
However, the present IEC standards may not sufficiently reflect all the relevant functional dielectric properties of the insulating liquids [51]. After reviewing studies such as [61], a definition has been formulated for this study.
The PDIV considered in this study is obtained by increasing the voltage by $250$ volts, with each step lasting one minute. The voltage at which the first PD larger than $2\,\mathrm{pC}$ occurs during this process is considered the PDIV.

## 3.8. Data Analysis

Due to the dominance of capacitive current in the needle [23]appropriate filtering techniques are necessary to extract meaningful information from the raw data acquired by the digitizer. It should be emphasized that the measured current corresponds to the current flow from the needle to the ground, as the setup has been described in detail in subsection 3.1.1 and illustrated in Figure 3.3. the current flowing through the needle to the ground always leads to the voltage waveform. Figure 3.20 is a demonstration of an example of the raw data obtained from the digitizer.

However, obtaining more data from the current waveform without separating the capacitive current is not possible. The voltage and current waveform in practice might look sinusoidal, but they include some higher-order harmonics as well. no matter how much effort has been given to make the voltage waveform close to sinusoidal. According to

$$i_C = C\frac{dV}{dt} \tag{3.12}$$

capacitive current can be obtained by calculating the derivative of the voltage and and having the capacitance value. There are always some defects in the waveform of the voltage, which makes the derivative of the voltage a fluctuating wave. Also, considering that measured voltage is no more than a series of data points with a value in time where the gap between each two points is defined by the quality of measurement, it can not be zero. Therefore, filtering in higher-order frequencies is necessary. Understanding the significance of filtering and processing experimental data is important, particularly

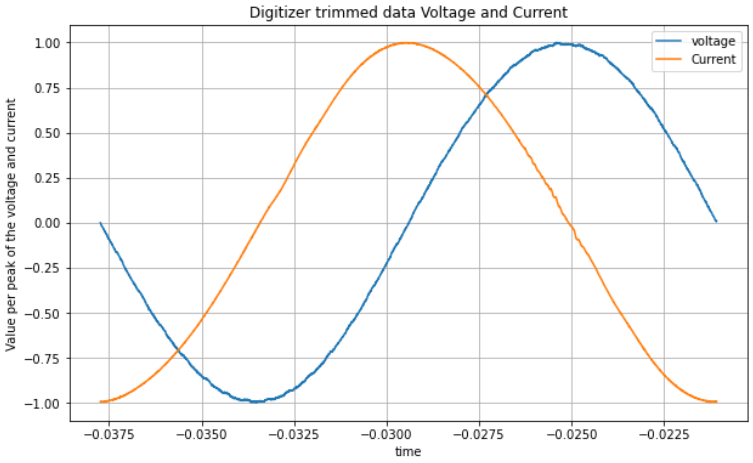


**Figure 3.20:** Measured voltage and current from Cyclohexane $60\,\mathrm{Hz}$ at $17.83\,\mathrm{kV}$ voltage peak-peak

when utilizing AC voltage above $10\mathrm{Hz}$, as in this study. In this setup, the plane is connected to the high voltage, while the omicron device measures voltage from the high voltage (plane) side (see Section subsection 3.1.1). Consequently, to accurately depict the polarity of needle potential and current, the current waveform needs to be inverted relative to the voltage waveform.

### 3.8.1. Python Script for Analysing the Data

All measured data has been saved in *".asc"* format. They have been imported into Python for multiple purposes, like visualising the saved data, filtering the voltage, calculating the $I_C$, subtracting it from the measured current to obtain conductive current, and further studying data such as finding patterns and curve fitting functions. A flowchart of the code has been shown in Figure 3.21. Different parts of the code include:

- loading data from files with a ".asc" extension in a specified folder path into a dictionary.
- plotting data from the dictionary into separate graphs and saving them.
- Extracting voltage and current data from the loaded data dictionary.
- Performing Fourier Transform on the data to analyze frequency components.
- Filtering out frequency components above a certain limit. (it has been set to $300\,\mathrm{Hz}$ for voltage before derivation)
- Calculating derivative of voltage data in the frequency domain to estimate capacitance
- Plotting voltage, capacitance, and resistive current data.
- Saving the plots and resistive current data to files.

The Python script of the code has been given in Appendix C.

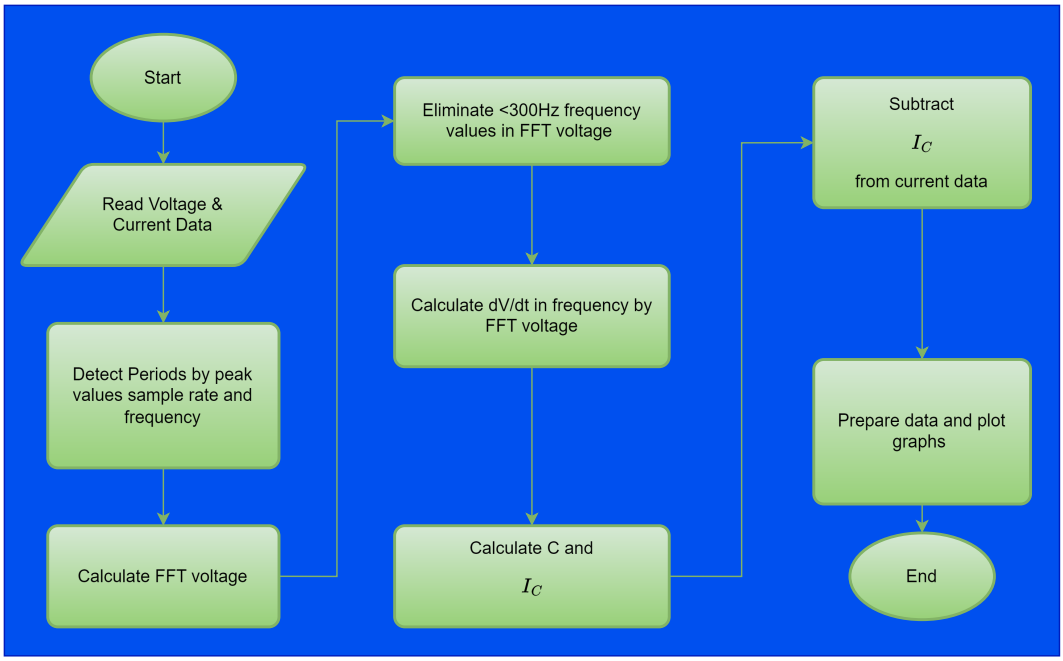


**Figure 3.21:** Flowchart of the Python script for analysing data

## 3.9. Test Procedure

The devised test procedure for investigating various liquids and discerning their distinctions is outlined below:

- Fill the test cell with a specified volume of liquid and seal the cell.
- Agitate the test cell to facilitate cleaning.
- Empty the test cell, ensuring that no remains of the ”old” liquid are in the test cell.
- Refill the test cell with the new liquid, taking care to prevent the formation of air bubbles.
- Position the test cell centrally within the test rack and align it with the optics.
- Initiate measurements using different waveforms (half-cycle or full-cycle):

  - First, conduct current measurements.

  - Second, perform PD measurements along with needle current measurements in different voltage steps.

  - third, apply a PDIV test from voltages below $2\,\mathrm{kV}$ until reaching the PDIV.
- Analyze the obtained results with the data analysing tool.

# 4

# Experimental Results

The voltage term in all parts points to the peak difference in electric potential between needle and plane contacts in the test cell. The needle is positively charged at the moment when the plane's charge is negative. The voltage has been measured by CPL542 (see section 3.1 and Figure 3.3) connected to the high voltage arm and plate. Therefore, a $180°$ phase shift has been added manually to full-cycle Histograms in order to represent the needle's voltage. Applied to all voltage measurements to show the correct polarity of the voltage on the needle.
The gap between the needle tip and the plane has been measured to be $20 \pm 0.5\mathrm{mm}$ in all tests.
Needle tip radii have been measured by using a digital microscope with $1000\,\mathrm{x}$ capability. They have been measured visually by using some measuring aids from the software of the digital microscope. The accuracy of the needle tip measurement is $\pm 0.5\mu\mathrm{m}$

## 4.1. PD Patterns in Tested Liquids

The voltage curve drawn in green in all histograms has different values; Therefore, the vertical axis for voltage amplitude has not been shown. Figure 4.1(a) shows the histogram of PD pulses in Cyclohexane at $19.81\,\mathrm{kV}$ and $30\,\mathrm{Hz}$. Figure 4.1(b) shows result for Cyclohexane at $19.35\,\mathrm{kV}$ and $45\,\mathrm{Hz}$ and PD pattern for Cyclohexane at $19.76\,\mathrm{kV}$ and $60\,\mathrm{Hz}$ has shown in Figure 4.1(c).
All PD histograms have been recorded in $1$ minute duration. The same needle has been installed for all three tests in Figure 4.1, in which the tip radius was $1.7\,\mu\mathrm{m}$ before tests and $6.03\,\mu\mathrm{m}$ after tests. It should be noted that each dot on the histogram shows the charge magnitude of the PD pulse on the vertical axis, and the phase angle is shown on the horizontal axis in time sequences.
The colour spectrum at the right side of each result shows the intensity of pulses per second. Red colour means more intense, and blue colour means less intense.
All PD histograms have been filtered for Pulses smaller than $1\,\mathrm{pC}$ because of the noise.
An intense accumulation of PD pulses between $2\,\mathrm{pC}$ to $11\,\mathrm{pC}$ in the negative peak of the voltage has been observed in Figure 4.1. There is also a symmetric concentration for the incidents happening at a negative peak. There are some rare incidents happening at the positive peak, but they have a relatively large magnitude. from $40\,\mathrm{pC}$ to $70\,\mathrm{pC}$, and evidence suggests that larger PD incidents in magnitude are more effective regarding needle erosion. (see section 4.4)

PD histogram results for Nytro 10XN tests have been presented in Figure 4.2. In Figure 4.2, (a) shows the result of test under $22.89\,\mathrm{kV}$ tension and with $30\,\mathrm{Hz}$ frequency while (b) and (c) are showing results under $23.91\,\mathrm{kV}$ and $23.26\,\mathrm{kV}$ with frequencies of $45\,\mathrm{Hz}$ and $60\,\mathrm{Hz}$, relatively. In contrast with Cyclohexane, the PD incidents at the negative peak are more concentrated towards the lower edge and peak voltage line. At the positive peak, there are a few incidents happening above $100\,\mathrm{pC}$ magnitude. This is different in PD patterns of Nytro 10XN than in other liquids. The tip radius was $5.24\,\mu\mathrm{m}$ before tests and $11.6\,\mu\mathrm{m}$ after tests. It has been believed that this pattern may have some parts below $1\,\mathrm{pC}$, but PD pulses under this magnitude have not been considered due to noise.

Figure 4.3 shows the PD histogram of MIDEL 7131 tests under $20.86\,\mathrm{kV}$ with $30\,\mathrm{Hz}$, $22.41\,\mathrm{kV}$ with $45\,\mathrm{Hz}$ and $22.75\,\mathrm{kV}$ with $60\,\mathrm{Hz}$. These patterns show less number of incidents in the same amount of time because the electrical field of these tests was closer to PDIV. Since they were tested by a needle with the tip round of $5.26\,\mu\mathrm{m}$ and after tests tip radius was $10.40\,\mu\mathrm{m}$. But the pattern for PD pulses in the MIDEL 7131 around the negative peak of the voltage is concentrated from $1\,\mathrm{pC}$ to $30\,\mathrm{pC}$ but the pattern around the positive peak includes two parts, some rare but large incidents happened from $100\,\mathrm{pC}$ to $1\,\mathrm{nc}$ and another part from$1\,\mathrm{pC}$ to $2\,\mathrm{pC}$ but more incidents in number in the test time duration.

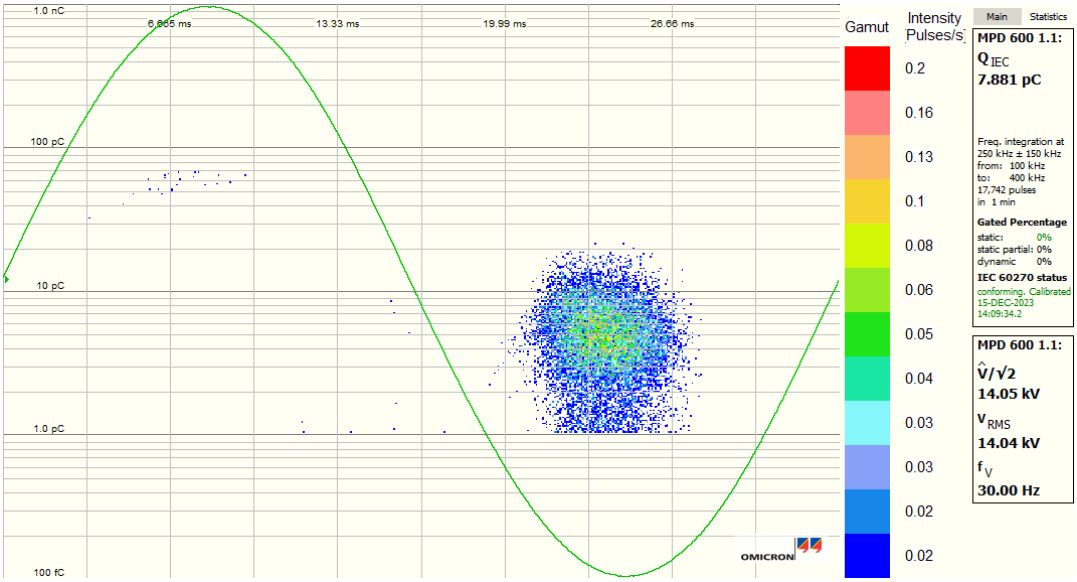


**(a)** $f = 30\text{Hz}$, $V_{peak} = 19.81\text{kV}$ with $r_0 = 1.7\mu\text{m}$

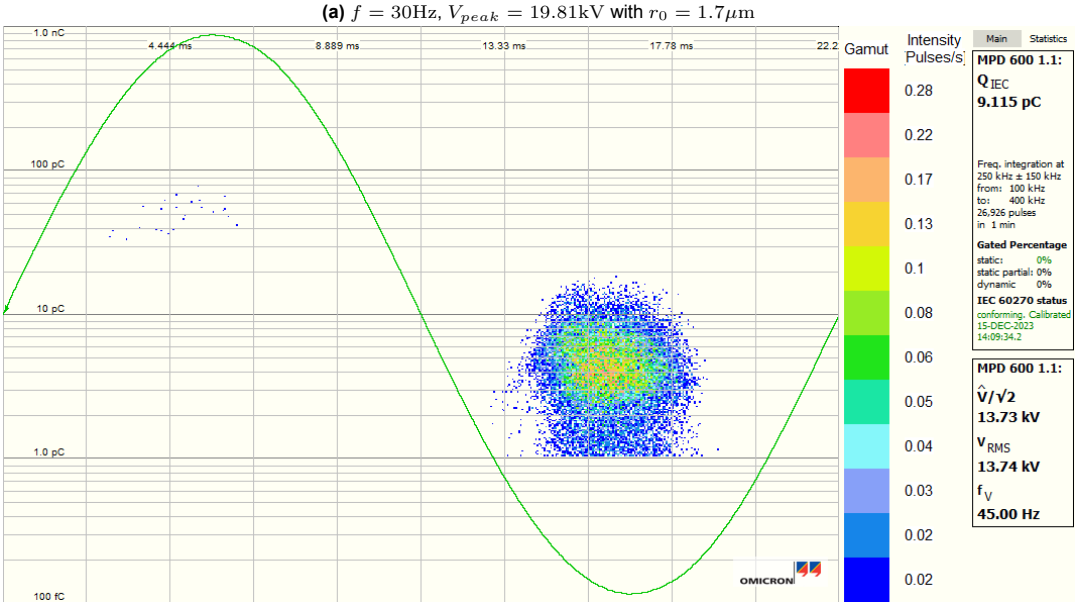


**(b)** $f = 45\text{Hz}$, $V_{peak} = 19.35\text{kV}$ with $r_0 = 1.7\mu\text{m}$

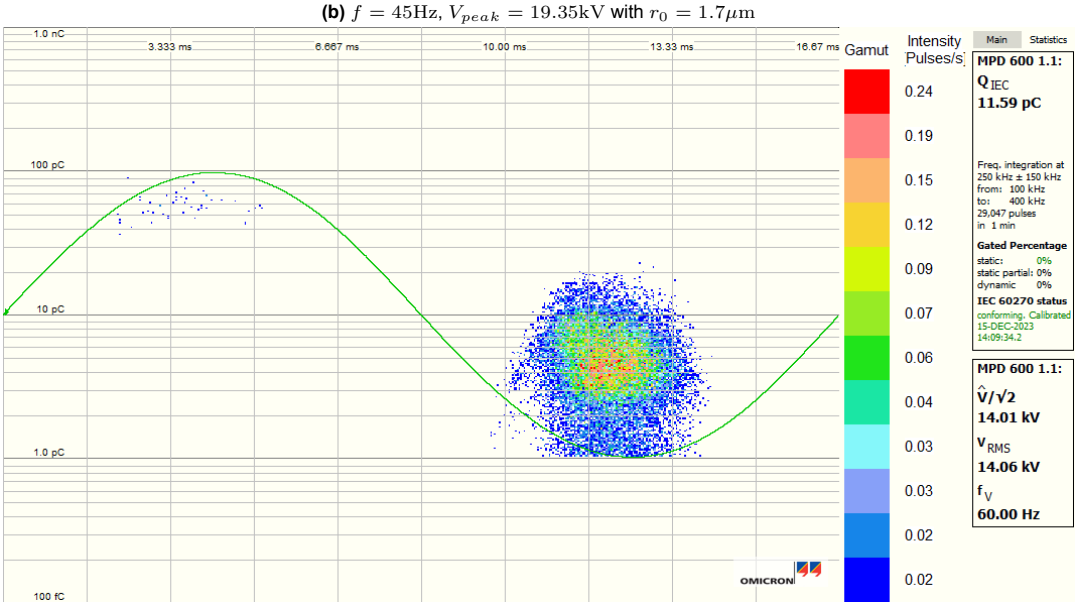


**(c)** $f = 60\text{Hz}$, $V_{peak} = 19.76\text{kV}$ with $r_0 = 1.7\mu\text{m}$

**Figure 4.1:** Histogram of the PD pulses larger than $1\,\text{pC}$ of the tests with Cyclohexane

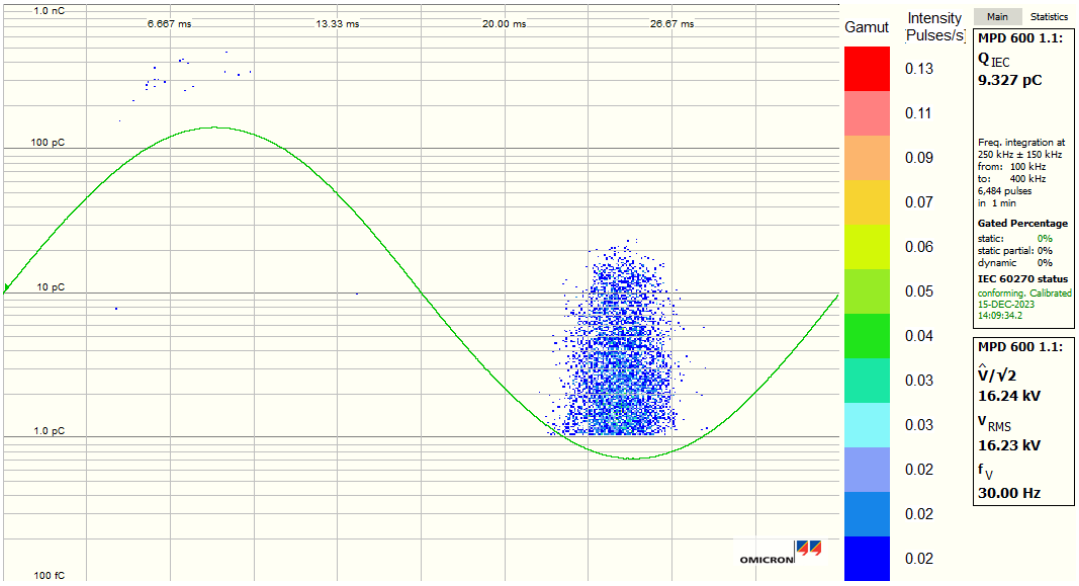


**(a)** $f = 30\text{Hz}$, $V_{peak} = 22.89\text{kV}$ with $r_0 = 5.3\mu\text{m}$

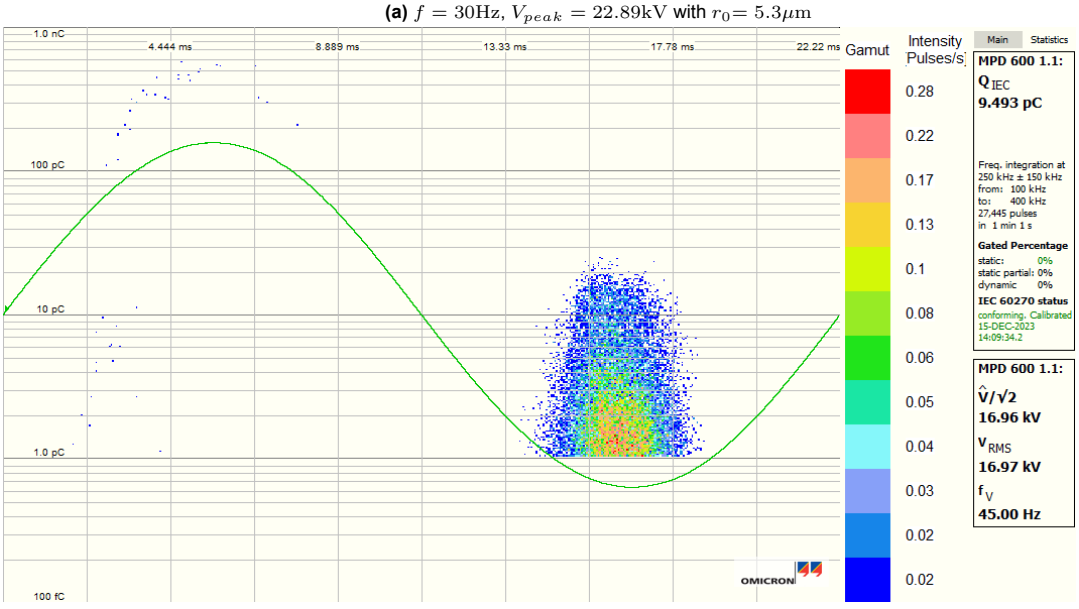


**(b)** $f = 45\text{Hz}$, $V_{peak} = 23.91\text{kV}$ with $r_0 = 5.3\mu\text{m}$

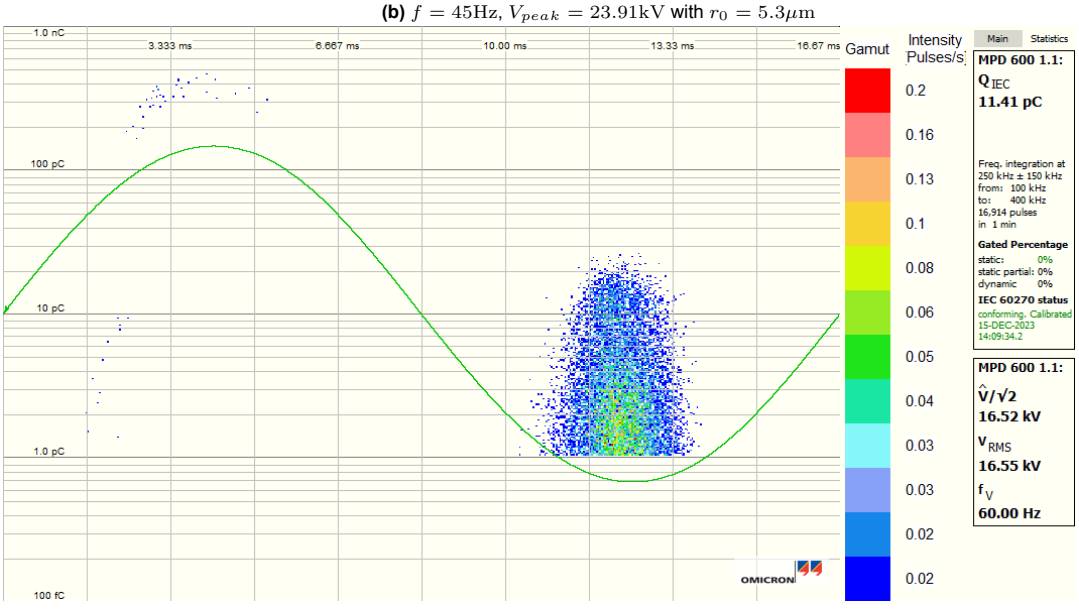


**(c)** $f = 60\text{Hz}$, $V_{peak} = 23.26\text{kV}$ with $r_0 = 5.3\mu m$

**Figure 4.2:** Histogram of the PD pulses larger than $1\,\text{pC}$ of the tests with Nytro 10XN

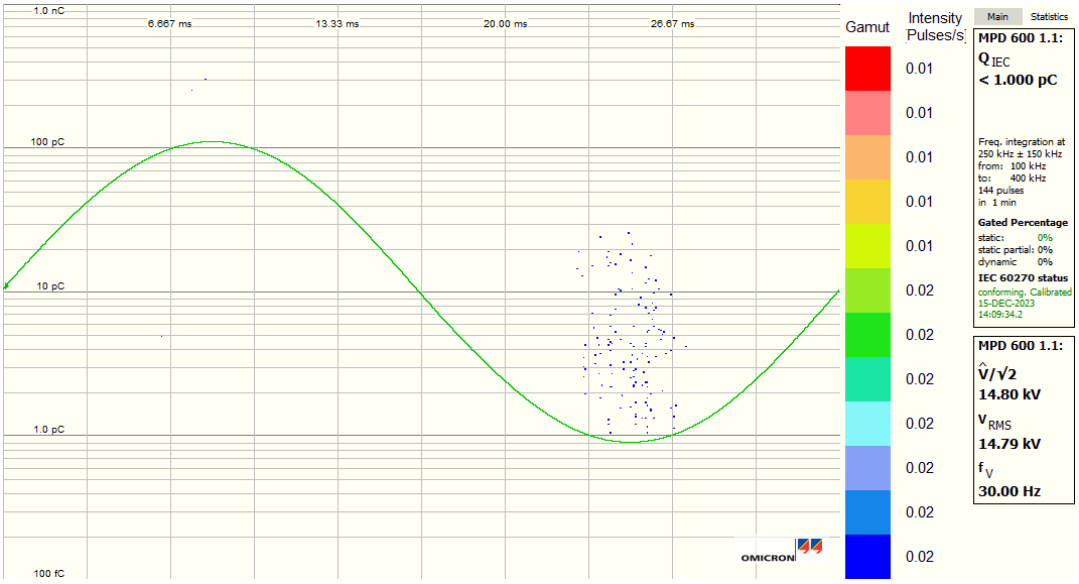


**(a)** $f = 30\text{Hz}$, $V_{peak} = 20.86\text{kV}$ with $r_0 = 5.26\mu\text{m}$

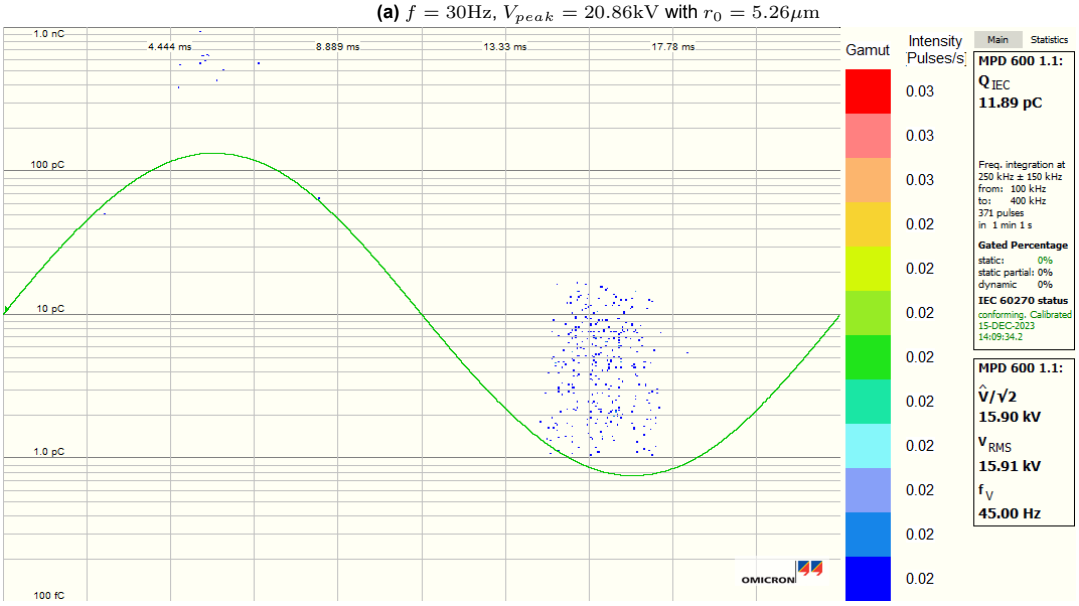


**(b)** $f = 45\text{Hz}$, $V_{peak} = 22.41\text{kV}$ with $r_0 = 5.26\mu\text{m}$

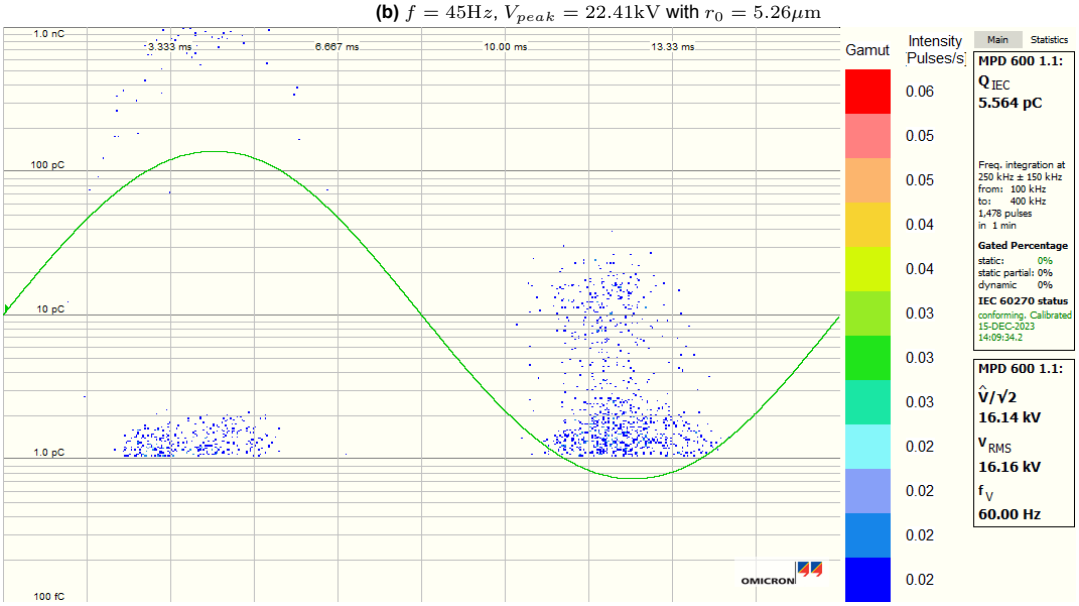


**(c)** $f = 60\text{Hz}$, $V_{peak} = 22.75\text{kV}$ with $r_0 = 5.26\mu\text{m}$

**Figure 4.3:** Histogram of the PD pulses larger than $1\,\text{pC}$ of the tests with MIDEL 7131

## 4.2. Conductive Current Measurements

Figure 4.4 shows a group of graphs of the conductive current waveforms in time for each test for Cyclohexane in four voltage levels and in three frequencies.
Applied voltage waveform in these tests has been shown in these results with blue colour. The peak value of the applied voltage has also been shown on each graph.
The vertical axis of each graph consists of two axises the left is related to the conductive current in $\mathrm{nA}$, and the vertical axis at the right of each graph is related to voltage in $\mathrm{kV}$ Difference in horizontal axis values is due to data recording time and also due to the selection of the cycle in the whole data range. voltage waveform has been recorded from the output of the CPL542 in the upper omicron device.

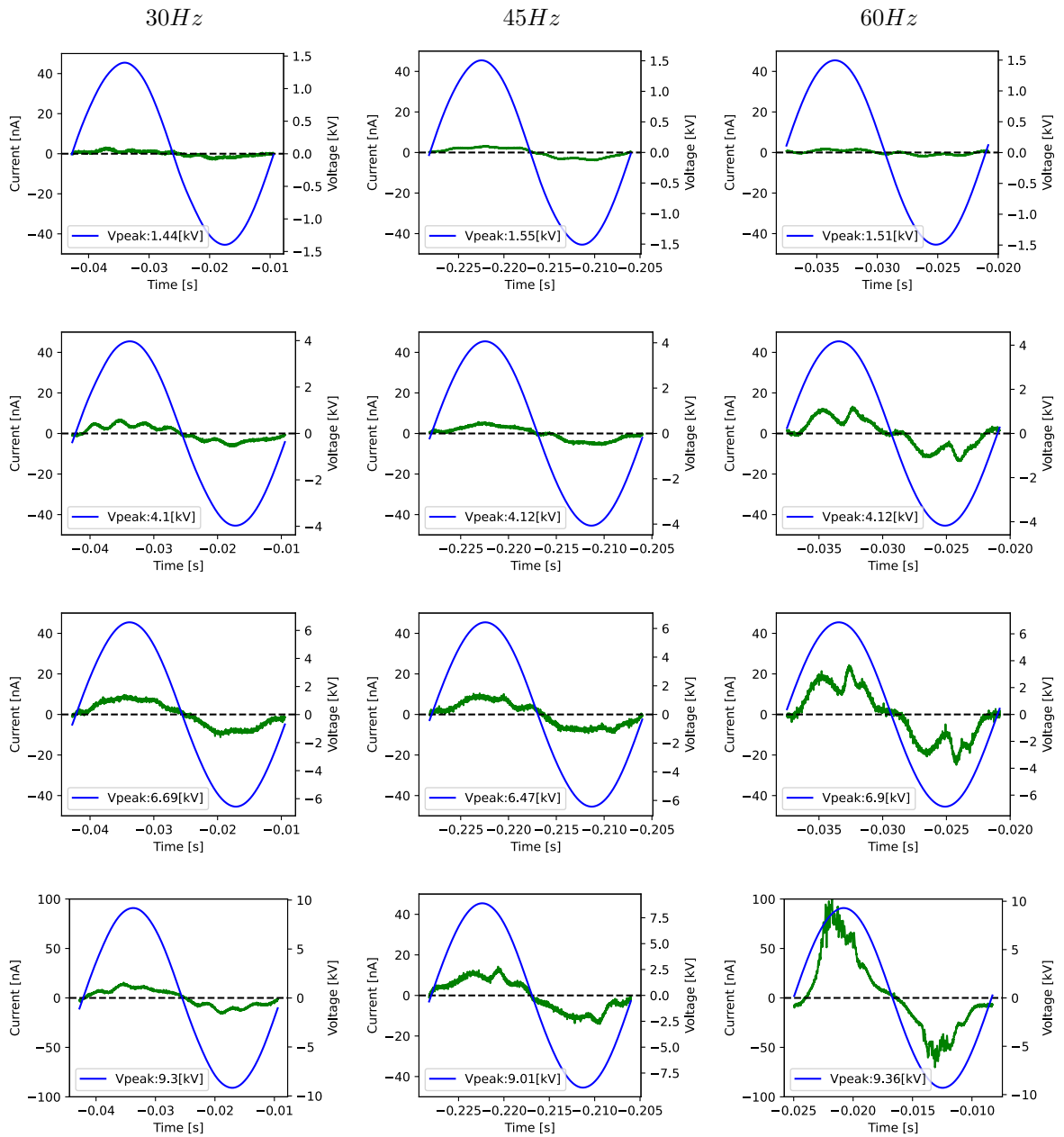


**Figure 4.4:** Conductive current and voltage versus time in different voltage steps and frequencies for Cyclohexane

Therefore, the data is related to the plane voltage. Voltage data has been inverted to show the voltage on the needle.
It is obvious that the amplitude of the conducting current increases with the increase of the voltage. It has a linear behaviour under PDIV voltage, which is visible in all graphs. As it is evident from the Figure 4.4.
The same needle has been used for each liquid's test group. It should not be neglected that needle erosion happened during the tests, which has been discussed in section 4.4.
The conductive current of Nytro 10XN and MIDEL 7131 has been tested with the same test procedure. The test cell has been dismantled and washed properly according to the explanation in chapter 3 with Isopropanol after emptying Nytro 10XN.

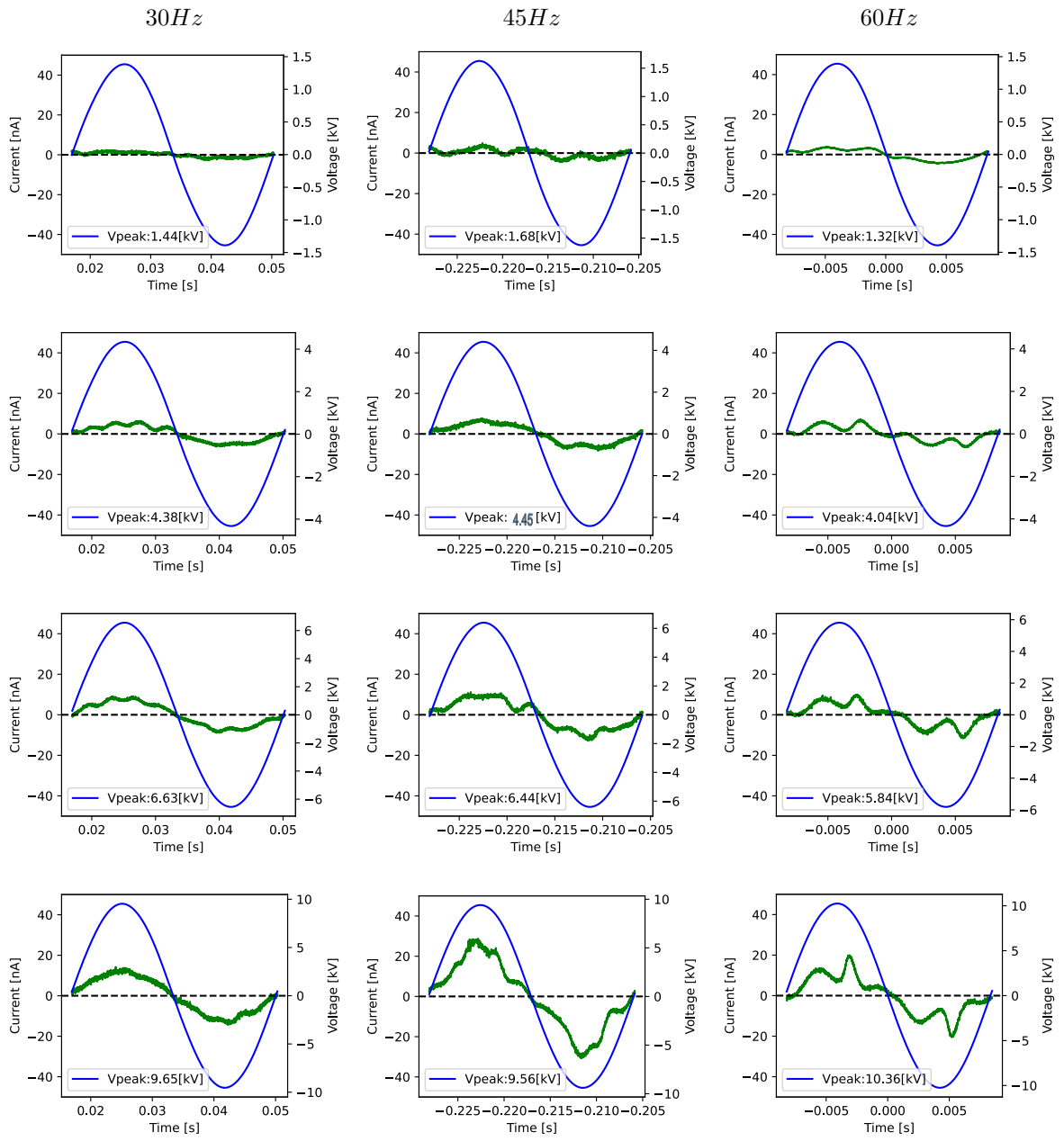


**Figure 4.5:** Conductive current and voltage versus time in different voltage steps and frequencies for Nytro 10XN

It has been washed again with MIDEL 7131 a couple of times, and the used MIDEL 7131 has been thrown out to make sure that it has the minimum effect on the purity of the liquid in the next test.
It is notable that the Nytro 10XN underwent a filtration process utilizing a $1.2\,\mu m$ filter in conjunction with a vacuum pump for purification.
There is a visible asymmetry between two sides in each half-cycle in the higher frequency ($60\,Hz$). They can be least possibly due to harmonics in the measured current or voltage and more likely due to explanations in chapter 6.
The same filtering settings have been used for all tests, even for the lower frequencies at high voltage levels, but they do not show asymmetry in the current waveform. Another reason this asymmetry is related to the movement of space charges is the same shape between tests with different frequencies.
In Figure 4.4, comparing graphs for Cyclohexane at $9.01\,kV$ with $45\,Hz$ with Cyclohexane at $6.9\,kV$ with

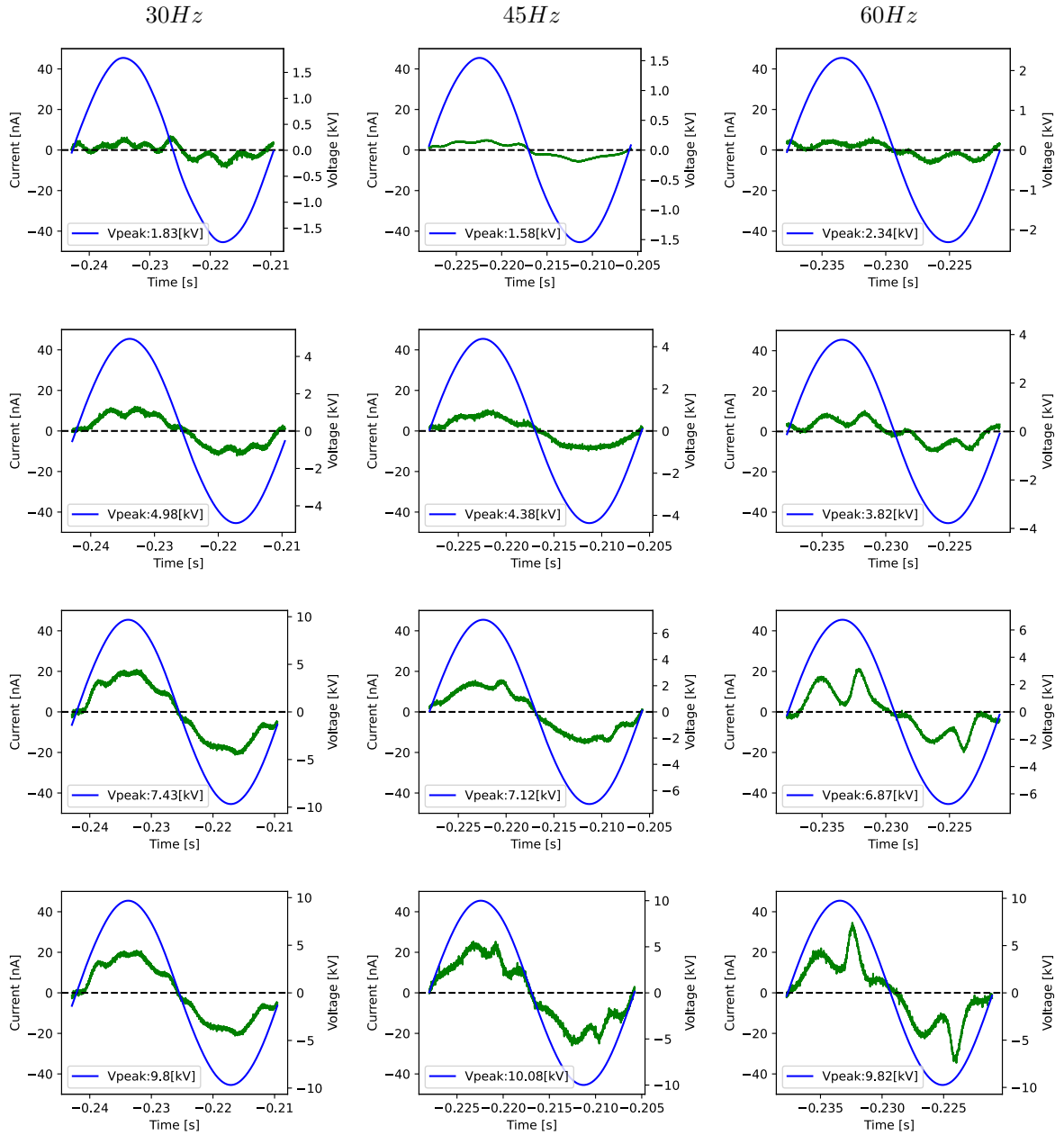


**Figure 4.6:** Conductive current and voltage versus time in different voltage steps and frequencies for MIDEL 7131

$60\,\mathrm{Hz}$, The same trend happens in different frequencies in the second quarter of the cycle. In addition to that, this trend is not related to the molecule since the same asymmetry is detectable in Nytro 10XN and MIDEL 7131. In Figure 4.5 Nytro 10XN at $6.44\,\mathrm{kV}$ with $45\,\mathrm{Hz}$ and at $5.84\,\mathrm{kV}$ with $60\,\mathrm{Hz}$ shows the same trend. MIDEL 7131 test results in Figure 4.6 at $7.12\,\mathrm{kV}$ with $45\,\mathrm{Hz}$ and at $6.87\,\mathrm{kV}$ with $60\,\mathrm{Hz}$ also showing the same trend. In Figure 4.4 in the graph for $V_{peak} = 9.36\mathrm{kV}$ and $60\,\mathrm{Hz}$ the waveform shape has been changed because of PD incidents happening at the voltage peak at both positive and negative peaks of the voltage.
It is notable that PD pulses are happening in positive and negative half-cycles at the same time. This is in accordance with the results from the optical PD measurement which is explained later in section 4.6. The FFT components for frequencies lower than $300\,\mathrm{Hz}$ have been used for calculating and resembling the voltage derivative and, consequently, the capacitive current. This frequency has been chosen after many tests because it gives accurate results with lower fluctuations.

### 4.2.1. Peak Values of the Conductive Current

The peak current graphs for each liquid have been shown in Figure 4.7 for testing Cyclohexane, Figure 4.8 for testing Nytro 10XN and Figure 4.9 for testing MIDEL 7131.
The highest value of the current passing through liquid between needle and plane has been considered in the whole recorded span of each data.
The radius of the needle tip is mentioned for each test; however, it changed during the tests due to needle erosion. It had a considerable influence on the electric field strength. The relativity between conductive current and the field strength is according to

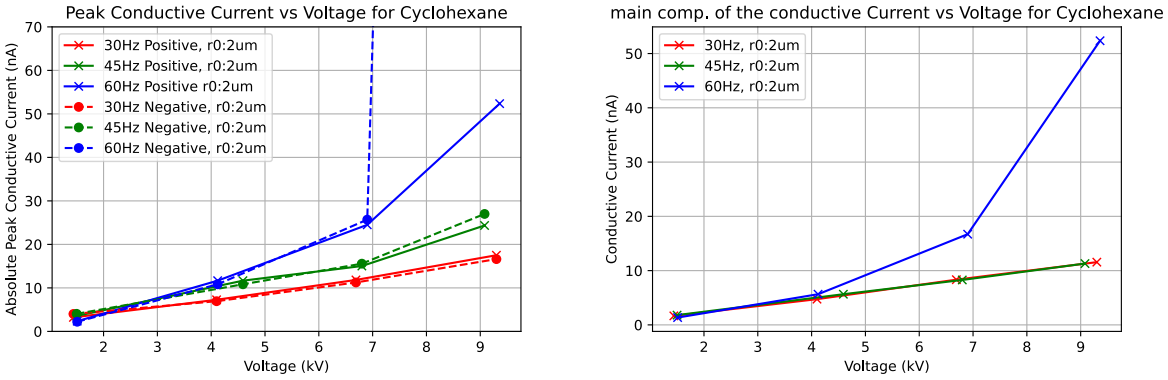


**(a)** Peak current versus voltage

**(b)** Main component peak versus voltage

**Figure 4.7:** Conductive Current peak versus voltage for Cyclohexane

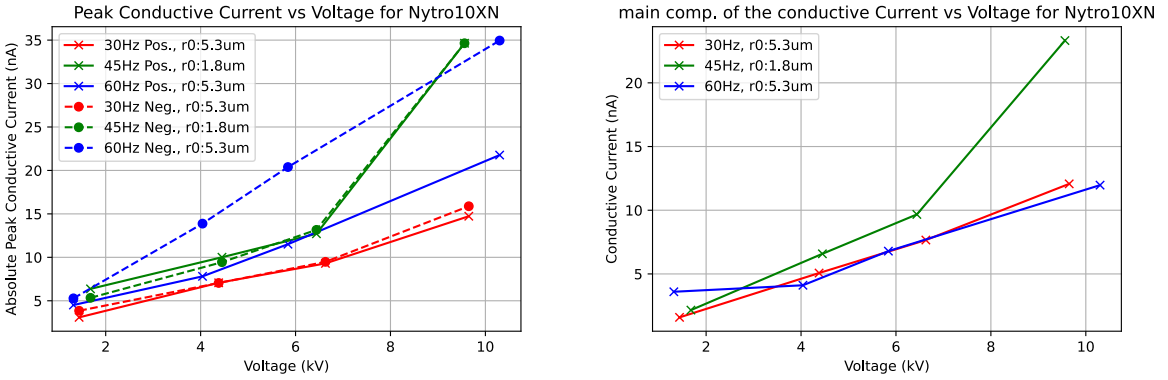


**(a)** Peak current versus voltage for Nytro 10XN

**(b)** Main component peak versus voltage for Nytro 10XN

**Figure 4.8:** Conductive Current peak versus voltage for Nytro 10XN

Figure 2.9. Figure 4.7(a) shows the positive and negative peaks of the conductive current for Cyclohexane tests. This graph shows a direct relation between the frequency and conductive current peak. Figure 4.8 shows the peak current and peak of the main component of the conductive current in Nytro 10XN. These graphs show a slope change at a transitioning point from nonlinear to exponential regions. The same trend has also been observed for MIDEL 7131 at the lower electric field at Figure 4.9. At higher voltages, the peak current values indicate several pulsed peaks resulting from PD incidents, which affect the maximum value.
The maximum value of the data sets with PD incidents usually indicates the maximum range of the preamplifier, which doesn't give any insight into the phenomena.
Therefore, the peak value of the main frequency of the conductive current has been obtained.

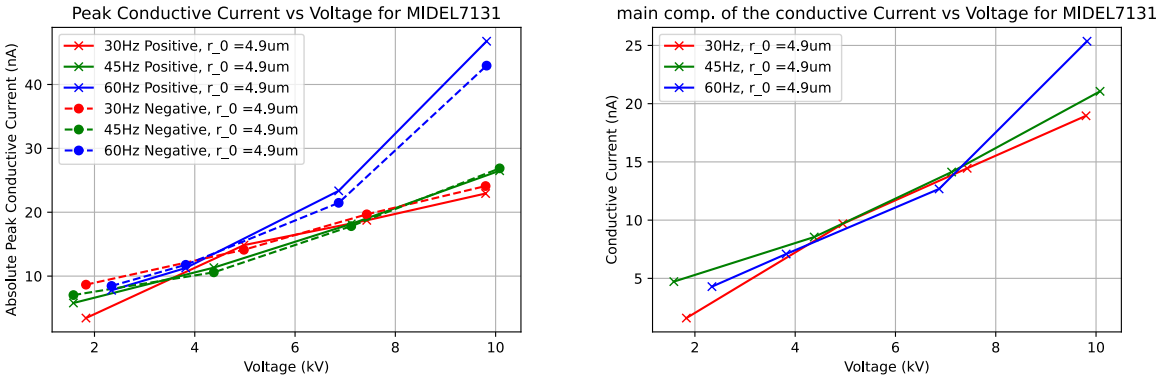


**(a)** conductive current peak

**(b)** Main component peak

**Figure 4.9:** Conductive Current peak versus voltage for MIDEL 7131

Consequently, with the change of the needle tip radius due to erosion, the conductive current also changes. This change is relatively linear in Region 1, but it is nonlinear in Region 2 and close to exponential in Region 3.
Another test has been prepared to measure the conductive current of different needle tip radii on Nytro 10XN in different voltages. Figure 4.10 shows results of Nytro 10XN tested with $45\,\mathrm{Hz}$ and two different needles tip radii of $1.8\,\mu\mathrm{m}$ and $2.3\,\mu\mathrm{m}$ which clearly shows the difference in conductive current in the same voltages due to different field strength and active region volume of the needle tip.

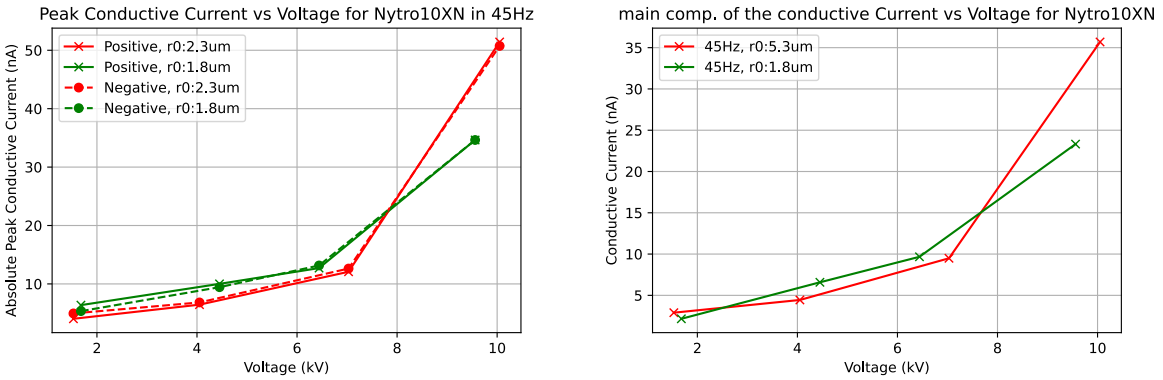


**(a)** Peak current vs. voltage for Nytro 10XN with different tip radius

**(b)** Main frequency vs. voltage for Nytro 10XN with different tip radius

**Figure 4.10:** Conductive Current peak versus voltage with different needle tip radii for Nytro 10XN

### 4.2.2. Influence of Remaining Space Charges in the Region After a PD Incident

The influence of space charges on the conductive current is detectable in the periods following a large PD incident in all three liquids. Investigating this phenomenon requires a special situation where a

couple of periods without PDs would follow a large PD incident. Therefore all the tests have been taken at a voltage around PDIV level. Figure 4.11 shows the conductive current (resistive current) in 7 cycles after a PD incident in Cyclohexane under $16.03\,\mathrm{kV}$ peak voltage and $30\,\mathrm{Hz}$ voltage and frequency. The exponential fit is a function fitted to the negative peaks of the conductive current from the first peak to a few later peaks. The same procedure has been used for Nytro 10XN under $19.3\,\mathrm{kV}$ and $30\,\mathrm{Hz}$, which has been shown in Figure 4.12.

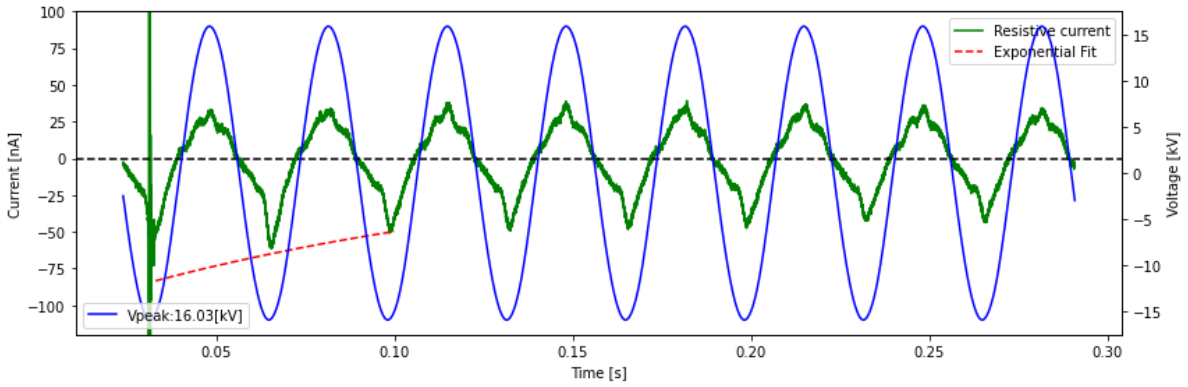


**Figure 4.11:** Conductive current and voltage waveforms after a large PD incident in Cyclohexane at 30Hz

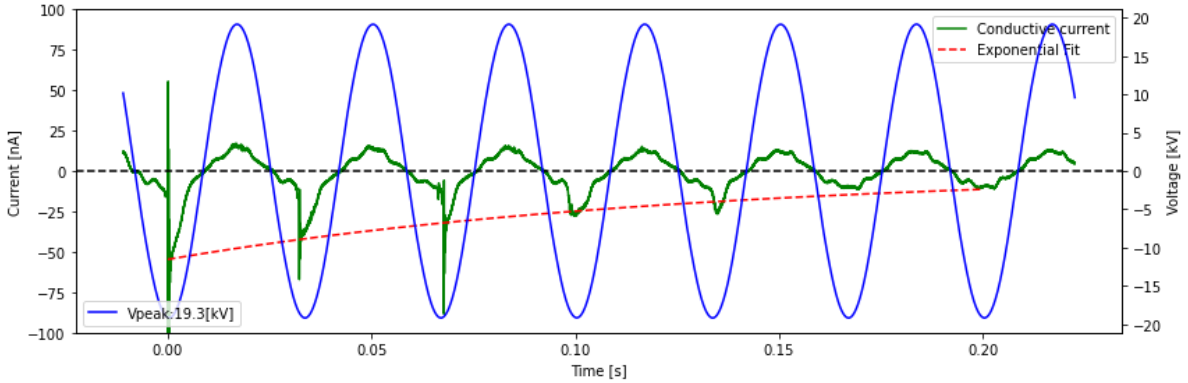


**Figure 4.12:** Conductive current and voltage waveforms after a large PD incident in Nytro 10XN at 30Hz

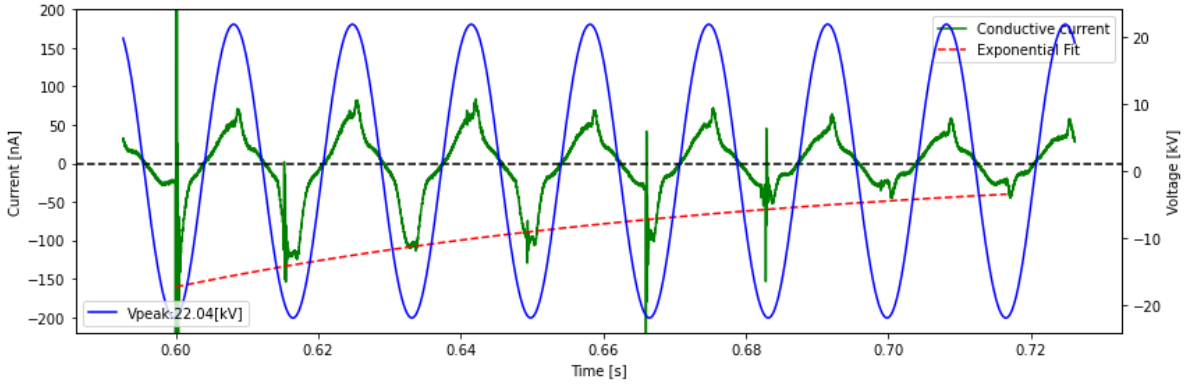


**Figure 4.13:** Conductive current and voltage waveforms after a PD incident in Nytro 10XN at 60Hz

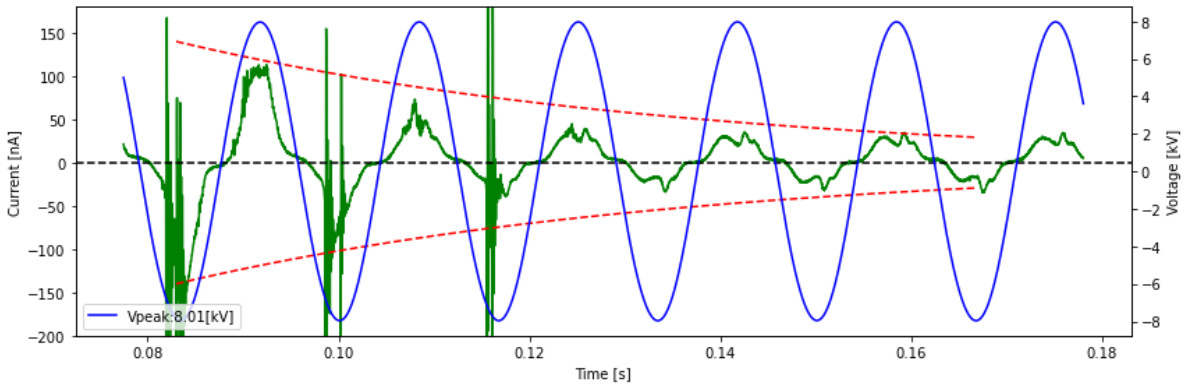


**Figure 4.14:** Conductive current and voltage wave forms after a PD incident in Cyclohexane at 60Hz

In Figure 4.13, 7 cycles of the conductive current have been shown in Nytro 10XN under $22.04\,\mathrm{kV}$ peak voltage and $60\,\mathrm{Hz}$ frequency and the Figure 4.15 shows the same trend in results for MIDEL under $19.8\,\mathrm{kV}$. The memory effect for the conductivity current of the liquids after a large PD incident is because of the space charges present in the region for a short time. It later decreases with the same trend in all the tests. Finding an exponential decrease in the conductive current peaks is tricky in higher frequency since, in most parts of the results, it was not possible to find the proper situation where a couple of cycles would follow a large PD incident.

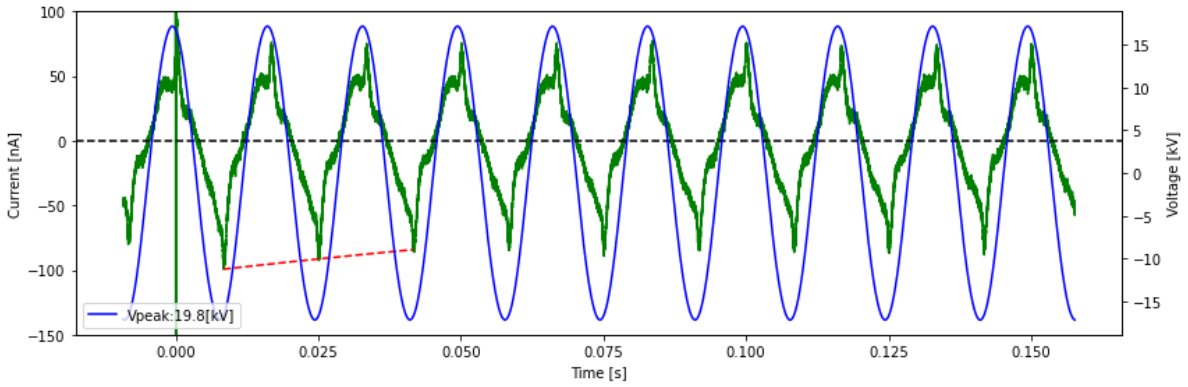


**Figure 4.15:** Conductive current and voltage waveforms after a PD incident in MIDEL 7131 at 60Hz

## 4.3. Effect of the Half-cycle Voltage on the Conductive Current

The test setup has been modified to be able to generate half-cycle voltages according to subsection 3.2.2. The modified test setup has two omicron measurement devices to measure the HV circuit from two points. (Omicron 1&2) The equivalent circuit of the test setup has been shown in Figure 3.7. The measured and filtered waveform of the voltage has been shown in Figure 4.16. It is obvious that the first quarter of the voltage waveform is sinusoidal. The second and third quarters decrease with the time constant of the load side in the half-cycle setup. It has been calculated in subsection 3.2.2. The half-cycle test is performed on Nytro 10XN at $45\mathrm{Hz}$. the peak voltage at the positive and negative half-cycle voltages are $\pm 19.5\mathrm{kV}$. It is obvious that despite the filtered voltage which follows the measured voltage well, there are some differences at the discontinuity points. Figure 4.17 shows the measured voltage and current waveforms; voltage data has been divided by $50$ to fit in the graph range, and current data in this graph has been recorded in volts since the output ratio of the preamplifier is $1\,\mathrm{V}$ per $\mu\mathrm{A}$ of current. (see Figure 3.3)

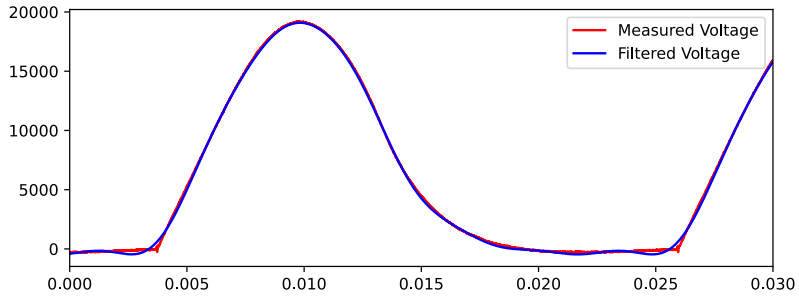


**Figure 4.16:** Measured and filtered voltage waveforms in positive half-cycle test $V_{peak} = 19.5\text{kV}$

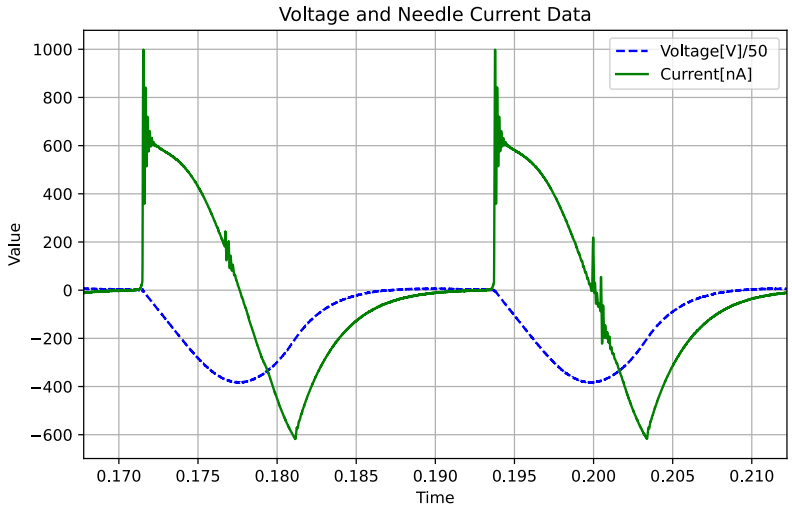


**Figure 4.17:** Voltage and Current Data of negative half-cycle test together

After adding the rectifier part to the test setup as the configuration in subsection 3.2.2, flipping the diode $D1$ in Figure 3.7 changes the polarity of the voltage, and only the negative half-cycle of the voltage will be applied to the test cell.
In Figure 4.18, the blue curve shows the applied voltage of the needle, the red curve shows the capacitive current calculated with FFT filter for eliminating over $300Hz$ components, the orange curve showing the measured current of the needle and the green curve shows the conductive current waveform resulted from subtracting capacitive current from measured current.
The conductive current has many fluctuations and has a higher range relative to the conductive current signal in $\text{nA}$ range. Therefore, FFT filtering of the higher frequency is not effective in filtering out distortion from the signal.

The histogram of Figure 4.19 shows the noise patterns recorded by Omicron-1 and Omicron-2 during the half voltage test. The voltage waveform was measured at higher and lower HV arms individually. The green curve on all histograms shows the voltage waveform at the Omicron-1 connection point, and the blue curve on all histograms shows the voltage waveform at the Omicron-2 point of connection. The voltage waveform should be inverted since this shows the HV arm and the plane voltage, and the needle voltage is inverted. (see Figure 3.3)

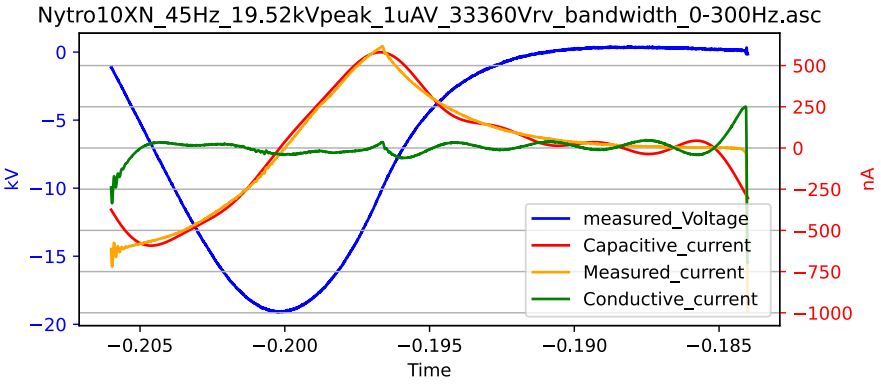


**Figure 4.18:** Measured voltage and current together with capacitive and conductive current calculated for negative half-cycle test


**Figure 4.19:** Histogram of the noise in negative half-cycle voltage test with Omicron 1&2

The histogram in Figure 4.19 shows the pattern of PD pulses happening inside and around the diode. Pattern 5 and pattern 6 in this figure are mostly related to switching high-frequency fluctuations. Pattern 3 and pattern 4 are due to the internal arrangement of uneven surfaces of the HV diode. Patterns 1,2,5, and 6 are easily detectable since they happen close to the zero crossing of the previous sinusoidal HV. Patterns 3 and 4 are in a tricky situation since they are happening around the voltage peak. Histogram of Measured PDs in the negative half-cycle test at $V_{peak} = -12.59\text{kV}$ for $t = 17\text{s}$ seconds has been shown in Figure 4.20.

The green curve in Figure 4.21 shows the voltage of the Omicron 1 at the lower arm. Obviously, the slope of the voltage waveform changes slightly at the moment of switching; therefore, there is a change happening in the resonance circuit of the HV source during the switching process. The blue curve shows the rectified voltage measured by Omicron 2 at the higher arm. it has successfully produced an acceptable waveform. There is a PD pattern excessive to the noise we expected for this experience. At the positive voltage peak (negative peak in the Figure 4.21) between $100\text{pC}$ and $1\text{nC}$. The needle tip radius for this experiment was $3.33\mu\text{m}$, and after the test, the tip radius was $5.95\mu\text{m}$. It appears in a higher voltage than PDIV level with considering needle tip radius. The range of the green and blue curves is adjusted automatically; therefore, the vertical axis is only related to PD incidents and not to the voltage curves. Histogram of the measured PDs in the positive half-cycle test at $V_{peak} = 15.3\text{kV}$ for $t = 17\text{s}$ is in Figure 4.21.

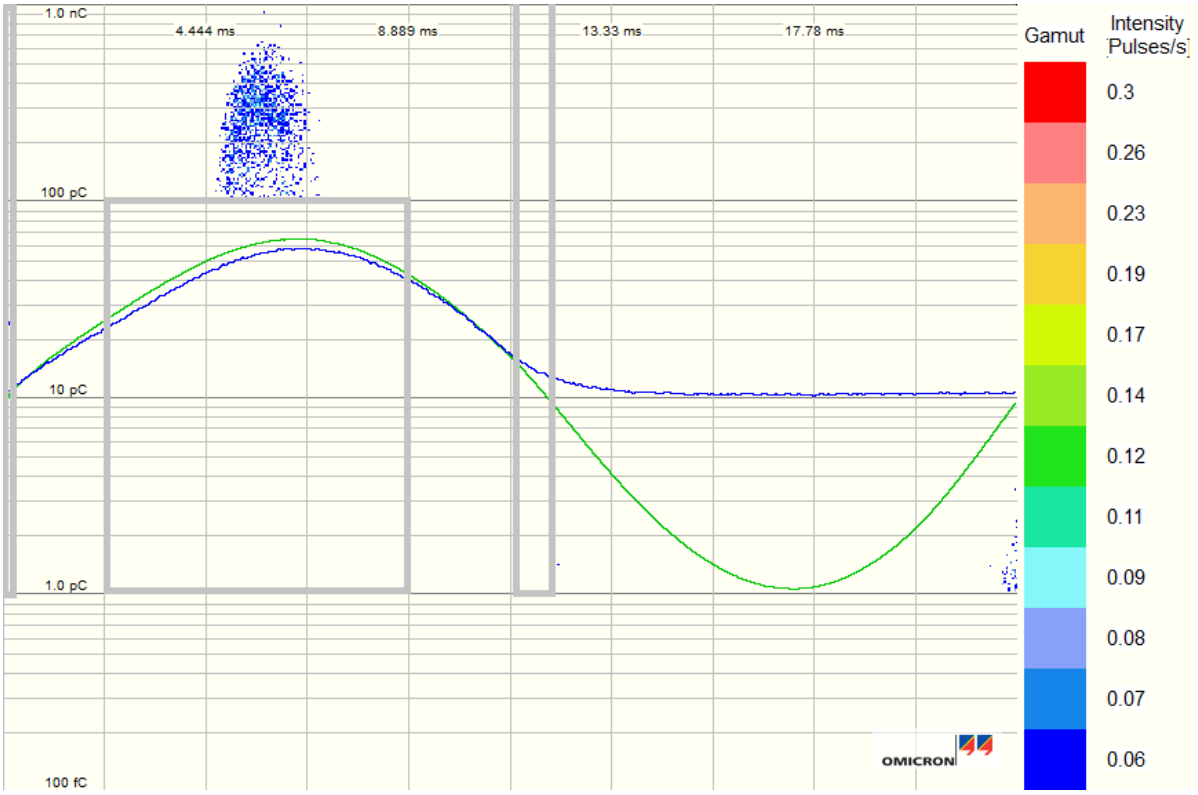


**(a)** Omicron-1 lower arm

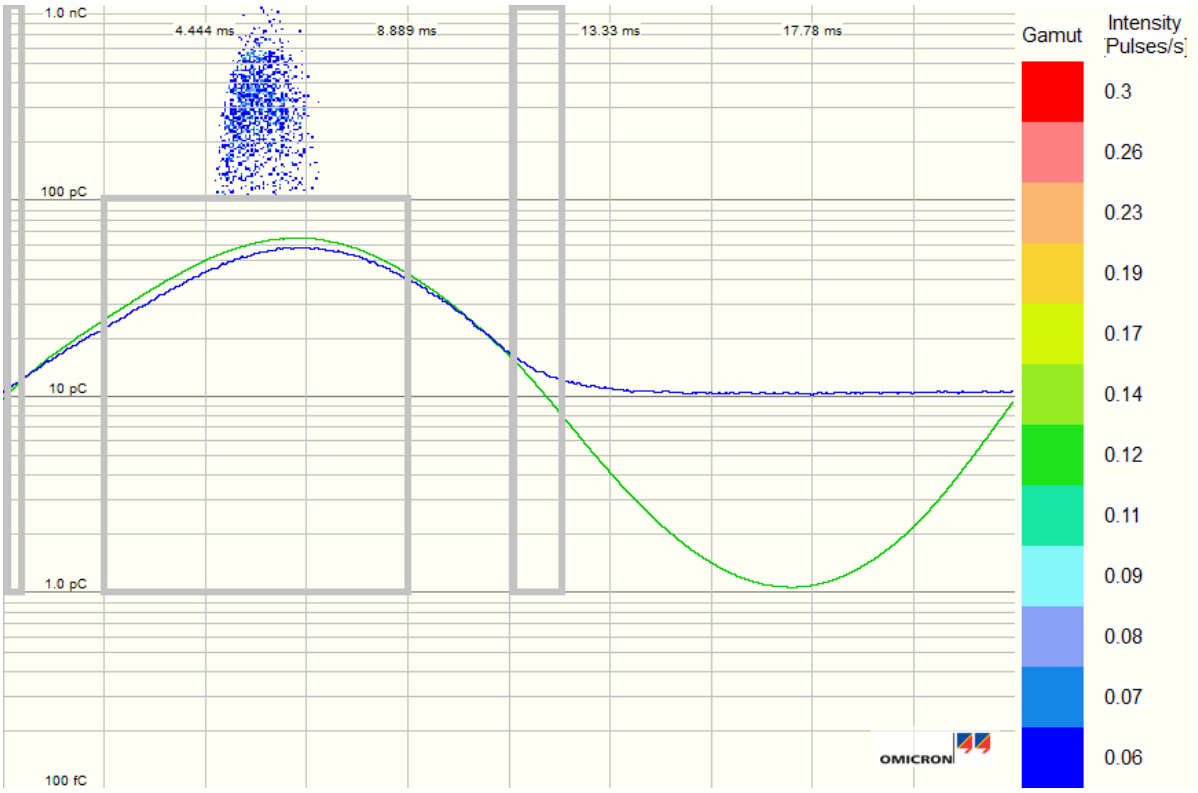


**(b)** Omicron-2 higher arm

**Figure 4.20:** Histogram of the negative half-cycle at $V_{peak} = -12.59\text{kV}$ (gray rectangle shows the filtered out area)

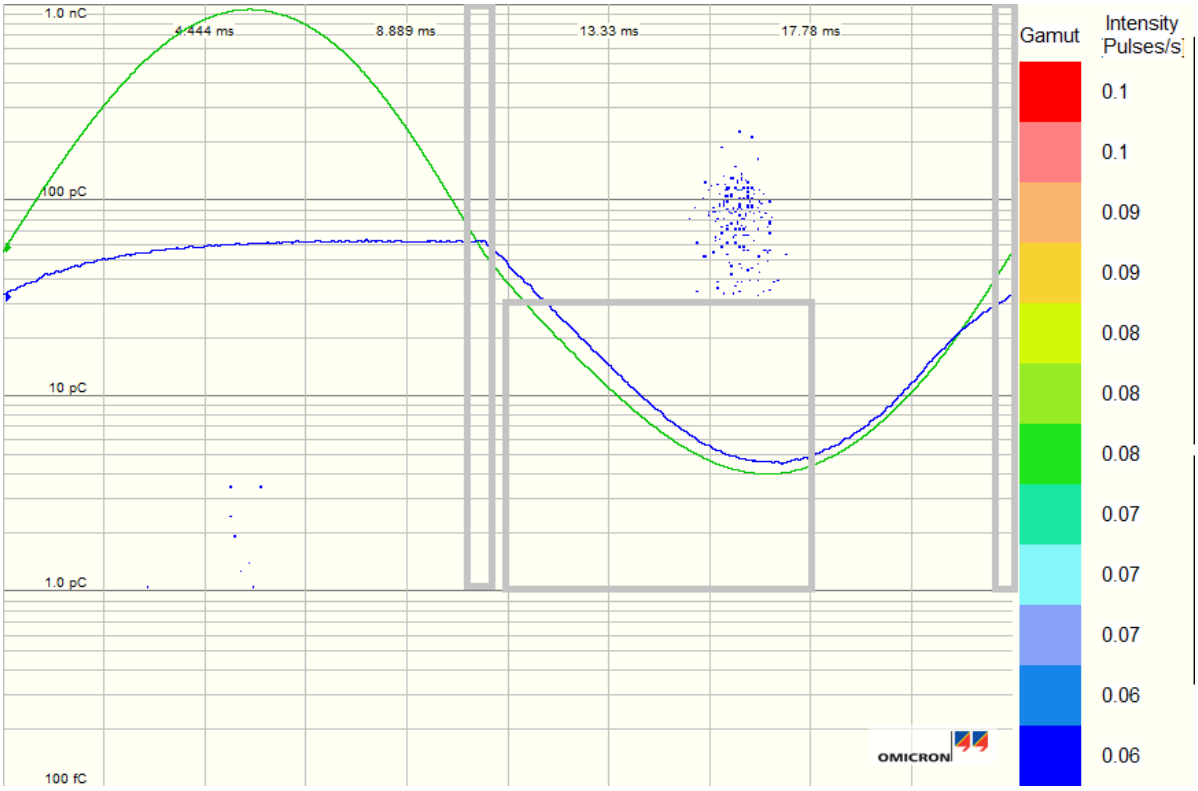


**(a)** Omicron-1 lower arm

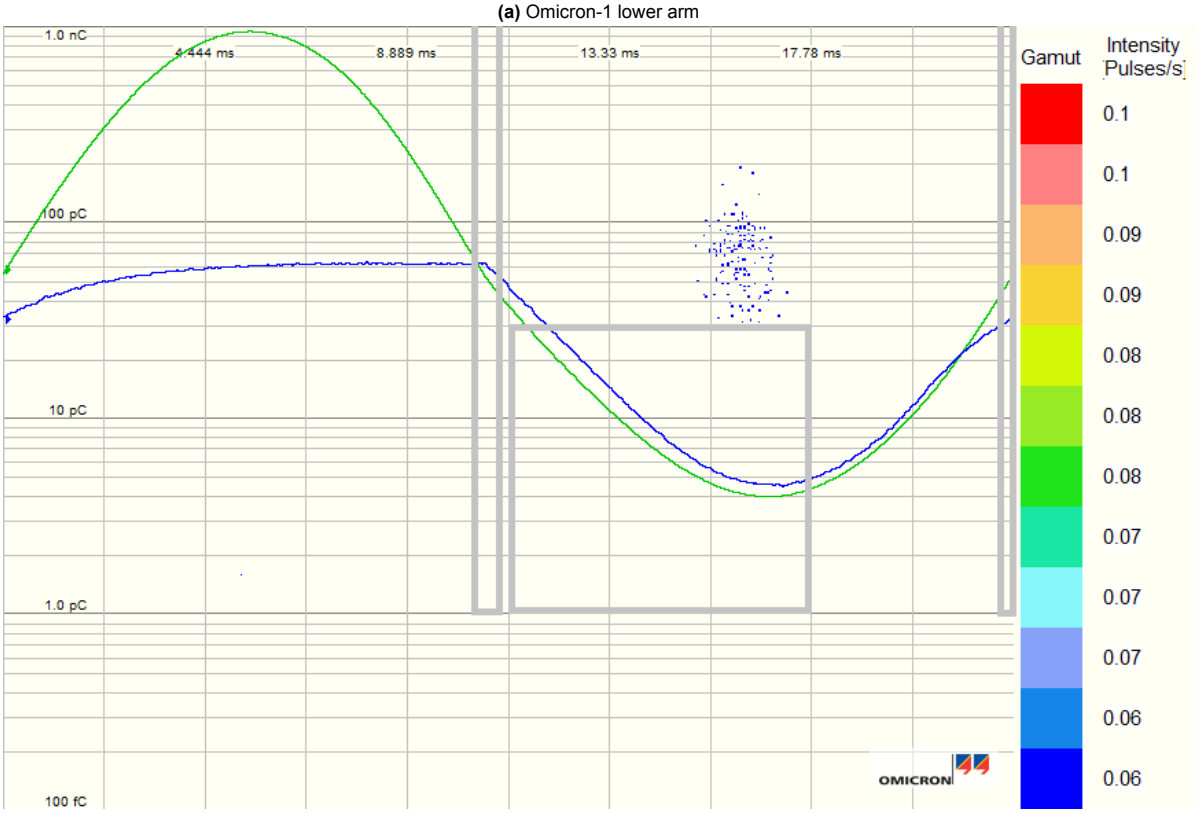


**(b)** Omicron-2 high arm

**Figure 4.21:** Histogram of the positive half-cycle at $V_{peak} = 16.8\text{kV}$ (gray rectangle shows the filtered out area)

## 4.4. Needle Tip Erosion During the Tests

Previous studies show that the needle tip erosion changes when it is under HV tension. (see subsection 2.2.2) Referring to section 2.2, any changes in the needle tip radius affect the maximum electric field drastically in the needle-plane geometry. The rate and the magnitude of this change have been studied in previous research. The importance of those results lies in the geometry and dimensions of the test cell. The same test cell has been used for this study.
Different liquids are tested for needle tip radius change over time and the results have compared with previous studies. There are two hypotheses explaining the main cause of needle tip erosion. First, needle erosion can happen due to reactions with ions being created and dissolved in the region. High electric field effects that are explained in section 2.5, can happen slowly during conductive current flow. Second, PD incidents, including large current pulses happening in a very short time, can be the main cause of the erosion.
In this study, the needle erosion caused by the conductive current will be measured at different voltage levels, both above and below the exponential part of the conductive current (Region 3) and below the PDIV level. The test will be further taken above the PDIV level to the first PD burst. The needle tip radius is measured after the test.

The first observation related to the needle tip shows the change of the needle in time.
For this experiment, the tip radius of the needle is measured as the first action. Then after placement into the test cell, the total time that the needle is being under HV tension is being measured. then, the needle will be measured again, and the changes in the tip radius will be compared with the previous study.

The second experiment has been designed for differing between the conductive current and PD effects on the needle tip.

#### Tip Radius Change Before and After PD

In this experiment, the needle has been sharpened and adequately measured at the first step. Then, it was loaded into the test cell and was put under different voltage steps.
The voltage rose gradually, and the needle was investigated for any changes after being under that voltage step for several minutes. Step voltages go higher and higher until they surpass the PDIV voltage, and the last step is the step where the first PD has been observed.
Nytro 10XN has been chosen for this experiment since it shows relatively good insulation characteristics. $45\,\mathrm{Hz}$ has been chosen since it was closer to grid frequency and exhibited good conductive results in previous tests. The testing procedure was as follows:

1. Needle has been sharpened and adequately measured
2. The test has been taken in several voltage steps lower than PDIV
3. Tip radius has been measured
4. Higher voltage steps applied
5. Tip radius has been measured again

The needle tip radius has been sharpened again for the next test. Measuring the tip radius is being done with the help of a digital microscope, which has been shown in different examples such as in Figure 4.22.
Observations of the needle tip radius in the previous tests begin by considering tests on Cyclohexane with the tip radius of $1.7\,\mu\mathrm{m}$ before tests. After tests, the needle was taken out and measured once again. which has been shown in Figure 4.22. The tip radius of the needle was about $6\,\mu\mathrm{m}$.

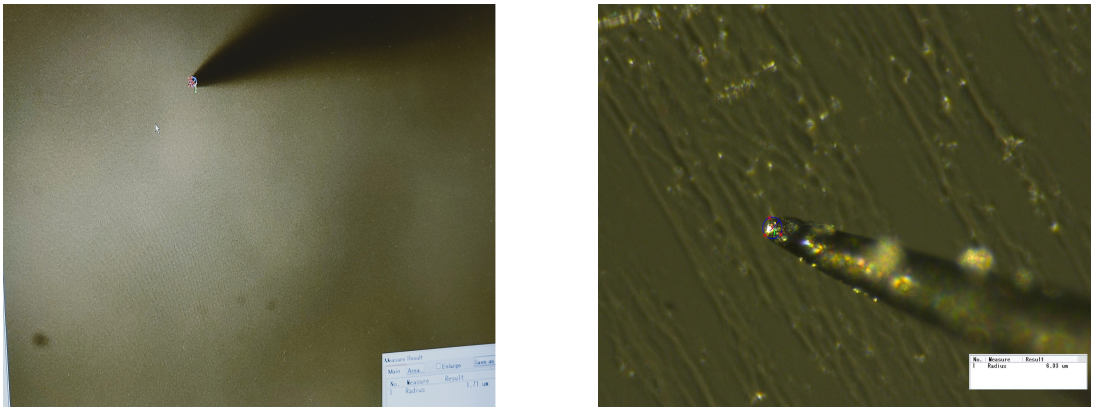

**(a)** Before test $1.71\mu\mathrm{m}$ **(b)** After test $6.03\mu\mathrm{m}$

**Figure 4.22:** Needle tip radii before and after testing Cyclohexane with $30, 45$ and $60\mathrm{Hz}$

Needle tip radii of Nytro 10XN tests is presented in Figure 4.23 The tip radius of the needle in these tests was $5.24\,\mu\mathrm{m}$ at the start and $11.6\,\mu\mathrm{m}$ at the end.
Needle tip photos for tests with Nytro 10XN have been shown in Figure 4.23.

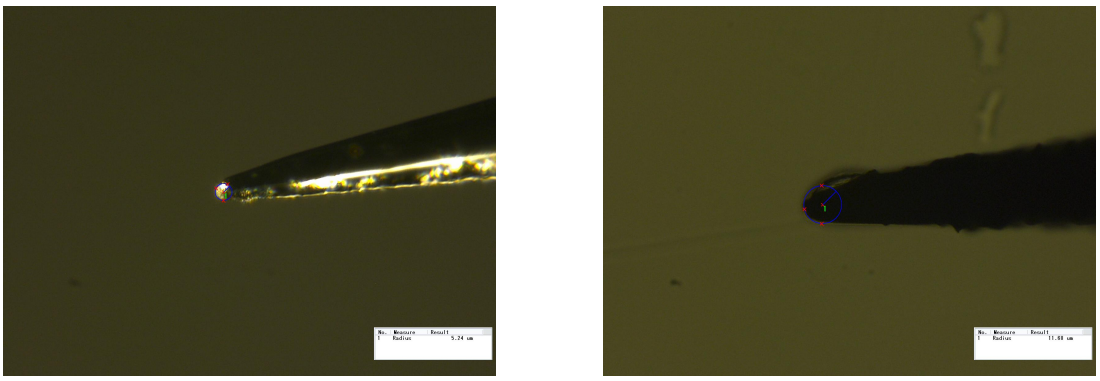

**(a)** Before tests $5.24um$ **(b)** After tests $11.6um$

**Figure 4.23:** Needle tip radii before and after testing Nytro 10XN with $30, 45$ and $60\mathrm{Hz}$

The needle tip has also been measured in testing with MIDEL 7131. The tip radius of the needle before tests was $5.26\,\mu\mathrm{m}$, and after tests, it was $10.4\,\mu\mathrm{m}$.
Needle tip photos before and after tests with MIDEL 7131 have been shown in Figure 4.24.

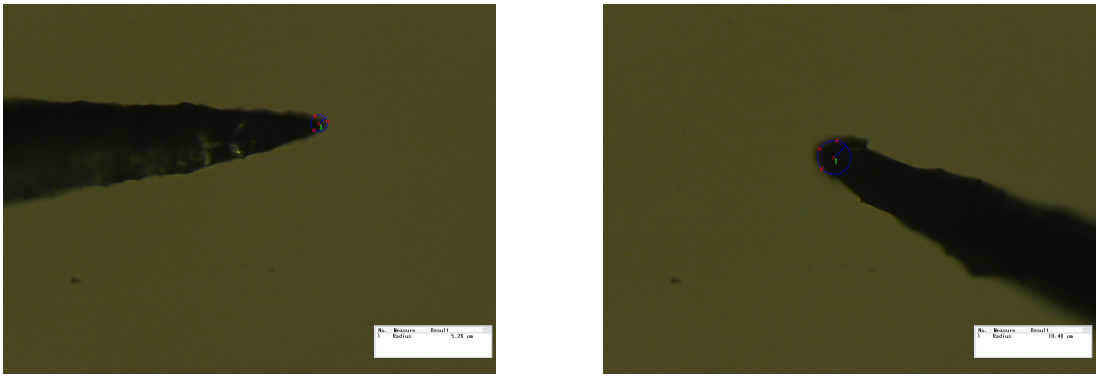

**(a)** Before tests $5.26um$ **(b)** After tests $10.40um$

**Figure 4.24:** Measurement of the Needle tip radii before and after testing MIDEL 7131

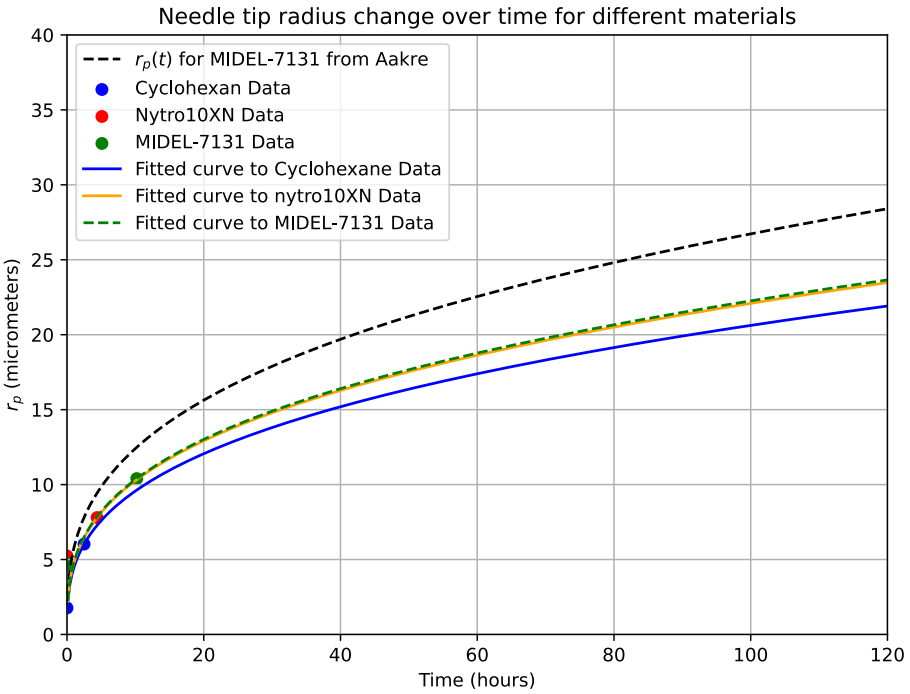


**Figure 4.25:** Needle change over time in different liquids and the fitted curves

It has been observed that needle erosion occurs while putting it under the HV tension, as presented in the previous study. Recording time in Omicron has been used to calculate the accumulative time span of each setup. However, for this part of the work, the tip radius has been measured before and after each liquid test group.
Resulted data points have been fitted to several cubic root functions and have been compared with previous study in Figure 4.25. Data points in this graph are pushed to the left side since the testing time was limited due to practical considerations; however, to show the difference between the curves properly, it has been extended to $120$ hours.

A test has been planned to differ between the erosion caused by PD incidents and by conductive current.
The needle tip radius has been measured before and after each voltage level this time. The needle tip before test has been shown in Figure 4.26a.
It has been installed in the test cell with Nytro 10XN and with a gap distance of $20\mathrm{mm}$. The test cell has been connected to the voltage source with $45\mathrm{Hz}$.
The voltage has been increased gradually in the first test. After increasing the voltage to $2.15\,\mathrm{kV}$, it has been applied for $10\,\mathrm{mins}$. The needle tip was inspected after that. Photo has shown in Figure 4.26d.
In the second test, the voltage has been increased to $9\,\mathrm{kV}$ applied for $14\,\mathrm{mins}$. The needle tip after the test has been shown in Figure 4.26b.

**(a)** Needle tip before test. Tip radius is $1.6\,\mu\mathrm{m}$

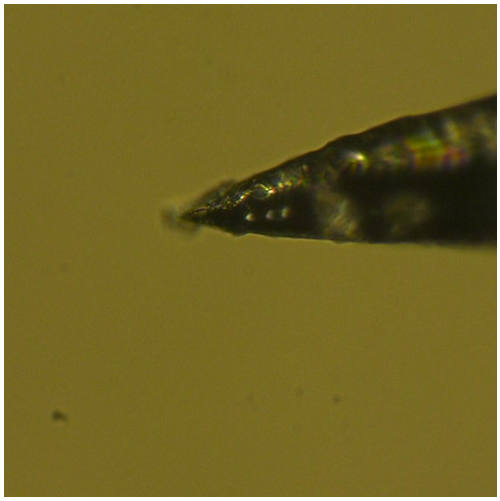

**(b)** Needle tip after the first step. Tip radius is $1.9\,\mu\mathrm{m}$

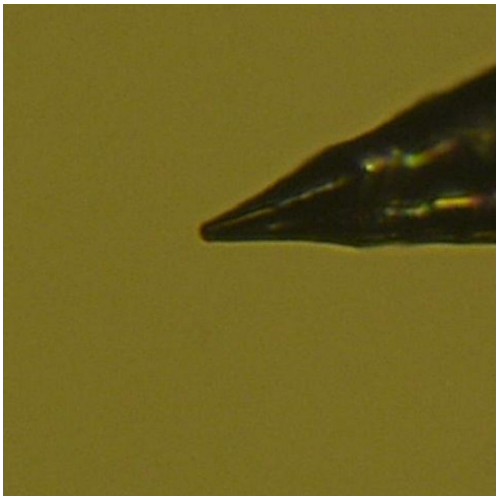

**(c)** Needle tip after second step. Tip radius is $2.01\,\mu\mathrm{m}$

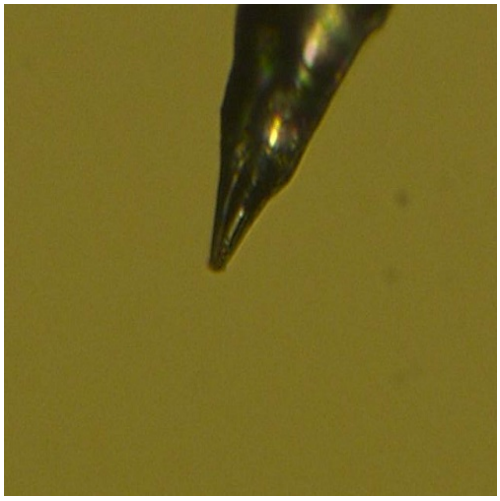

**(d)** Needle tip after third step. Tip radius is $2.19\,\mu\mathrm{m}$

**Figure 4.26:** Needle tip measuring after each voltage step for Nytro 10XN at $45\,\mathrm{Hz}$

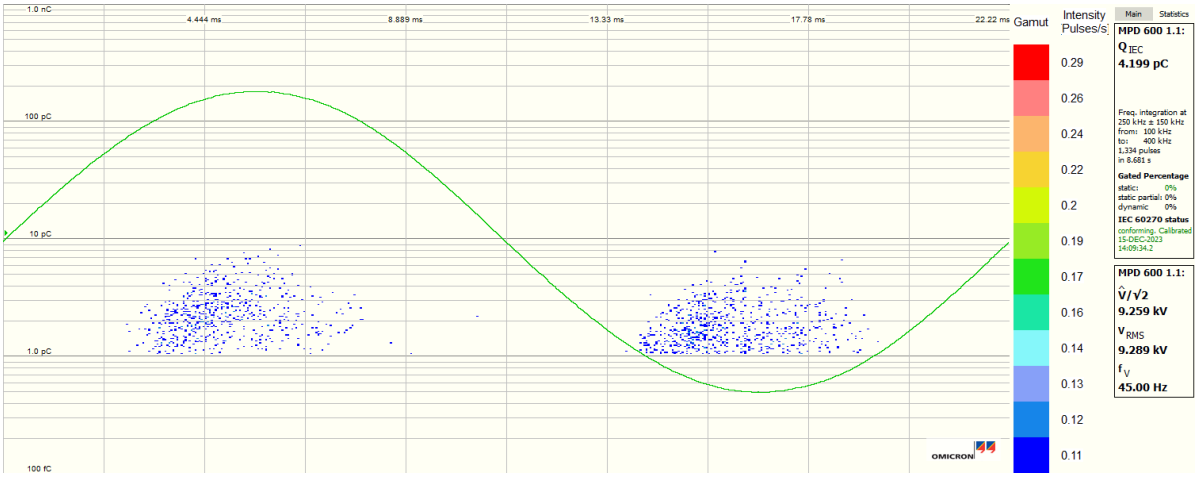


**Figure 4.27:** Histogram of testing Nytro 10XN at 45Hz for needle tip inspection

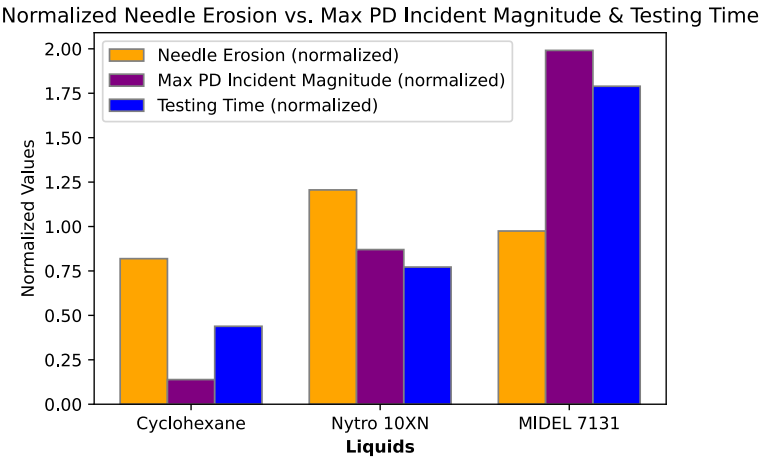


**Figure 4.28:** Normalized needle tip erosion, testing time and maximum PD incident magnitudes

Subsequently, the test proceeded beyond PDIV, to $9.3\,\mathrm{kV}$ and was halted after the first PD burst. The needle tip radius was then measured, as depicted in Figure 4.26c.
The pattern of the first PD burst has been shown in Figure 4.27. There were 1334 pulses measured in $8.6\mathrm{s}$ until the voltage has been cut off. The needle tip inspection result has been shown in Figure 4.26c. The results of these two tests indicate that needle tip erosion occurs during conductive current flow in the liquid, but it predominantly happens during PD incidents. Significant changes in the needle tip radius are observed over longer periods in the first test under HV.
In previous results, considering the PD patterns in Cyclohexane in Figure 4.1, the largest PD incidents are around $30 - 70\mathrm{pC}$, the PD patterns in Nytro 10XN in Figure 4.2, the largest PD incidents are over $100\mathrm{pC}$ and for MIDEL 7131 in Figure 4.3, the largest incidents are around $500\mathrm{pC}$. Comparing these PD incident magnitudes with needle tip erosion has been shown in a bar graph in Figure 4.28. The overall result shows that the needle tip erosion is different in different liquids and is less related to the testing time and Max PD incident value.

## 4.5. PDIV of the Liquids Under Test

According to explanations in section 3.7, PDIV level is not a fixed threshold. Therefore, a specific method should be defined for measuring correct PDIV. According to the defined procedure in section 3.7, The voltage step of the first partial discharge incident larger than $2\,\mathrm{pC}$ is considered as the PDIV level. The voltage will increase gradually in steps. Every step magnitude is $250\,\mathrm{V}$ and is applied for $1\,\mathrm{minute}$.

The histogram of the PDIV test for Cyclohexane in $45\,\mathrm{Hz}$ has been shown in Figure 4.29a. It shows the pattern of PD incidents happening in the earliest burst after passing the PDIV voltage. The voltage has been increased to $13.8\,\mathrm{kV_{RMS}}$ for Cyclohexane, and the PD pattern is recorded for a period of time after PDIV. The PD charge versus voltage has been shown in Figure 4.29b Nytro 10XN and MIDEL 7131 have also been tested after Cyclohexane. The charge versus voltage and histogram have been shown for each one in Figure 4.30 and Figure 4.32. The results of PDIV tests have been shown in Table 4.1. Table 4.1 shows the PDIV levels for each liquid in $45\,\mathrm{Hz}$.
Figure 4.31 shows the bar graph of the PDIV levels in tests with Cyclohexane, Nytro 10XN and MIDEL 7131.

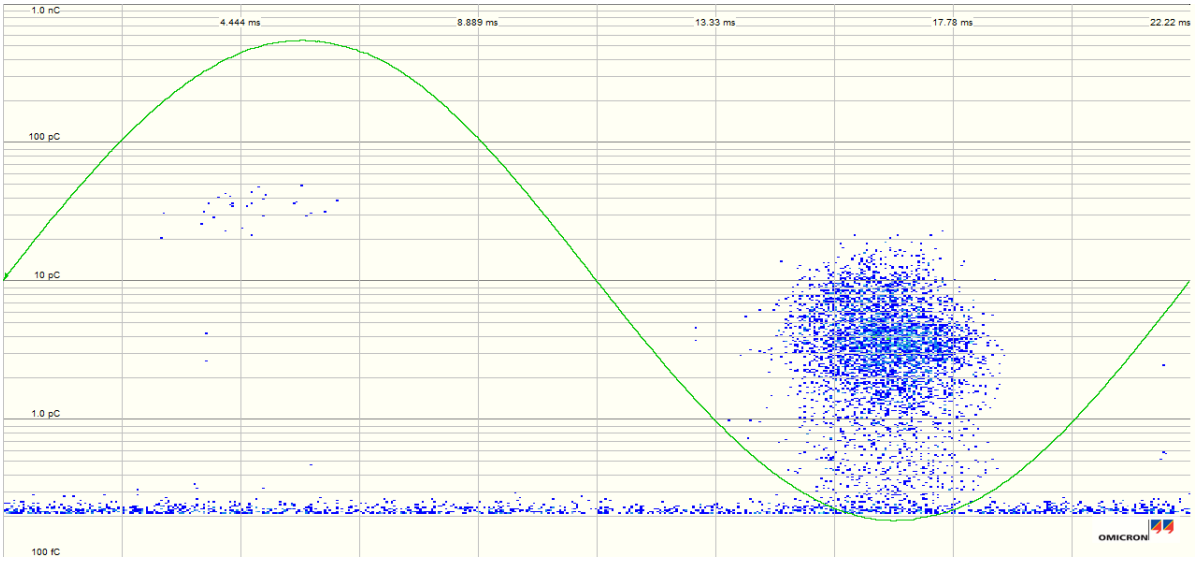


**(a)** PD burst pattern

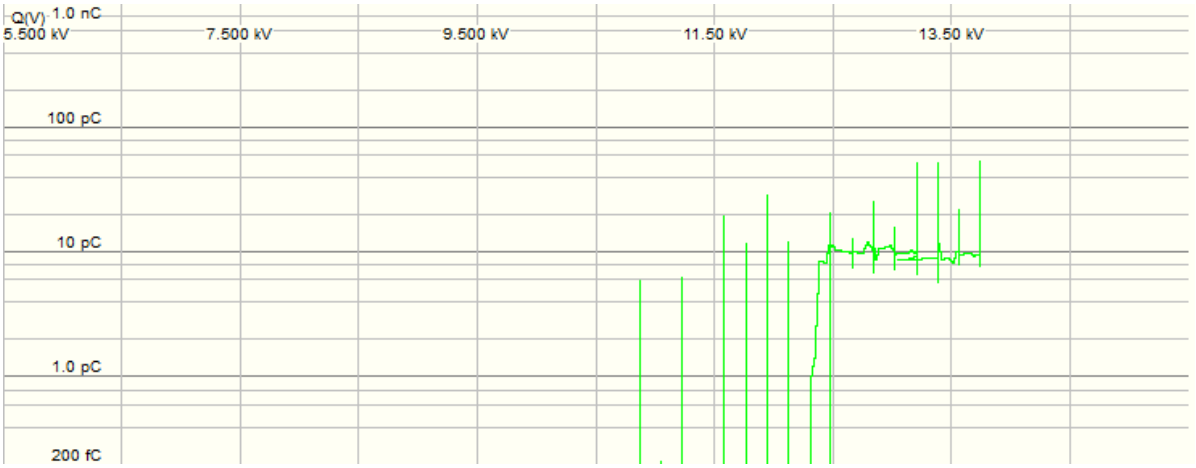


**(b)** PD charge versus Voltage

**Figure 4.29:** PDIV histogram for the Cyclohexane at $45\,\mathrm{Hz}$

**Table 4.1:** PDIV Voltage Level of tested liquids

| Liquid | Frequency | Needle tip radius | PDIV level |
|---|---|---|---|
| Cyclohexane | $45\,\mathrm{Hz}$ | $2\mu m$ | $10.85\,\mathrm{kV}$ |
| Nytro 10XN | $45\,\mathrm{Hz}$ | $5.3\mu m$ | $14.85\,\mathrm{kV}$ |
| MIDEL 7131 | $45\,\mathrm{Hz}$ | $4.5\mu m$ | $13.76\,\mathrm{kV}$ |

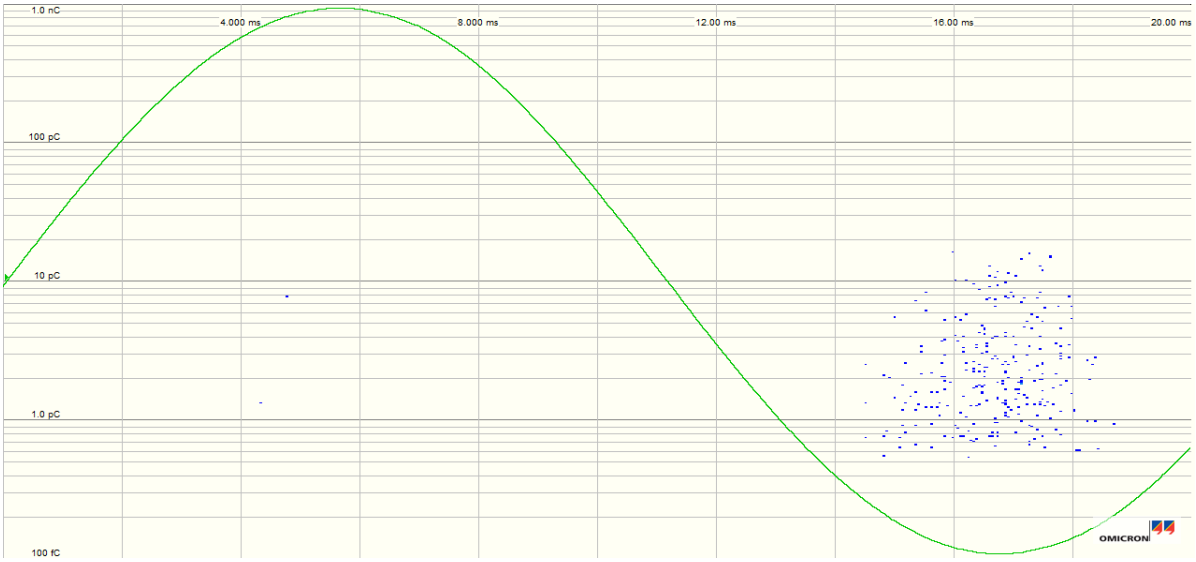


**(a)** PD burst pattern

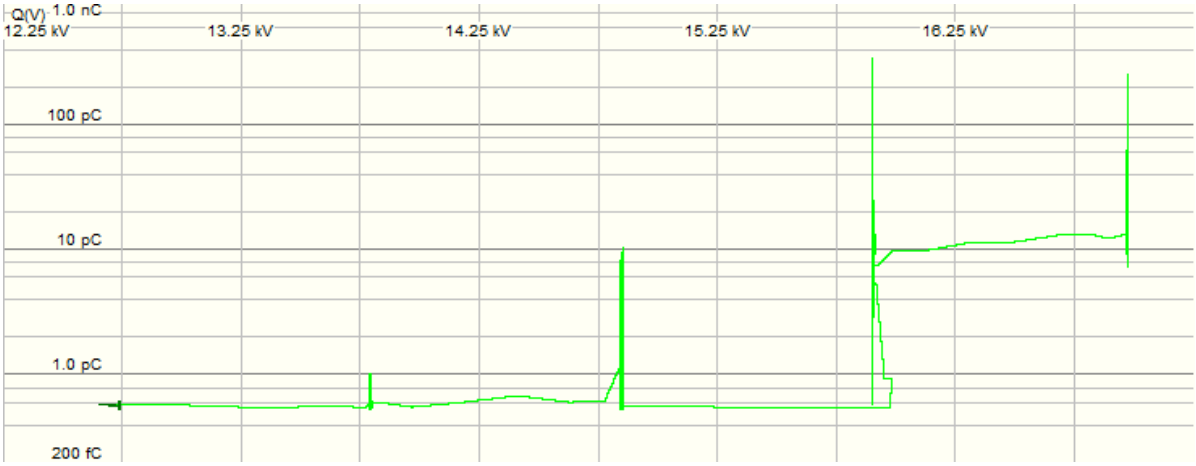


**(b)** PD charge versus voltage

**Figure 4.30:** PDIV histogram for Nytro 10XN at $45\,\mathrm{Hz}$

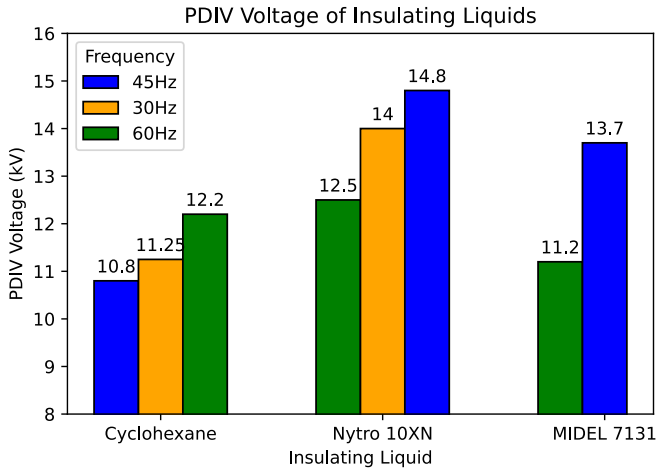


**Figure 4.31:** Bar graph of PDIV of tested liquids

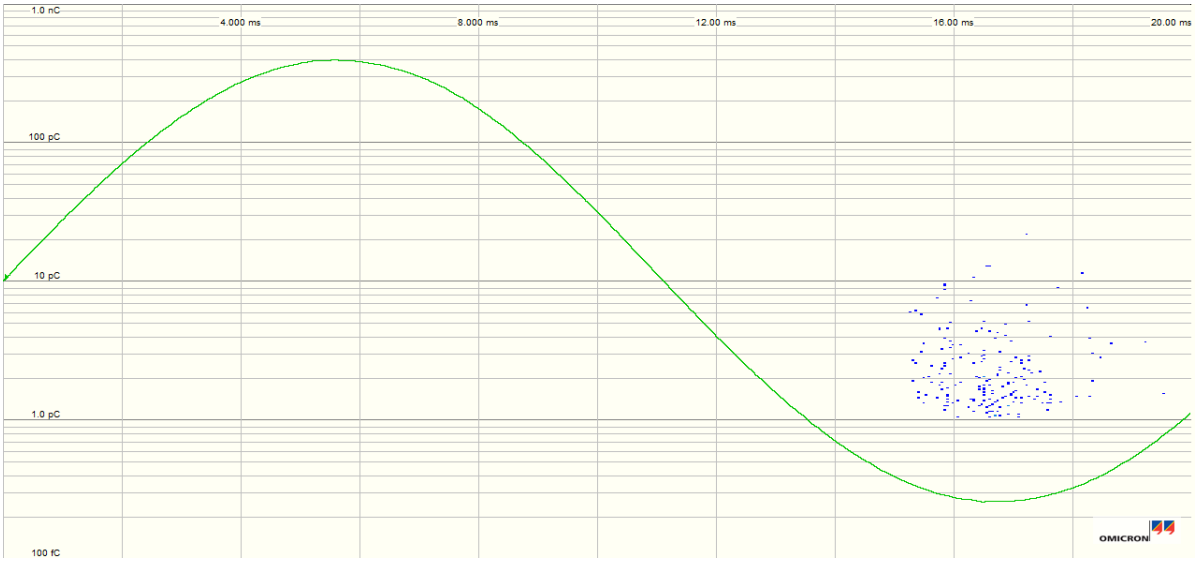


**(a)** Histogram showing the PDs happened after PDIV level

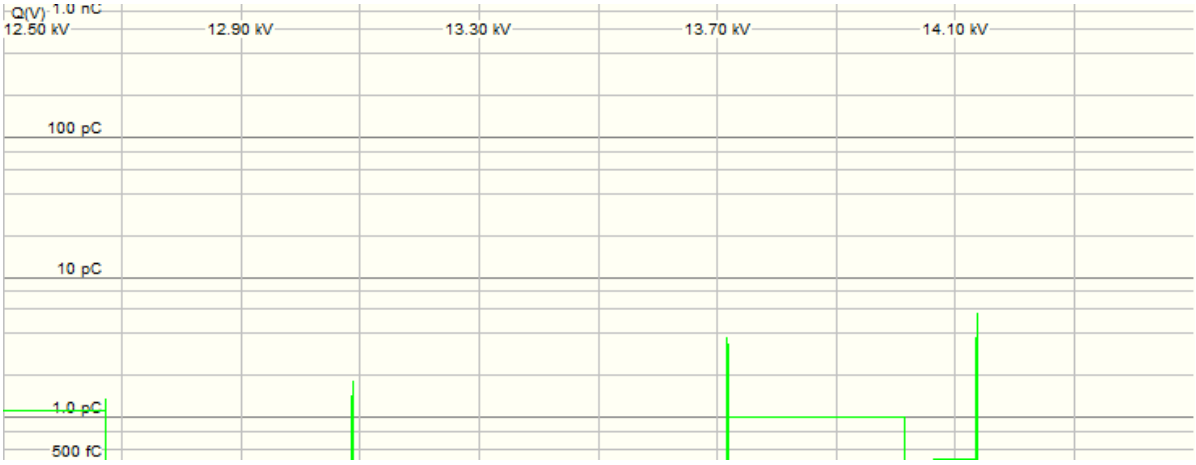


**(b)** PD charge versus voltage

**Figure 4.32:** PDIV MIDEL 7131 at $45\,\mathrm{Hz}$

## 4.6. PD Detection By Optical Method

The optical PD measuring system has been explained in section 3.5. An experiment has been conducted to investigate the initiation stage of the PDs happening in the air from a wire which has been connected to the HV arm inside the test cell.
To facilitate this investigation, the test cell was removed from the test chamber, and a sample wire was positioned on the HV in the air. Subsequently, the voltage was gradually increased to observe PDs. Specifically, an RMS voltage of $5.26\,\mathrm{kV}$ at a frequency of $45\,\mathrm{Hz}$ the first PD incidents occurred. The voltage was kept constant for a duration of $60\,\mathrm{s}$, and the PD pulses were recorded both electrically through an omicron connected to CPL542 and optically through a second MPD600 omicron module connected to the output of the gate module of the coincidence circuit (see section 3.5). The resulting histogram of the test has been shown in the Figure 4.33.
Furthermore, Figure 4.34 shows the same wire has been tested under RMS voltage of $6.32\,\mathrm{kV}$ at the frequency of $45\,\mathrm{Hz}$ for the same duration of time.

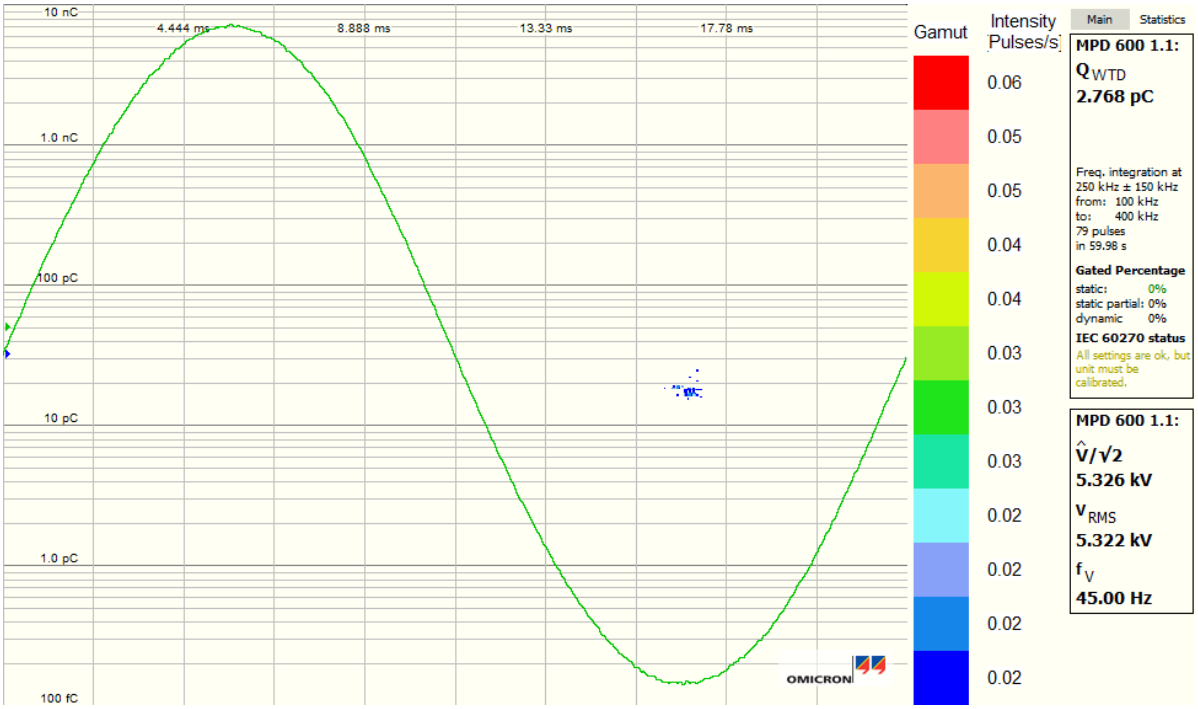


**(a)** Histogram of the electrical PD pulses detected at $5.26\mathrm{kV}$ for $1\mathrm{minute}$

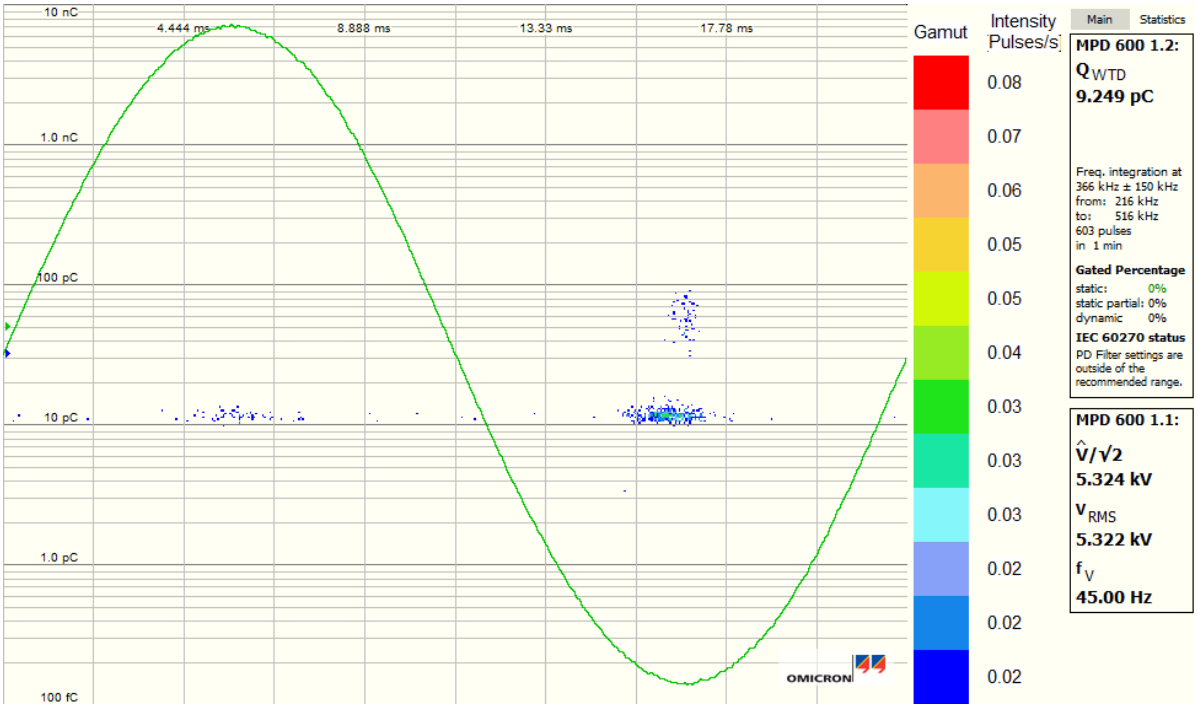


**(b)** Histogram of the optical PD pulses detected at $5.26\mathrm{kV}$ for $1\mathrm{minute}$

**Figure 4.33:** PD measurements by electrical and optical methods around PDIV in air at $5.26\,\mathrm{kV}$

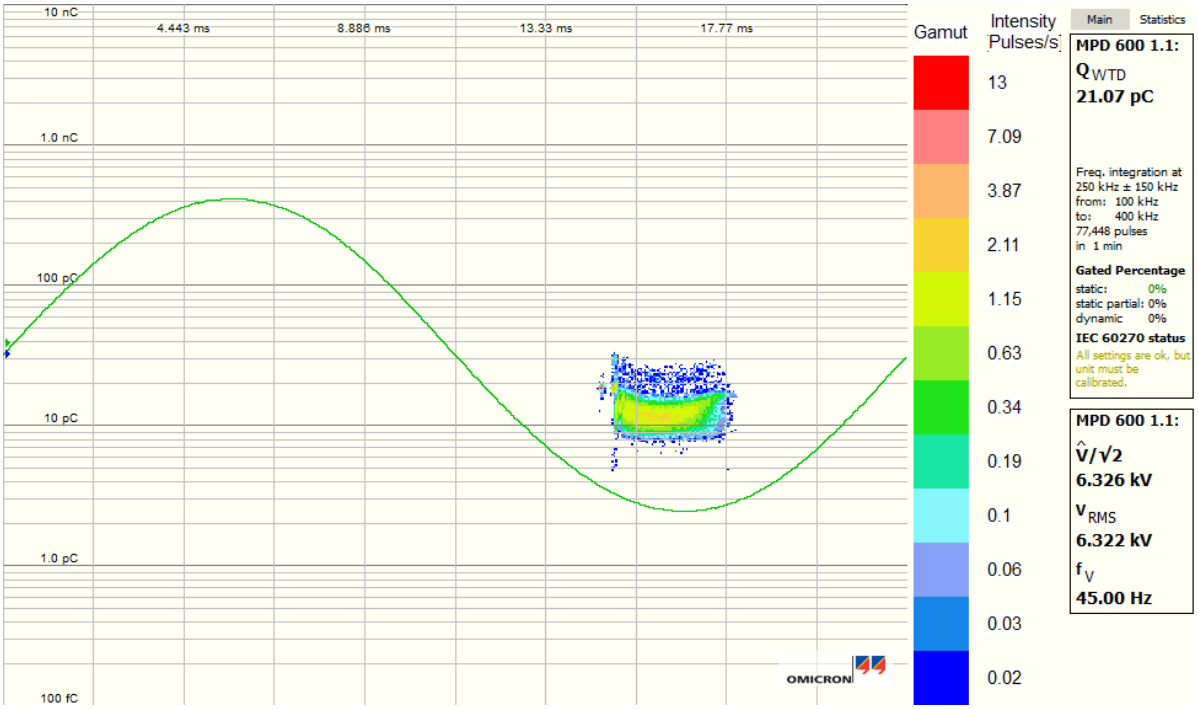


**(a)** Histogram of the electrical PD pulses detected at $6.32\mathrm{kV}$ for $1\mathrm{minute}$

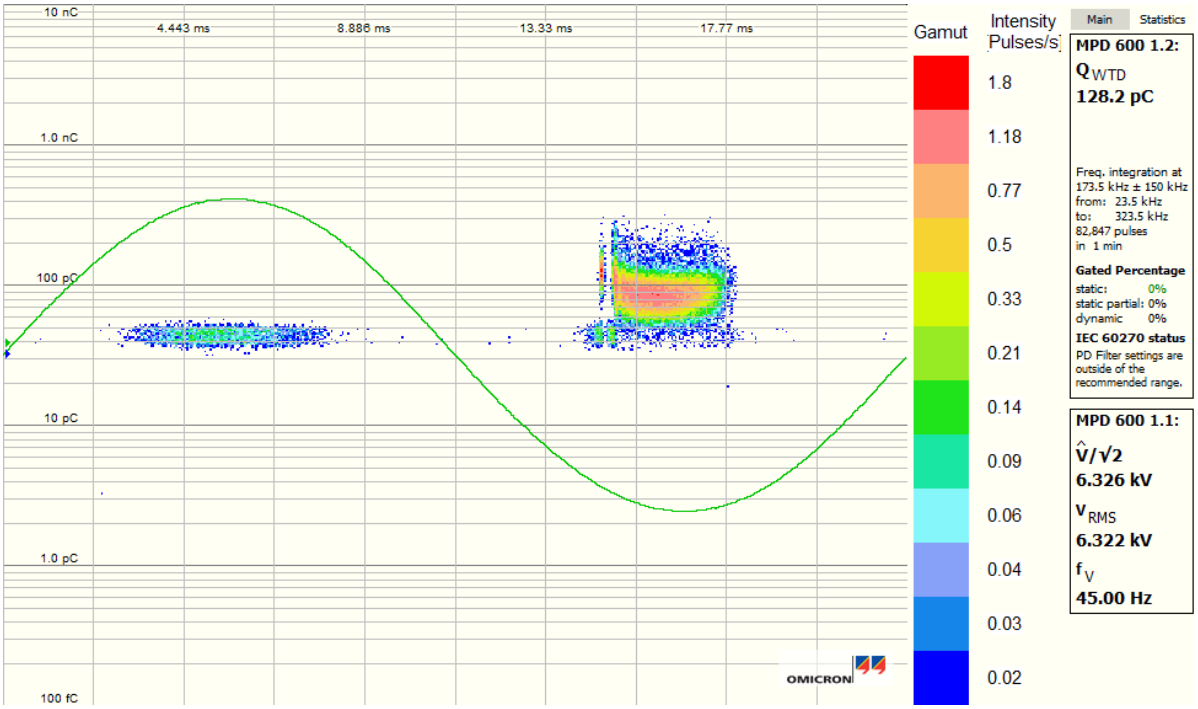


**(b)** Histogram of the optical PD pulses detected at $6.32\mathrm{kV}$ for $1\mathrm{minute}$

**Figure 4.34:** PD measurements by electrical and optical methods around PDIV in air at $6.32\,\mathrm{kV}$

# 5

# Discussion

The mechanism of creating a partial discharge in the liquid causes the formation of space charges in the insulating liquid, as mentioned in section 2.5. The effect of these space charges is discussed in section 2.6. The following part intends to analyse the results from the observations in chapter 4 with the given insight from the space charge mechanism mentioned in chapter 2.

## 5.1. Explaining Space Charge Effect

The concept of space charges as an important phenomenon that initialises partial discharges in insulating liquids is the most interesting part of this work. The quantity or the amount of charge of the space charges in the vicinity of the needle cannot be determined without studying the conductive current. Hence, they become detectable by observing the current flow in this region because of the effect of moving charges and the electric field change carried out in the needle tip. Note that a method to measure space charges directly in practice is missing. Still, the effect of these charges on the field and conductive current flowing in the insulating liquid identifies the presence of these charges.

The effects of space charges in the region were explored previously and investigated by obtaining conductive current from tests with different voltage waveforms as in [23]. However, it was difficult to effectively filter and extract conduction current at high frequency in that study due to the switching of the AC source. As described in section 2.5, various mechanisms effectively produce space charges in the region. The speed with which these space charges move is quite considerable, hence the impression that in previous experiments with low frequencies, it was not possible to catch effects because they are moving fast.
Successfully performing the tests at higher frequencies by changing data filtering methods and using a resonance AC source for the tests in this work made it possible to ponder the nature of space charges in the liquid deeply.

Some analytical results from experimental relations, like fitting data points, have been established based on the theories in section 2.6.

## 5.2. Space Charge Effect on Conductive Current Shape

Analysis of the resistive current extracted from specific sections revealed a distinct pattern of asymmetrical half-cycles in most tests. Notably, this asymmetry appears to correlate with the strength and frequency of the electric field.
To check space charges, it should be noted that the Equation 2.15 shows that the presence of space charges in the region causes current. This current depends on the mobility and strength of the electric field in Equation 2.16. Considering a half-cycle of the conduction current waveform in MIDEL 7131 at a voltage range of about $V_{peak} = 10\mathrm{kV}$ and with the same test conditions and at three different frequencies that are part of the results in the last row of Figure 4.32b and shown in Figure 5.1. The normalised time in this graph has been obtained by

$$\mathrm{Normalized\,time} = \frac{\mathrm{data\,time}}{\tau} = \mathrm{data\,time} \cdot \mathrm{frequency} \tag{5.1}$$

Since data has been shifted in time for $0.02$, the peak of the voltage is at $0.27$, and all current curves are shifted as well.
By comparing the voltage waveform, the two-quarter cycles are clearly different, and this deference becomes more apparent by applying a higher frequency. This difference is due to the difference in the effect of space charges formed in the region. If the space charges in the strong electric field region are considered the red circle in Figure 5.2. It creates in the region and moves towards the cathode because of the strong electric field. In Figure 5.2(b1), the needle has changed the polarity, and the direction of the electric field has also been changed, but the space charge is outside of the strong field region; therefore, the new electric field has less effect on the speed and direction of it. Therefore, it also causes smaller fluctuations in the current.
By increasing the Frequency, the formed space charges in the region have less time to move outside

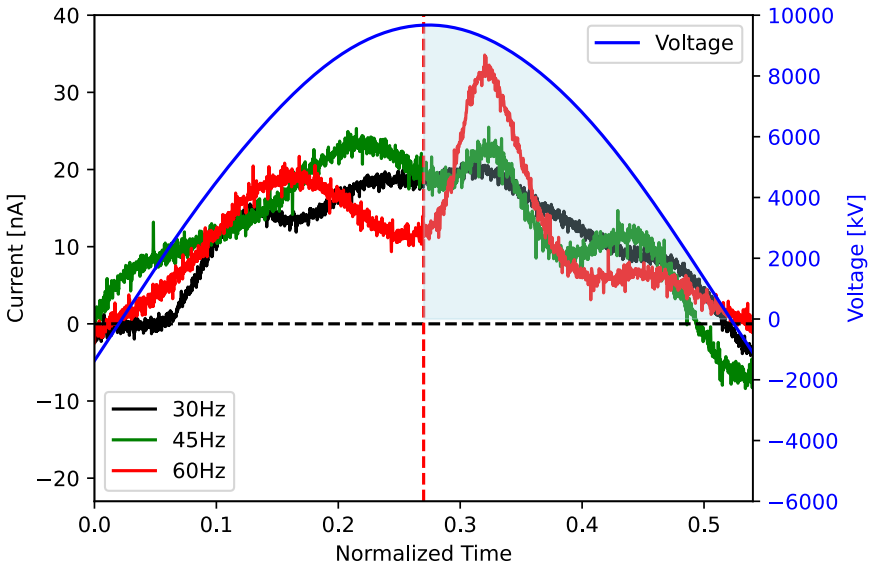


**Figure 5.1:** Asymmetry in the conductive current of MIDEL 7131 at different frequencies

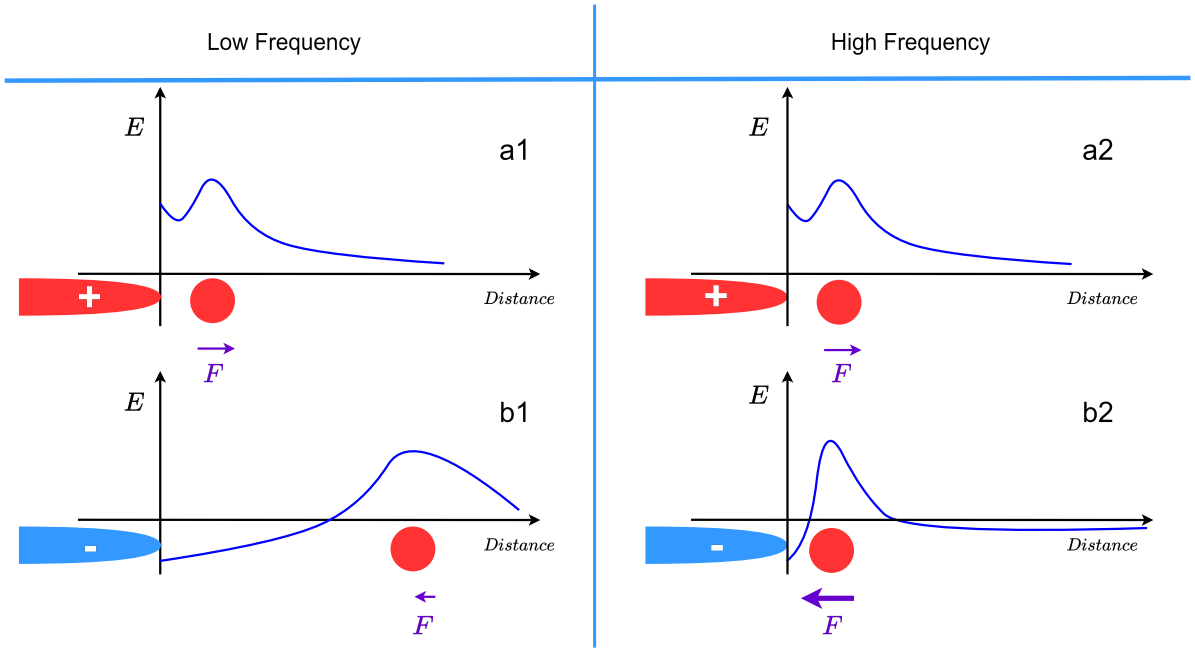


**Figure 5.2:** Drawing showing space charges remaining in the strong electric field region

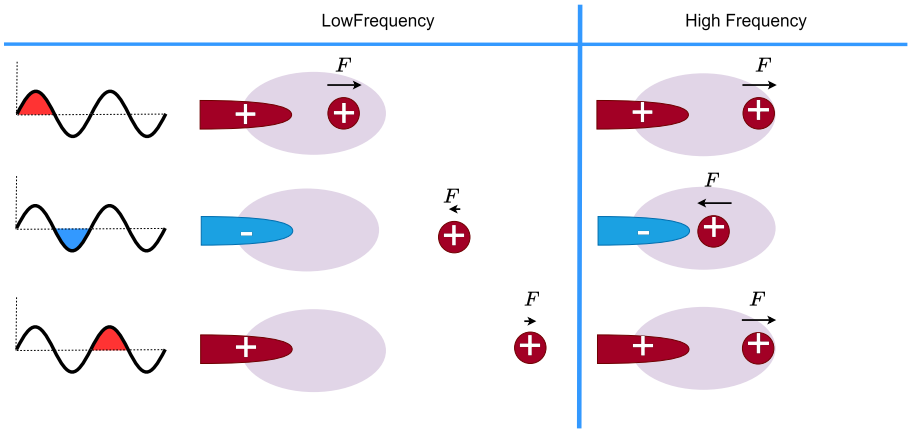


**Figure 5.3:** Drawing showing the behaviour of space charges moving in the strong electric field region

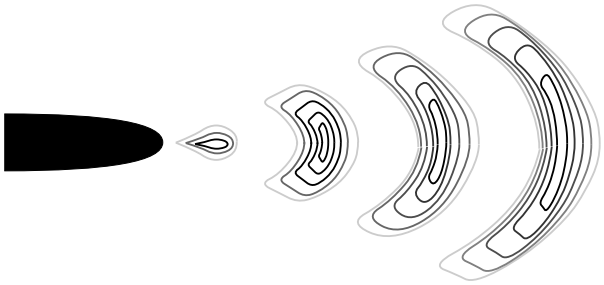

**Figure 5.4:** Drawing Showing different areas of space charge density around the needle tip

the strong field region; therefore, changing the polarity of the needle and electric field has a big effect on the direction and speed of the space charge. This leads to a huge local overshoot in the second quarter of the conductive current waveform, repeated every cycle and for the negative half-cycle.
In the following, assuming that the frequency of the electric field change is large enough to be rival to the speed of movement of space charges in the region, at the same time, the forces applied to space charges and their displacement in the region can change constantly, be in the form of Figure 5.3. It can be seen that increasing the frequency to a certain extent can limit the mobility and range of movement of space charges within the region. This is the cause of different wave shapes in the conductive current waveform.
Considering the movement of space charges as a longitudinal wave propagating from the tip of the needle with drift velocity and the changing electric field in the form of another wave with a certain frequency and with a much higher propagation speed than that. The theory of interference of longitudinal waves may be used for analysing the placement of different areas around the needle with different densities or different polarities of space charges like in Figure 5.4.

## 5.3. Space Charge Effect on the Conductive Current Amplitude

Two different parts with different conductivity (slope) are detectable in all results, such as peak current at different voltages in different liquids.(Figure 4.7, Figure 4.8, and Figure 4.9)
Region 1 at low voltages, the current shows a linear behaviour with voltage similar to Equation 2.17, but at further increasing fields, which causes the formation of space charges in the region; therefore, these space charges change the electric field inside the region, and hence, the conductive current becomes more nonlinear according to Mott-Gurney's law that has given in Equation 2.15.
The geometry considered for this relation is plane-plane. Hence, tests have been taken on a needle-plane geometry; therefore, there is no way to compare the values from the test using this relation.
However, comparing what is available from these relationships, the trend of the conductive current demonstrates a clear agreement with the theory.

This shows that the form of electrodes affects the resistance value between conductors, but the trend is the same.

The peak current waveform in all results changes earlier or in lower voltage by increasing the frequency. This agrees with the hypothesis that higher frequency causes more space charges to stay in the region around the needle tip. Therefore, the space charge effect can be seen earlier in the conductive current. On each of the three tests, the peak value of the main component of the conductive current has also been drawn side by side with the absolute peak current to be able to differentiate between the peak value of high pulses and the overall trend of the conductive current. For example, the negative part of the absolute peak current in Figure 4.8 and Figure 4.7 at $60\,\mathrm{Hz}$ are showing large deference due to PD incidents recording during the tests.
Focusing on the Figure 4.7, which shows the absolute value of the peak current for Cyclohexane in negative and positive peaks of the voltages. The reason for the large overshoot in the negative current peak at $60\,\mathrm{Hz}$ at a voltage above $7\,\mathrm{kV}$ is due to a PD incident that happened during the current measurement.
The only inconsistency that can be raised with the presented hypotheses is regarding the shape of the peak curve of Nytro 10XN in Figure 4.8. The reason affecting this test is the different tip radius of the needle between different tests for this liquid.
In the test at $45\,\mathrm{Hz}$, a smaller needle tip radius ($1.8\mu\mathrm{m}$) has been used other than the needle for $30\,\mathrm{Hz}$ and $60\,\mathrm{Hz}$ tests. ($5.3\mu\mathrm{m}$)
This caused the difference in the electric field strength and the region in front of the needle, reflected in the graphs.

The results for the MIDEL 7131 in Figure 4.9 show the expected behaviour better since the test has been done with the same needle and it has been tried to keep the testing time as short as possible to lower the erosion of the needle tip.
The peak of the main component versus voltage for MIDEL 7131 shows the same trend in the Figure 4.9.

Based on the discussed results, the peak value of the conductive current is related to the electric fields and frequency of the test for all three liquids. Another factor that also plays a critical role in the peak current value is needle tip radius; therefore, in Figure 4.10, the peak current versus voltage steps have been drawn for Nytro 10XN with different needle tip radii.
It shows that the non-linear part of the conductive current related to region 2 at Figure 2.9 happens more or less in all tested insulating materials. Therefore, the amplitude of the conductive current is a function of the insulating material molecule, the strength of the applied electric field (tip radius and voltage), and frequency. But the field strength seems to be a more important factor since different liquids (Nytro 10XN and Cyclohexane) in Figure 4.10 and Figure 4.7 are showing quite close peak values at the same tip radius.

## 5.4. Residual Space Charges and Their Impact on Subsequent Current Waveforms

In further exploring the impacts of space charges on the measured current, it's noteworthy to mention previous findings indicating a link between the peak current of the conductive current in the cycles following a PD incident.
As depicted in Figures 4.11 to 4.15, the conductive current exhibits a notable alteration in peak current following a significant PD event. Specifically, the behaviour observed is characterised by an increase in peak values of the conductive current of the negative half-cycle of the following waveform. It follows an exponential decrease in most of them.
Obtaining the theory of the mobility of space charges from the region makes it possible to fit analytical curves to the current peaks in the subsequent PD cycles.
The exponential factors derived from the fitted exponential curves according to Equation 5.2 for each graph are elucidated in the Table 5.1.

Remarkably, the influence of space charges mostly impacts the negative half-cycles while leaving the

positive side unaffected. However, in Figure 4.14, The same trend has also been detected on the positive side.

$$y = a_{fit} \cdot e^{b_{fit}x}, \tau = \frac{1}{b} \tag{5.2}$$

**Table 5.1:** Exponential function Values and Time Constants

| Liquid | Frequency | a | b | $\tau\,[ms]$ |
|---|---|---|---|---|
| Cyclohexane | 30Hz | $-107.54$ | $-7.71$ | $129.7$ |
| | 45Hz | $-27.96$ | $-8.47$ | $118$ |
| | 60Hz | $\pm 660.41$ | $-18.68$ | $53.5$ |
| Nytro 10XN | 30Hz | $-54.65$ | $-7.89$ | $126.7$ |
| | 60Hz | $-204154.8$ | $-11.91$ | $83.9$ |
| MIDEL 7131 | 60Hz | $-103.51$ | $-4.95$ | $202$ |

### 5.4.1. Needle Tip Radius Change Over Time

The experiments demonstrate that the test results are susceptible to variations in the tip radius of the needle. Because the tip radius of the needle plays a decisive role in producing the highest electric field in the needle-plane region. From section 2.2 resulted that electric field strength depends more on the curvature of the needle tip radius than its distance from the plane. The maximum field strength is of the most importance for the PD test in needle-plane geometry.

Following the study done by T.G.Aakre, the tip radius of the testing needle changes over time during the test [23]. A test procedure has been developed to inspect the needle tip radii over time.
It has been described in detail at subsection 2.2.2. Tests have been done on three different liquids, and results have been shown in Figure 4.25. In addition, a cubic root function was fitted to the data from each material separately. Cubic root function has been suggested in previous studies. Therefore, this form of function has also been used in this study. The mathematical form of this function is at Equation 2.28, and different constant parameters obtained for each curve have been gathered in Table 5.2

**Table 5.2:** Constant Value of the Cubic root function fitted

| Liquid test Data | Constant value |
|---|---|
| Previous study MIDEL 7131 | 400 |
| Cyclohexane | 183.63 |
| Nytro 10XN | 255.8 |
| MIDEL 7131 | 231 |

The final result from the needle tip radius inspection in section 4.4 defines that the needle tip radii are unaffected by the testing liquid according to the results of the three voltage levels before the PD incident in Figure 4.26a, Figure 4.26d, Figure 4.26b and Figure 4.26c.
When the conductive current has been passed through the liquid. In the voltages above PDIV, the undiluted facts appear to be that PD events with amplitudes smaller than $10\,\mathrm{pC}$ do not substantially impact the alteration of the radius of the needle tip. Therefore, when compared, $1334$ PD incidents under $10\,\mathrm{pC}$ that happened in $8\,\mathrm{s}$ with the fact that testing Cyclohexane with around $150$ minutes of high voltage with several PD events of more than $10\,\mathrm{pC}$ significantly alters the needle tip. In conclusion, The needle tip is unaffected by such a test as long as the PD events are not so large.

## 5.5. Space charges Effect in Rectified voltage Regime

The half-cycle test aimed to examine the effects of space charges in the case of the field only in one direction. This observation is important in several ways

1. With this observation, the polarity of the formed space charges in the region can be found
2. It can also give a good insight into the contribution of positive and negative polarity of the needle to forming space charges
3. By comparing the results of this test, which only includes the field in one direction, with the previous results in two directions, space charge movement can be investigated more

The measured and filtered voltage waveform has been presented in the Figure 4.16. The filtered voltage can follow the measured voltage by detecting higher-order frequencies. Still, unfortunately, it does not follow the cracked point in the voltage waveform very well when turning off the diode D1. The reason for this can be the limited ability of FFT filtering in nonsinsoidal cracked points of the waveform.
The data from the digitiser before being processed looks like Figure 4.17. It clearly shows some high-frequency oscillations due to parasitic elements in the circuit, which can also be detected in the histogram at Figure 4.19. Patterns 1,2,5 and 6 are considered to be because of the high-frequency noises due to the switching of the diode D1. There are two more parasitic PD patterns (3 and 4)due to the poor structure of the diode. They start at voltages higher than $V_{peak} = 10.43\mathrm{kV}$, which could not be eliminated on positive or negative half-cycle tests.

It can be seen in the Figure 4.20 that the partial discharge at the negative peak of the voltage (which occurs at the positive peak in this histogram) with a size greater than $100\,\mathrm{pC}$ in the liquid, this partial discharge occurred at a higher voltage level than the corresponding partial discharge in the Full cycle mode. Correspondingly, a positive half cycle has been tested in the Figure 4.21 histograms, and in this test, partial discharges with a magnitude greater than $100\,\mathrm{pC}$ can be seen at the positive peak of the voltage (in the histogram it is displayed as a negative peak). Unfortunately, due to the high disturbance in the results of the histograms in both figures due to the structure and switching of the diode on the sinusoidal voltage waveform of the source, which can be seen in the green curve in Figure 4.19. It is impossible to draw a complete and reliable conclusion from this test, and it can only be briefly stated that the application of a half-cycle of voltage in both positive and negative states has increased the inception voltage of partial discharges in the insulating liquid.

## 5.6. Optical Detection of PDs

In the explanation of the experiment conducted in section 4.6, it was mentioned that two separate measurement methods were used simultaneously to measure partial discharge with electrical and optical methods. An electrical method based on ABC-circuit, which has been explained in section 2.9 and an optical method devised using PMTs and coincidence circuit described in section 3.5. But as stated in the description of the test in section 4.6, the voltage of the wire was raised step by step to reach the first PD pulse, and then the voltage was kept constant, and PD measurement continued for a minute. However, according to the existing assumptions, it is expected that the PD will start from the negative peak, and then it will be seen at much higher voltages in the positive peak of the voltage.
Considering Figure 4.33 and Figure 4.34, the PD pulses happened approximately in the same phase angle (the delay is negligible), but the pulse amplitude in optical measurement is relatively higher than electrical. Considering that the optical pulse amplitudes are dependent on many aspects, such as the gain of the PMT, the shape of the pulse, and the equivalent resistance of the circuit from the PMT side. The MPD600 has not been calibrated to the PMT pulses; therefore, the amplitude of the optically measured PD incidents can not be trusted.
The results of the electrical measurement are in accordance with the assumptions, but the results of the optical measurement are contrary to the existing assumptions and show that the PD starts simultaneously at the negative and positive peaks of the voltage. The correctness of the output of the optical measurement circuit has been researched with the tests mentioned in section 3.5, and it seems that

the PD starts at the positive and negative peaks of the voltage simultaneously, but for some reason, in the electrical PD measurement, the first electric PD pulses appear only in negative voltage peaks. This test has also been performed at a higher voltage level, the results of which are shown in Figure 4.34. These results also show the presence of light pulses at the needle tip in the positive peak of the voltage, which was not recorded in the electrical measurement using the ABC-circuit method. This is a phenomenon that should be further investigated in future studies.

### 5.6.1. PDIV

The PDIV voltage of insulating liquids in different frequencies in Figure 4.31 shows a higher PDIV level for the Nytro 10XN than MIDEL 7131 as it is obvious in both $45\,\mathrm{Hz}$ and $60\,\mathrm{Hz}$. The PDIV level for Cyclohexane is relatively lower than other liquids. One of the most possible reasons might be that the needle tip radius in Cyclohexane was smaller than Nytro 10XN and MIDEL 7131 during the tests. According to the results presented in section 4.4, the needle tip erosion causes considerable changes in the needle tip radius. The sorting of the bar graph in Figure 4.31 is according to the testing order, and it is obvious that the PDIV level is affected more by the needle tip erosion between tests other than frequency or molecule.
The patterns of PDs in figures 4.29a,4.30a and 4.32a to compare with PD pattern of each liquid in Figure 4.1, Figure 4.2 and Figure 4.3. Comparing these two groups shows the same pattern for each liquid, thus validating the PDIV test in liquids.
An important result obtained from the half-cycle tests is that PDIV peak voltage and the magnitude of PD incidents have been increased in the half-cycle mode. This increase in the magnitude of PD pulses is more in the negative half-cycle, and it shows the effect of space charges in the region on the PDIV level.

### 5.6.2. Comparing Results With IEC 61294 Process

IEC 61294 is a standard that has been defined to find out the PDIV of insulating liquids. The procedure measures the inception voltage for a large PD with a voltage increment rate of $1\mathrm{kV/s}$.
Due to uncertainty in the PD activity, the PDIV test might not correctly reflect certain insulation rates for different liquids.
An example of this uncertainty in PD behaviour is evident in the experiments conducted in this research. According to the results of maximum conductive current in Figure 4.7,Figure 4.8 and Figure 4.9, it seems that the change in conductive current from region 2 to region 3 according to the conduction diagram in insulating liquids in Figure 2.9 happens at relatively same field strength at the field corresponding to $7\,\mathrm{kV}$. The PDIV level in liquids is considered to be proportional to the level of space charge formation voltage. Therefore, PDIV determination in the IEC standard is uncertain due to the different PD patterns of different liquids. Multiple testing is recommended in the IEC 61294 test procedure, but the PD pattern of the liquid is in favour of or against passing a dielectric liquid. The results of PD patterns for these liquids are shown in Figure 4.1, Figure 4.2 and Figure 4.3. The probability of $100\,\mathrm{pC}$ pulse occurrence is different in time. For example, for MIDEL 7131, in measuring the maximum PD in all three frequencies, the threshold level of the IEC standard has been exceeded, but for Cyclohexane, the PD occurrences are more often but all below the threshold determined in the IEC standard. In comparison, It is also important that the conductive current in the voltage range of $10\,\mathrm{kV}$ and frequency of $60\,\mathrm{Hz}$ in Cyclohexane can be much larger than the conductive current in MIDEL 7131 or Nytro 10XN, which of course is expected in this test with the radius of the needle tip being smaller in the Cyclohexane test. But contrary to the expectations, PD pulses are larger in MIDEL 7131, which seems to have caused inconsistent results regarding the determination of PDIV.

# 6

# Conclusion and Future Work

## 6.1. Conclusion

This study has investigated the PD characteristics of different insulating liquids and the connection of space charges with the initialization of PDs. The main purpose was to experiment with the behaviour of space charges and investigate the effect of their presence on the initiation of PDs in both regular and newly developed insulating liquids.
Evidence of the existence of space charges during the formation of PDs in insulating liquids has been presented. It has shown, with the help of the half-cycle rectified HV source, that space charges include different polarities. It has also shown that the speed of movement of space charges does not depend on the frequency of the applied voltage and is more a function of the type of molecule.
The effect of space charges on conductive currents has been well studied and compared, and new paths have been created to investigate their nature. A more efficient method, using an FFT filter, is used to extract conductive current in insulating liquids. It has shown that the changes in conductive current caused by space charges are non-linear, and the presence of space charges caused by the PD event in the domain causes changes in the conductive current for some time. The effect of space charges on current waveforms has been successfully demonstrated in multiple cycles after a PD incident. This change decreases exponentially with the displacement of space charges.
Also, observations of the asymmetry between the first and second quarters of the cycle in higher frequency have been made. The theory of the impact of space charges on the asymmetry has been developed.
In addition, the results of practical tests on the PDIV level in three different dielectric liquids under three different frequencies have been reported.
The effects of applying voltage and PDs on the erosion of the needle tip in a needle-plane geometry have been investigated in two different aspects. The results have been presented and compared with previous research. It was shown that the erosion of the needle depends more on the type of material, on the rate of PD events, and on their magnitude than on the conductive current flow.
The optical partial discharge detection system has been set up and successfully tested using PMTs and a coincidence circuit. One of the goals achieved in this work is to prove the difference between the results obtained from the optical setup and the results from the charge acquisition detection. (ABC-circuit)
The IEC 61294 standard was criticized on the PDIV detection methodology by the results obtained from PD patterns of different insulating liquids.

## 6.2. Future Work

The research conducted has been an important step in the study of space charges in insulating liquids. To continue the research on space charges, more tests should be done around the causes of asymmetry of the conductive current waveform in insulating liquids. Further research on the PDIV surface. Another suggestion is to use a PDIV level test according to the IEC61294 setup and compare the results with this study.
There is a large research opportunity related to the optical measurement of PDIV. The question has now been raised as to what causes PD pulses to start at positive and negative half-cycles simultaneously and why the regular PD measuring system based on charge acquisition can not detect them.

Following the design of the rectified HV source in this study one can use this setup to further investigate the effects of different polarity space charges in dielectric liquids. Another suggestion for future work can be to use diodes without PDs to improve the rectified source to have less noise or use a different method to filter the data received from the digitiser in the presence of switching devices so that the conduction current can be calculated more accurately.
The use of optical PD detection, which has been demonstrated in detail in this work, can be taken as another option for testing with a half-cycle to neutralize the switching effect.
Another point for future work can be the use of an HV source with a higher capacity to maintain the perfect sinusoidal waveform during the switching procedure in half-cycle tests.
Many efforts were taken to filter the Nytro 10XN and MIDEL 7131 to $2\,\mu\mathrm{m}$. despite using adequate filters and a vacuum system to force the liquid through the filters multiple times; unfortunately, due to the high viscosity and adhesion of the used liquids, there were some particles remaining in the test cell. This has not happened with testing Cyclohexane because of the comparably lower adhesion and viscosity, but for Nytro 10XN and MIDEL 7131, the filtering was ineffective in some tests since there were particles in the test cell. Perhaps a better method of washing the test cell and filling in a more isolated situation should be considered for future work. the points for future work are:

- A more investigation into PDIV definition of IEC 61294 and testing more dielectric liquids.
- studying the causes of PD pulses starting at the positive half-cycle simultaneously with the negative half-cycle.
- Quantifying the space charge effect based on Mott-Gurney's law and developing the proper relations based on needle-plane geometry.
- further tests with rectified HV source to compare PD patterns with full-cycle tests.
- testing optical PD detection method for PDIV level detection.

# References


[1] M. M. Hirschler. *Electrical Insulating Materials: International Issues*. West Conshohocken, Pa.: ASTM, 2003, pp. 82–95. isbn: 978-0-8031-2613-8.

[2] J. M. Sketchley. “The role of transformer oil analysis in the detection of fault conditions”. In: *IEEE Colloquium on Assessment of Degradation Within Transformer Insulation Systems*. 1991, pp. 1.

[3] D. M. Mehta et al. “A review of critical evaluation of natural ester vis-a-vis mineral oil insulating liquid for use in transformers: Part II”. In: *IEEE Transactions on Dielectrics and Electrical Insulation*. Vol. 23. 3. 2016, pp. 1705–1712.

[4] D. K. Mahanta. “Green transformer oil: A review”. In: *2020 IEEE International Conference on Environment and Electrical Engineering and 2020 IEEE Industrial and Commercial Power Systems Europe (EEEIC/I&CPS Europe)*. IEEE. 2020, pp. 1–6.

[5] J. S. Chahal and C. C. Reddy. “Investigations on mustard oil for its suitability as insulating fluid in transformers”. In: *IEEE Transactions on Dielectrics and Electrical Insulation*. 2017.

[6] Sh. A. Azli et al. “A review on alternative oils as dielectric insulating fluids on power transformer”. In: *2019 IEEE 15th International Colloquium on Signal Processing & Its Applications (CSPA)*. IEEE. 2019, pp. 198–201.

[7] W. Naranpanawe et al. “Performance analysis of natural esters as transformer liquid insulation—Coconut, castor and sesame oils”. In: *2013 IEEE 8th International Conference on Industrial and Information Systems*. IEEE. 2013, pp. 105–109.

[8] M. Rafiq et al. “Use of vegetable oils as transformer oils–a review”. In: *Renewable and Sustainable Energy Reviews*. Vol. 52. Elsevier, 2015, pp. 308–324.

[9] R. V. Radhika, M. W. Iruthayarajan, and P. S. Pakianathan. “Investigation of critical parameters of mixed insulating fluids”. In: *2014 International conference on circuits, power and computing technologies [ICCPCT-2014]*. IEEE. 2014, pp. 357–362.

[10] WG Cigre. “A2. 35, Experiences in service with new insulating liquids”. In: *CIGRE Brouchure*. Vol. 436. 2010.

[11] M. Ş. Vihacencu, A. Ciuriuc, and L. M. Dumitran. “Experimental study of electrical properties of mineral and vegetable transformer oils”. In: *UPB Scientific Bulletin, Series C*. Vol. 75. 3. 2013, pp. 171–182.

[12] T. V. Oommen. “A new vegetable oil-based transformer fluid: development and verification”. In: *Proceedings of the CEIDP*. Victoria, British Columbia, Canada, 2000, pp. 308–312.

[13] F. M. T. Luna et al. “Assessment of biodegradability and oxidation stability of mineral, vegetable and synthetic oil samples”. In: *Industrial Crops and Products*. Vol. 33. 3. Elsevier, 2011, pp. 579–583.

[14] EU Council Directive. “96/59/EC of 16 September 1996 on the disposal of polychlorinated biphenyls and polychlorinated terphenyls (PCB/PCT)”. In: *Official Journal of the European Communities*. L243/34. 1996, pp. 24–9.

[15] International Electrotechnical Commission (IEC). *IEC TR 61294:1993 Electrical Insulating Materials: International Issues*. Technical Report IEC TR 61294. [Accessed on 20th of Nov. 2023]. IEC, 1993. url: `https://webstore.iec.ch/publication/5152`.

[16] *Insulating liquids - Determination of the dielectric dissipation factor by measurement of the conductance and capacitance*. IEC, 1998.

[17] Y. Bertrand and L. C. Hoang. “Vegetal oils as substitute for mineral oils”. In: *Proceedings of the 7th International Conference on Properties and Applications of Dielectric Materials*. Nagoya, June 2003.

[18] I. Radu. “Electric field calculation and the influence of water trees on insulation breakdown in needle–plane geometry”. In: *Journal of electrostatics*. Vol. 60. 1. Elsevier, 2004, pp. 49–67.

[19] E. Durand. *Electrostatique Les distributions*. 1964.

[20] J.H. Mason. “Dielectric breakdown in solid insulation”. In: *Progress in dielectrics*. Vol. 1. Heywood, 1959, pp. 1–58.

[21] S. S. Bamji, A. T. Bulinski, and K. M. Prasad. “Electric field calculations with the boundary element method”. In: *IEEE Transactions on Electrical Insulation*. Vol. 28. 3. IEEE, 1993, pp. 420–424.
[22] P. Moon and D. E. Spencer. *Field theory handbook: including coordinate systems, differential equations and their solutions*. Springer, 2012.
[23] T. Grav. “Mechanisms Governing the Occurrence of Partial Discharges in Insulation Liquids”. Master’s Thesis. Trondheim, Norway: Department of Physics, Norwegian University of Science and Technology (NTNU), 2013.
[24] O. Lesaint and T. V. Top. “Streamer inception in mineral oil under ac voltage”. In: *2011 IEEE International Conference on Dielectric Liquids*. IEEE. 2011, pp. 1–5.
[25] D. K. Mahanta and Sh. Laskar. “Electrical insulating liquid: A review”. In: *Journal of advanced dielectrics*. Vol. 7. 04. World Scientific, 2017, pp. 1730001.
[26] M. L. Campbell. “Cyclohexane”. In: *Ullmann’s encyclopedia of industrial chemistry*. Wiley Online Library, 2000.
[27] Wikimedia Commons contributors. *Cyclohexane for High School*. Wikimedia Commons, the free media repository. [Accessed on 20th of Nov. 2023]. 2023. url: https://commons.wikimedia.org/wiki/File:Cyclohexane_for_highschool.svg.
[28] W. Cigre. “A2. 35, Experiences in service with new insulating liquids”. In: *CIGRE Brouchure*. Vol. 436. 2010.
[29] Nynas AB. *Nytro 10XN Transformer Oil*. https://www.nynas.com/en/products/transformer-oils/products/nytro-10xn/. 2024.
[30] R. Chang. *Chemistry*. 10th. New York: McGraw-Hill, 2010.
[31] MIDEL & MIVOLT Fluids Ltd. *Midel 7131 Transformer Oil Brochure*. Corporate Headquarters/Europe, Hibernia Way, Trafford Park, Manchester M32 0ZD, United Kingdom. [Accessed:2024-03-30]. March 2024. url: https://www.midel.com.
[32] P. Gill. *Electrical Power Equipment Maintenance and Testing*. 2nd. Boca Raton: CRC Press, 2009, p. 193. isbn: 978-1-57444-656-2.
[33] X. Wang. *Partial discharge behaviours and breakdown mechanisms of ester transformer liquids under ac stress*. The University of Manchester (United Kingdom), 2011.
[34] B. Fagerli. “Converter Stress on Transformer Insulation Materials”. Master’s Thesis. Trondheim, Norway: Department of Energy, Environmental Engineering, Norwegian University of Science, and Technology (NTNU), Dec. 2022.
[35] A. A. Zaky and R. Hawley. *Conduction and Breakdown in Mineral Oil*. Peter Peregrinus, 1973.
[36] A. Denat. “Conduction and breakdown initiation in dielectric liquids”. In: *IEEE International Conference on Dielectric Liquids*. Trondheim, Norway, 2011, pp. 1–11.
[37] A. Castellanos. “Space Charged Limited Currents in Liquid Dielectrics”. In: *Electrohydrodynamics*. Ed. by A. Castellanos. Vol. 380. International Centre for Mechanical Sciences. Vienna: Springer, 1998. doi: 10.1007/978-3-7091-2522-9_11. url: https://doi-org.tudelft.idm.oclc.org/10.1007/978-3-7091-2522-9_11.
[38] J. Kuffel and P. Kuffel. *High voltage engineering fundamentals*. Elsevier, 2000.
[39] M. Bhatt and P. Bhatt. “Effect of voltage type and polarity on streamer dynamics in transformer oil”. In: *Materials Today: Proceedings*. Vol. 62. Elsevier, 2022, pp. 7131–7136.
[40] O. Hjortstam et al. “Measurements of ion mobility in transformer oil: Evaluation in terms of ion drift”. In: *Proceedings of 2012 IEEE Conference on Electrical Insulation and Dielectric Phenomena*. Vol. 2. Montreal, Canada, 2012, pp. 357–360.
[41] H. J. Wintle. “Charge motion in technical insulators: facts, fancies and simulations”. In: *IEEE transactions on dielectrics and electrical insulation*. Vol. 10. 5. IEEE, 2003, pp. 826–841.
[42] D. Braun. “Electronic injection and conduction processes for polymer devices”. In: *Journal of Polymer Science Part B: Polymer Physics*. Vol. 41. 21. Wiley Online Library, 2003, pp. 2622–2629.
[43] N. Felici and J. P. Gosse. “Injection d’ions par des électrodes métalliques dans les hydrocarbures liquides de résistivité élevée”. In: *Revue de Physique Appliquée*. Vol. 14. 5. Société Française de Physique, 1979, pp. 629–633.
[44] K. Niayesh and M. Runde. *Power switching components*. Springer, 2017.
[45] Q. Xue et al. “Mobility of Charge Carriers in Dielectric Liquids”. In: *2019 IEEE 20th International Conference on Dielectric Liquids (ICDL)*. 2019, pp. 1-4. doi: 10.1109/ICDL.2019.8796776.

[46] W. Shockley. “Currents to conductors induced by a moving point charge”. In: *Journal of applied physics*. Vol. 9. 10. American Institute of Physics, 1938, pp. 635–636.
[47] D. S. McGregor et al. “CdZnTe semiconductor parallel strip Frisch grid radiation detectors”. In: *IEEE Transactions on Nuclear Science*. Vol. 45. 3. IEEE, 1998, pp. 443–449.
[48] C. D. Child. “Discharge From Hot CaO”. In: *Phys. Rev. (Series I)*. Vol. 32. American Physical Society, May 1911, pp. 492–511. doi: 10.1103/PhysRevSeriesI.32.492. url: https://link.aps.org/doi/10.1103/PhysRevSeriesI.32.492.
[49] N. F. Mott and R. W. Gurney. *Electronic Processes in Ionic Crystals*. 1st. Oxford University Press, 1940.
[50] P. N. Murgatroyd. “Theory of space-charge-limited current enhanced by Frenkel effect”. In: *Journal of Physics D: Applied Physics*. Vol. 3. 2. IOP Publishing, 1970, pp. 151.
[51] L. Lundgaard. *Dielectric performance of insulating liquids for transformers*. Technical report. CIGRE, 2021.
[52] P. Atten, B. Malraison, and M. Zahn. “Electrohydrodynamic plumes in point-plane geometry”. In: *IEEE transactions on dielectrics and electrical insulation*. Vol. 4. 6. 1997, pp. 710–718.
[53] *Insulating Liquids - Measurement of Relative Permittivity, Dielectric Dissipation Factor ($\tan\delta$), and D.C. Resistivity*. IEC, 2004.
[54] U. Gäfvert et al. “Electrical Field Distribution in Transformer Oil”. In: *IEEE Transactions on Electrical Insulation*. Vol. 27. 3. June 1992, pp. 647-660. doi: 10.1109/14.142730.
[55] H. S. Smalø et al. “Field dependence on the molecular ionization potential and excitation energies compared to conductivity models for insulation materials at high electric fields”. In: *Journal of Applied Physics*. Vol. 109. 7. AIP Publishing, 2011.
[56] N. Davari, P. O. Astrand, and T. Van Voorhis. “Field-dependent ionisation potential by constrained density functional theory (vol 111, pg 1456, 2013)”. In: *MOLECULAR PHYSICS*. Vol. 111. 21. TAYLOR & FRANCIS LTD 4 PARK SQUARE, MILTON PARK, ABINGDON OX14 4RN, OXON …, 2013, pp. 3334–3334.
[57] J. Eikeset. “Photon Activity from Partial Discharges in Liquid Dielectrics: Experimental Test Setup and Measurements”. MA thesis. Norwegian University of Science and Technology, June 2014.
[58] R. Kattan, A. Denat, and O. Lesaint. “Generation, growth, and collapse of vapor bubbles in hydrocarbon liquids under a high divergent electric field”. In: *Journal of applied physics*. Vol. 66. 9. American Institute of Physics, 1989, pp. 4062–4066.
[59] E. Ildstad. *TET4160 - High Voltage Insulation Materials*. Tech. rep. NTNU, Department of Electric Power Engineering, 2021.
[60] L. E. Lundgaard. *Partial Discharges - General Description*. Tech. rep. SINTEF Energy Research, 2018.
[61] M. Pompili et al. “The effect of the definition used in measuring partial discharge inception voltages”. In: *IEEE Transactions on Electrical Insulation*. Vol. 28. 6. 1993, pp. 1002-1006. doi: 10.1109/14.249373.
[62] F. Skirbekk. “Transformer Insulation Stressed by Power Converters”. Master’s Thesis. Trondheim, Norway: Norwegian University of Science and Technology (NTNU), June 2021.
[63] P. Gournay and O. Lesaint. “Evidence of the gaseous nature of positive filamentary streamers in various liquids”. In: *Proceedings of IEEE Conference on Electrical Insulation and Dielectric Phenomena-(CEIDP’94)*. IEEE. 1994, pp. 834–839.
[64] L. E. Lundgaard and S. L. Kyrkjeeide. “Evaluation of dielectric liquids by measurement of their partial discharge characteristics”. In: *Proceedings of IEEE Conference on Electrical Insulation and Dielectric Phenomena-(CEIDP’94)*. IEEE. 1994, pp. 901–909.
[65] R. Schwarz and M. Muhr. “Modern technologies in optical partial discharge detection”. In: *2007 Annual Report - Conference on Electrical Insulation and Dielectric Phenomena*. Vancouver, BC, Canada, 2007, pp. 163-166. doi: 10.1109/CEIDP.2007.4451557.
[66] X. Yang et al. “Comparison between optical and electrical methods for partial discharge measurement”. In: *Proceedings of the 6th International Conference on Properties and Applications of Dielectric Materials (Cat. No. 00CH36347)*. Vol. 1. IEEE. 200, pp. 300–303.
[67] K. Forsyth. “Optical partial discharge detection”. In: *Iris Rotating machine Technical Conference*. 1998.
[68] Omicron Electronics GmbH. *MPD 600 User Manual, Version MPD600.AE.6*. User Manual. 2012.

[69] S. Ingebrigtsen. “The Influence of Chemical Composition on Streamer Initiation and Propagation in Dielectric Liquids”. PhD thesis. Trondheim, Norway: Norwegian University of Science and Technology (NTNU), 2008.
[70] K. Weman. *Welding processes handbook*. Elsevier, 2011.
[71] Matsusada Precision Inc. *Photomultiplier Tubes - Application Note*. Release: 2019-08-22, Update: 2023-01-05. 2019. url: https://www.matsusada.com/application/ps/photomultiplier_tubes/.
[72] Hamamatsu Photonics co. *Photomultiplier Tubes and Related Products*. Hamamatsu: Hamamatsu Photonics K.K., Electron Tube Division, 2010.
[73] ORTEC. *Model 935 Quad Constant Fraction 200 MHz Discriminator Operating and Service Manual*. ORTEC. 2003.
[74] P. Rozga et al. “A review on synthetic ester liquids for transformer applications”. In: *Energies*. Vol. 13. 23. MDPI, 6429, p. 2020.

# A

# Appendix 1: Previous studies

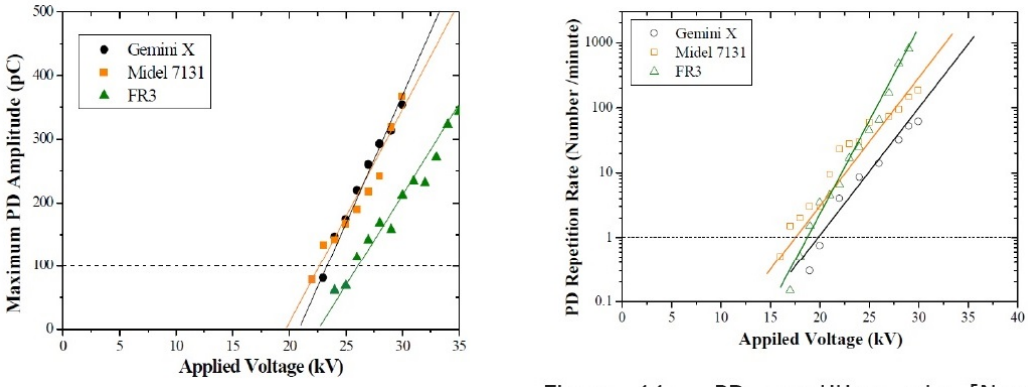


**Figure A.1:** maximum PD amplitude and repetition rate for three different materials adopted from [33]

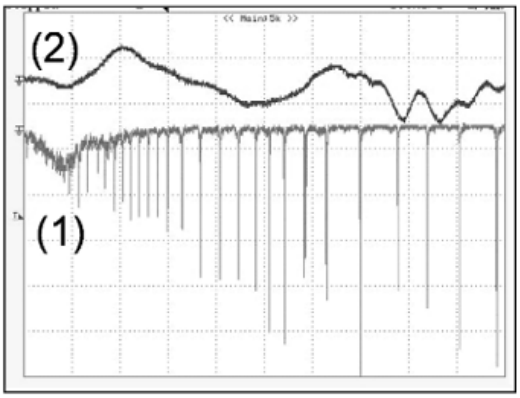


**Figure A.2:** Comparison of conventional detected PD signal (2) and optical detected pulses (1) in oil adopted from [65]

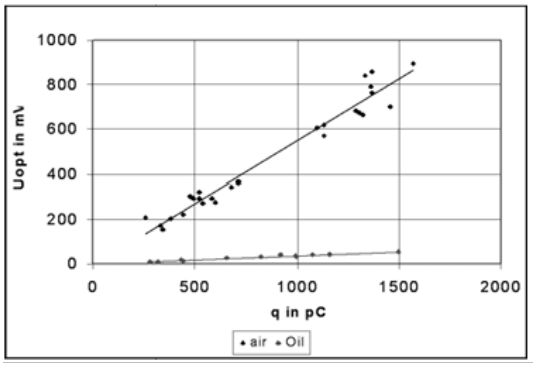


**Figure A.3:** The relationship of the optical signal and the discharge level in the air and in oil at the same arrangements adopted from [65]

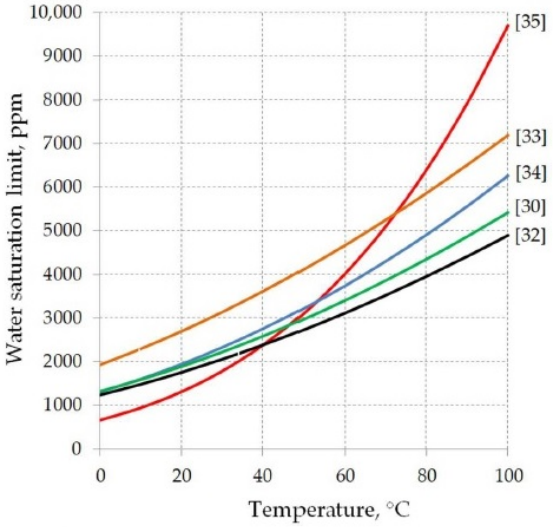


**Figure A.4:** details of MIDEL 7131 water contamination effect [74]

# B

# Appendix 2: Datasheets

**MIDEL 7131 Fluid Properties**

| | | IEC 61099 | MIDEL 7131 |
|---|---|---|---|
| Property | Test Method | Un-used new fluid property requirements | Typical Values |
| **Physical** | | | |
| Colour | ISO 2211 | Max. 200 Hazen | 125 |
| Appearance | | Clear, free from water and suspended matter and sediment | Clear, free from water and suspended matter and sediment |
| Density at 20°C (kg/dm³) | ISO 3675 or ISO 12185 | Max. 1 | 0.97 |
| Kinematic Viscosity (mm²/sec) | ISO 3104 | | |
| at 40°C | | Max. 35 | 29 |
| at -20°C | | Max. 3000 | 1440 |
| Flash Point PMCC (°C) | ISO 2719 | Min. 250 | 260 |
| Fire Point (°C) | ISO 2592 | Min. 300 | 316 |
| Pour Point (°C) | ISO 3016 | Max. -45 | -56 |
| Crystallization | IEC 61099 (2010 Annex A) | No crystals | No crystals |
| Biodegradation | Readily Biodegradable | | Fully/Readily Biodegradable |
| **Electrical** | | | |
| Dielectric Breakdown (kV) | IEC 60156 | Min. 45 | >75 |
| Power Factor at 90°C | IEC 60247 | Max. 0.03 | <0.008 |
| DC Resistivity at 90°C (GΩ.m) | IEC 60247 | Min. 2 | >20 |
| **Chemical** | | | |
| Water Content (mg/kg) | IEC 60814 | Max. 200 | 50 |
| Acidity (mg KOH/g) | IEC 62021-1 or IEC 62021-2 | Max. 0.03 | <0.03 |
| Oxidation Stability (164hr) | IEC 61125C | | |
| Total Acidity (mg KOH/g) | | Max. 0.3 | 0.02 |
| Total Sludge (% mass) | | Max. 0.01 | <0.01 |

MIDEL 7131 is supplied in accordance with IEC industry standard acceptance values and test methods. The displayed typical values do not form part of this specification.

**Figure B.1:** MIDEL 7131 details from Midel company' website [31]

**Table B.1:** Nytro 10XN Transformer Oil product datasheet [29]

| Property | Unit | Guaranteed Data | Typical Data |
|---|---|---|---|
| **1. Physical** | | | |
| Appearance | – | Clear, free from sediment | – |
| Density, 20°C | $kg/dm^3$ | 0.895 | 0.876 |
| Viscosity, 40°C | $mm^2/s$ | 8.0 | 7.6 |
| Viscosity, -30°C | $mm^2/s$ | 800 | 730 |
| Flash Point, PM | °C | 140 | 144 |
| Pour Point | °C | -45 | -60 |
| **2. Chemical** | | | |
| Neutralization value | mg KOH/g | 0.03 | $<$0.01 |
| Corrosive sulphur | – | Non-corrosive | – |
| Aromatic content | % | – | 7 |
| Antioxidant, phenols | Wt% | – | 0.3 |
| Water content | mg/kg | 30 | $<$20 |
| **3. Electrical** | | | |
| Dielectric dissipation factor at 90°C | – | 0.005 | $<$0.001 |
| Interfacial tension | mN/m | 40 | 45 |
| Breakdown voltage | kV | 30 | 40-60 |
| **4. Oxidation Stability** | | | |
| At 100°C 164h | – | – | – |
| Neutralization value | mg KOH/g | – | $<$0.01 |
| Sludge | Wt% | – | $<$0.005 |
| At 120°C | – | – | – |
| Induction period | h | – | $>$236 |
| At 110°C 28 days | – | – | – |
| Baader test | | | |
| Saponification number | mg KOH/g | 0.15 | – |
| Sludge | Wt% | – | $<$0.005 |
| Dielectric dissipation factor at 90°C | – | 0.003 | – |

# C

# Appendix 3: Python Script

*Python script used for analysing the digitizer data for cyclohexane at* $30\,\mathrm{Hz}$ *and* $14.52\,\mathrm{kV}$ *with sample rate* $200\,\mathrm{K}$

```
"""
Created on Sat Feb 17 12:02:58 2024

@author: Mohammad Fazlalizadeh

Norges teknisk-naturvitenskapelige universitet

"""
import pandas as pd
import matplotlib.pyplot as plt
import os
from scipy.signal import find_peaks
import numpy as np
from scipy.optimize import minimize
import math

# Function to load data from a folder path and store it in the dictionary
def load_data(folder_path):
    file_list = os.listdir(folder_path)
    data = {}
    for file_name in file_list:
        if file_name.endswith('.asc'):
            file_path = os.path.join(folder_path, file_name)
            data[file_name] = pd.read_csv(file_path, delim_whitespace=True,
            ↪  header=None, skiprows=13)
    return data

# Cyclohexane
# Define folder paths for each frequency and sampling rate
folder_paths = {
    '30Hz': {
        'long_33630': 'file path should be added here',
        'PDtrigged_200KSs': 'file path should be added here'
    },
    '45Hz': {
        '50KSs_33630': 'file path should be added here',
```

```
        '200KSs_33630': 'file path should be added here'
    },
    '60Hz': {
        '50KSs_17071': 'file path should be added here',
        '100KSs_17071': 'file path should be added here',
        '100KSs_33630': 'file path should be added here',
    }
}
# Specify the folder path to save the graphs
save_folder_path = 'save folder path should be added here'

# Create the save folder if it doesn't exist
os.makedirs(save_folder_path, exist_ok=True)

# Create an empty dictionary to store data
data_dict = {
    '30Hz': {'long_33630': {}, 'PDtrigged_200KSs': {}},
    '45Hz': {'50KSs_33630': {}, '200KSs_33630': {}},
    '60Hz': {'50KSs_17071': {}, '100KSs_17071': {}, '100KSs_33630': {}}
}

# Load data from folder paths
for freq, freq_data in folder_paths.items():
    for sampling_rate, folder_path in freq_data.items():
        data_dict[freq][sampling_rate] = load_data(folder_path)

#%% Plotting data in different graphs and saving them
for freq, freq_data in data_dict.items():
    for sampling_rate, sampling_data in freq_data.items():
        graph_number = 0  # Reset graph number for each combination of frequency and
        ↪  sampling rate
        for file_name, data in sampling_data.items():
            plt.plot(data.iloc[:, 0], data.iloc[:, 1], label=file_name)
            plt.title(f'{file_name} (Graph {graph_number})')
            plt.xlabel('Time')
            plt.ylabel('Voltage')
            save_file_path_svg = os.path.join(save_folder_path,
            ↪  f'{file_name.replace(".asc", f"_plot_{graph_number}.svg")}')
            save_file_path_jpeg = os.path.join(save_folder_path,
            ↪  f'{file_name.replace(".asc", f"_plot_{graph_number}.jpg")}')
            plt.savefig(save_file_path_svg, format='svg')
            plt.savefig(save_file_path_jpeg, format='jpeg')
            plt.show()
            graph_number += 1  # Increment graph number

#%% Extracting data from dictionary and plotting on the same graph
# Define the location in the nested dictionary
dictionary_loc = ('30Hz', 'long_33630')
# The name of the graphs being saved
plot_title = "Cyclohexane_30Hz_14.52kVpeak_1uAV_33360Vrv.asc"
peakvoltage = 14.52
frequency = 30
voltage_data_set = 39
current_data_set = 38
sensor_ratio = 1000  # nA per V
FFT_cycle_num = 24
```

```
frequency_limit = 300
sample_rate = 200000
plot_show_time = (-0.0440, -0.008) #cyclo 30

# Access the nested dictionary based on the location specified
if dictionary_loc[0] in data_dict and dictionary_loc[1] in data_dict[dictionary_loc[0]]:
    nested_dict = data_dict[dictionary_loc[0]][dictionary_loc[1]]
    file_names_list = list(nested_dict.keys())
    # Check for the file_names_list to contain at least one name
    if file_names_list:
        # Check if the indices are within the range
        if 0 <= voltage_data_set < len(file_names_list) and 0 <= current_data_set < len(file_names_list):
            # Access the specified data frames in the nested dictionary
            voltage_data = list(nested_dict.values())[voltage_data_set]
            current_data = list(nested_dict.values())[current_data_set]
            # Plotting Voltage and Current data on the same graph
            plt.figure(figsize=(20, 12))  # Set the figure size
            plt.plot(voltage_data.iloc[:, 0], voltage_data.iloc[:, 1] / 50, label=f"Voltage[V]/50 ({file_names_list[voltage_data_set]})")
            plt.plot(current_data.iloc[:, 0], current_data.iloc[:, 1] * sensor_ratio, label=f"Current[nA] ({file_names_list[current_data_set]})")
            plt.title("Voltage and Current raw Data")
            plt.xlabel('Time')
            plt.ylabel('Value')
            plt.legend()
            plt.grid(True)  # Add grid
            plt.show()
        else:
            print("Invalid indices provided.")
    else:
        print("No data available in the nested dictionary.")
else:
    print("Location not found in the main dictionary.")
# Write data frames into new separate arrays
num_voltage = voltage_data.iloc[:, 1].to_numpy(dtype=np.float64)
num_current = current_data.iloc[:, 1].to_numpy(dtype=np.float64) * sensor_ratio
time = voltage_data.iloc[:, 0].to_numpy(dtype=np.float64)
# Combine the arrays horizontally
array = np.column_stack((time, num_voltage, num_current))

#%% Finding zero crossings and complete cycles
# Function to find the index of the maximum peak in the voltage data
def find_max_peak_index(voltage_data_values):
    max_peak_index = np.argmax(voltage_data_values)
    return max_peak_index

# Function to find the index corresponding to pi/2 before the maximum voltage
def find_index_pi_over_2_before_max(data_values, max_peak_index, frequency):
    # Calculate the period of the sinusoid (assuming a sinusoidal waveform)
    period = 1 / frequency
    # Calculate the time difference corresponding to pi/2 phase difference
    time_difference_pi_over_2 = period / 4
    # Find the time value corresponding to pi/2 before the maximum voltage
```

```
140     time_pi_over_2_before_max = data_values[max_peak_index, 0] -
        ↪ time_difference_pi_over_2
141     # Find the index corresponding to this time value
142     index_pi_over_2_before_max = np.argmin(np.abs(data_values[:, 0] -
        ↪ time_pi_over_2_before_max))
143     return index_pi_over_2_before_max
144 # Function to trim the data at the zero crossing just before the maximum voltage
145 def trim_to_zero_crossing_before_max(data_values, zero_crossing_index ,
    ↪ FFT_cycle_num, samples_per_period):
146     cycles_points = samples_per_period * FFT_cycle_num
147     trimmed_array_data = data_values[0: cycles_points]
148     return trimmed_array_data, cycles_points
149 samples_per_period = int(sample_rate / frequency)
150 voltage_max_peak_index = find_max_peak_index(array[:,1])
151 index_pi_over_2_before_max = find_index_pi_over_2_before_max(array,
    ↪ voltage_max_peak_index, frequency)
152 trimmed_array, cycles_points =
    ↪ trim_to_zero_crossing_before_max(array,index_pi_over_2_before_max, FFT_cycle_num,
    ↪ samples_per_period)
153
154 #%% Perform FFT on each signal
155 fft_voltage = np.fft.fft(trimmed_array[:, 1])
156 fft_current = np.fft.fft(trimmed_array[:, 2])
157 # Frequency values corresponding to the FFT result
158 freq1 = np.fft.fftfreq(len(fft_voltage), d=(trimmed_array[1, 0] - trimmed_array[0,
    ↪ 0]))
159 # d is the distance between two data points for example 1399-1400
160 freq2 = np.fft.fftfreq(len(fft_current), d=(trimmed_array[1, 0] - trimmed_array[0,
    ↪ 0]))
161 # d is the distance between two data points for example 1399-1400
162 # Find the index corresponding to the main frequency
163 main_f_voltage_index = np.argmax(np.abs(fft_voltage))
164 main_f_current_index = np.argmax(np.abs(fft_current))
165 # Extract the phase angle for the main frequency
166 phase_angle_voltage = np.angle(fft_voltage[main_f_voltage_index])
167 phase_angle_current = np.angle(fft_current[main_f_current_index])
168 # Convert the phase angle from radians to degrees
169 phase_angle_voltage_degrees = np.degrees(phase_angle_voltage)
170 phase_angle_current_degrees = np.degrees(phase_angle_current)
171 # Extract the amplitude of the main component in the current signal
172 #amplitude_main =
    ↪ np.abs(fft_current[main_f_current_index])/(0.5*len(trimmed_current)) # amplitude
    ↪ is multiplied by half of the number of data points by definition of FFT
173 # Set the threshold for FFT component detection
174 threshold = 1.00036  # Adjust this threshold as needed
175 threshold_voltage = threshold * np.max(np.abs(fft_voltage))
176 # Find FFT components above the threshold for voltage
177 significant_indices_voltage = np.where(np.abs(fft_voltage) > threshold_voltage)[0]
178 significant_freqs_voltage = freq1[significant_indices_voltage]
179 # Find the main frequency index for voltage
180 main_f_voltage_index = np.argmax(np.abs(fft_voltage))
181 # Exclude the main frequency from the list of significant frequencies
182 significant_freqs_voltage = significant_freqs_voltage[significant_freqs_voltage !=
    ↪ freq1[main_f_voltage_index]]
183 significant_freqs_voltage = significant_freqs_voltage[significant_freqs_voltage !=
    ↪ -freq1[main_f_voltage_index]]
```

```
# Find corresponding indices in current FFT and eliminate those components
significant_indices_current = [np.abs(freq2 - freq).argmin() for freq in significant_freqs_voltage]
fft_current_filtered = fft_current.copy()
fft_current_filtered[significant_indices_current] = 0
fft_current_filtered[0] = 0

#%% Plot the FFT output of the voltage data
plt.figure(figsize=(20, 12))
# fft voltage and current amplitude per length that is necessary
FFT_voltage = fft_voltage / (0.5 * len(trimmed_array))
FFT_current = fft_current / (0.5 * len(trimmed_array))
fft_current_filtered =  fft_current_filtered/ (0.5 * len(trimmed_array))
plt.plot(freq1, np.abs(FFT_voltage), label='FFT of the voltage signal')
plt.title(plot_title.replace('.asc', '_FFT'))
plt.axvline(x= frequency, color='red', linestyle='--', label= dictionary_loc[0])
plt.axvline(x= frequency_limit, color='orange', linestyle='--', label= 'cut-off frequency')
plt.xlim(0, 1000)
#plt.ylim(0,100)
plt.xlabel('Frequency')
plt.ylabel('Amplitude [v]')
plt.legend()
plt.grid()
# Set y-axis to be logarithmic
plt.yscale('log')
save_file_path_svg = os.path.join(save_folder_path, plot_title.replace('.asc', '_FFT_voltage.svg'))
save_file_path_jpeg = os.path.join(save_folder_path, plot_title.replace('.asc', '_FFT_voltage.jpeg'))
plt.axhline(y= threshold_voltage/ (0.5 * len(trimmed_array)), color='red', linestyle='--', label= dictionary_loc[0])
plt.savefig(save_file_path_svg, format='svg')
plt.savefig(save_file_path_jpeg, format='jpeg')
plt.show()

# Save the voltage FFT to an ASC file
np.savetxt(os.path.join(save_folder_path, plot_title.replace('.asc', '_FFT_voltage_data.asc')) , np.column_stack((freq1,FFT_voltage)), header="Frequency\tAmplitude", delimiter='\t', comments='')
#%% Plot the FFT output of the Current data
plt.figure(figsize=(20, 12))
plt.plot(freq2, np.abs(FFT_current)* sensor_ratio , color='green', label='FFT of the current signal')
plt.plot(freq2, np.abs(fft_current_filtered)* sensor_ratio , color='red', label='filtered current signal')
plt.title(plot_title.replace('.asc', '_FFT'))
plt.axvline(x= frequency, color='red', linestyle='--', label= dictionary_loc[0])
plt.axvline(x= frequency_limit, color='orange', linestyle='--', label= 'cut-off frequency')
plt.xlim(0, 1000)
#plt.ylim(0,100)
plt.xlabel('Frequency')
plt.ylabel('Amplitude [nA]')
plt.legend()
plt.grid()
```

```
230 # Set y-axis to be logarithmic
231 plt.yscale('log')
232 save_file_path_svg = os.path.join(save_folder_path, plot_title.replace('.asc',
    ↪ '_FFT_current.svg'))
233 save_file_path_jpeg = os.path.join(save_folder_path, plot_title.replace('.asc',
    ↪ '_FFT_current.jpeg'))
234 plt.savefig(save_file_path_svg, format='svg')
235 plt.savefig(save_file_path_jpeg, format='jpeg')
236 plt.show()
237
238 # Save the voltage FFT to an ASC file
239 np.savetxt(os.path.join(save_folder_path, plot_title.replace('.asc',
    ↪ '_FFT_current_data.asc')) , np.column_stack((freq1,FFT_voltage)),
    ↪ header="Frequency\tAmplitude", delimiter='\t', comments='')
240 #%% Calculating the Capacitance
241 # Find the indices where freq1 is above the frequency limit
242 indices_above_limit = np.where(np.abs(freq1) > frequency_limit)[0]
243 # Set the adjacent elements in fft_voltage to zero for the indices above the limit
244 FFT_voltage[indices_above_limit] = 0
245 FFT_voltage[indices_above_limit + 1] = 0
246 # eliminate the offset within the FFT signal of the voltage
247 FFT_voltage[0] = 0
248 # Set the adjacent elements in fft_current to zero for the indices above the limit
249 FFT_current[indices_above_limit] = 0
250 FFT_current[indices_above_limit + 1] = 0
251 FFT_current[0] = 0
252 # Find the mean value of voltage and current
253 mean_voltage = np.mean(trimmed_array[:, 1])
254 mean_current = np.mean(trimmed_array[:, 2])
255 # Subtract the mean value from voltage and current to remove offset
256 trimmed_voltage_no_offset = trimmed_array[:, 1] - mean_voltage
257 trimmed_current_no_offset = trimmed_array[:, 2] - mean_current
258 # find the max value of the voltage with no offset
259 trimmed_voltage_no_offset_max_index = np.argmax(trimmed_voltage_no_offset)
260 # Calculate the derivative of the voltage in the frequency domain
261 derivative_voltage_freq_domain = 2j * np.pi * freq1 * FFT_voltage * (0.5 *
    ↪ len(trimmed_array))
262 # Perform the inverse FFT to obtain the derivative in the time domain
263 derivative_voltage = np.fft.ifft(derivative_voltage_freq_domain)
264 # reproducing the voltage from the FFT of the voltage after filtering
265 voltage_redo = np.fft.ifft(FFT_voltage) * (0.5 * len(trimmed_array))
266 # reproducing the current from the FFt of the current after filtering
267 current_redo = np.fft.ifft(fft_current_filtered) * (0.5 * len(trimmed_array))
268 # capacitance of each harmonic by i(s)/(v(S)*2pi*f) formula
269 capacitance_array = FFT_current * 1e-9 / (FFT_voltage * 2j * np.pi * freq1+ 1e-30)
270 # Calculate capacitive current using the optimal capacitance
271 capacitive_current = derivative_voltage *
    ↪ np.real(capacitance_array[main_f_voltage_index]) * 1e9 #113.5e-15 223.5e-15
272 # amplitude of the voltage has been multiplied because derivative of the voltage has
    ↪ been calculated based on trimmed voltage
273 resistive_current = (current_redo - capacitive_current)
274 fft_conductive_current = np.fft.fft(resistive_current)
275 # Frequency values corresponding to the FFT result
276 freq_cond_current = np.fft.fftfreq(len(fft_conductive_current),
    ↪ d=(resistive_current[1] - resistive_current[0]))
277 # d is the distance between two data points for example 1399-1400
```

```
# Find the index corresponding to the main frequency
main_f_cc_index = np.argmax(np.abs(fft_conductive_current))
main_freq_cc = freq_cond_current[main_f_cc_index]
# Find the indices where freq1 is above the frequency limit
indices_other_than_main = np.where(np.abs(freq_cond_current) !=
↪  np.abs(main_freq_cc))[0]
# Set the adjacent elements in fft_conductive_current to zero for the indices above
↪  the limit
fft_conductive_current[indices_other_than_main] = 0
# Perform inverse FFT to get the time-domain signal
conductive_current_redo = np.fft.ifft(fft_conductive_current)
Max_negative_resistive_current =  -1 *
↪  resistive_current[np.argmax(resistive_current)]
Max_positive_resistive_current =  -1 * resistive_current[np.argmax(-1 *
↪  resistive_current)]
Max_first_harmonic_resistive_current =
↪  conductive_current_redo[np.argmax(conductive_current_redo)]
plt.plot(trimmed_array[:, 1], color='red', label = 'measured')
plt.plot(voltage_redo, color='blue', label = 'filtered')
plt.xlim(0, 20000)
plt.legend()

#%% Create the plot
bandwidth_title = f"bandwidth_0-{frequency_limit}Hz"
combo_plot_title = f"{plot_title.replace('.asc', '')}_{bandwidth_title}.asc"
fig, ax1 = plt.subplots(figsize=(14, 6))
# Find the indices corresponding to plot_show_time
start_time, end_time = plot_show_time
start_index = np.argmax(trimmed_array[:, 0] >= start_time)
end_index = np.argmax(trimmed_array[:, 0] >= end_time)
# Plot the real part of capacitive_current on the left y-axis
ax1.plot(trimmed_array[start_index:end_index, 0], -1*
↪  trimmed_voltage_no_offset[start_index:end_index] / 1000, 'b-',
↪  label='measured_Voltage')
ax1.plot(trimmed_array[start_index:end_index, 0], -1*
↪  voltage_redo[start_index:end_index] / 1000, color='violet',
↪  label='filtered_Voltage')
ax1.set_xlabel('Time')
ax1.set_ylabel('kV', color='b')
ax1.tick_params('y', colors='b')
# Create the right y-axis and plot the real part of derivative_voltage
ax2 = ax1.twinx()
ax2.plot(trimmed_array[start_index:end_index,0], -1*
↪  capacitive_current[start_index:end_index], 'red', label='Capacitive_current')
ax2.plot(trimmed_array[start_index:end_index,0], -1*
↪  trimmed_current_no_offset[start_index:end_index], 'orange',
↪  label='Measured_current')
ax2.plot(trimmed_array[start_index:end_index,0], -1*
↪  resistive_current[start_index:end_index] , 'green', label='Conductive_current ')
#ax2.set_ylim(-1800, 1800)
#plt.axvline(x=0, color='red', linestyle='--', label='OV')
ax2.set_ylabel('nA', color='r')
ax2.tick_params('y', colors='r')
ax2.grid(True)
# Display the legend
lines, labels = ax1.get_legend_handles_labels()
```

```
lines2, labels2 = ax2.get_legend_handles_labels()
ax2.legend(lines + lines2, labels + labels2, loc='lower left')
plt.title(combo_plot_title)
save_file_path_svg = os.path.join(save_folder_path, combo_plot_title.replace('.asc' , '.svg'))
save_file_path_jpeg = os.path.join(save_folder_path, combo_plot_title.replace('.asc' , '.jpeg'))
plt.savefig(save_file_path_svg, format='svg')
plt.savefig(save_file_path_jpeg, format='jpeg')
plt.show()
# Save the resistive_current data to an ASC file
#np.savetxt(os.path.join(save_folder_path, plot_title.replace('.asc', '_resistive_current_data.asc')), np.column_stack((trimmed_array[:,0], resistive_current)), header="Time (s)\tResistive Current (nA)", delimiter='\t', comments='')

#%%
fig, ax1 = plt.subplots(figsize=(6, 4))
full_period_points = int((1 / frequency) * sample_rate) + 5
cc_start = full_period_points * 0 + 5650
ax1.plot(trimmed_array[cc_start:full_period_points*1 + cc_start, 0], -1*resistive_current[cc_start:full_period_points*1 + cc_start], 'green', label='Resistive current')
ax1.set_ylim(-50, 50)
# Add a horizontal line at y=0 on ax1
ax1.axhline(y=0, color='black', linestyle='--')
# Create the right y-axis and plot the real part of derivative_voltage
ax2 = ax1.twinx()
peakvoltage_label = f"Vpeak:{peakvoltage}[kV]"
ax2.plot(trimmed_array[cc_start:full_period_points*1 + cc_start, 0], -1*voltage_redo[cc_start:full_period_points*1 + cc_start]/1000, 'blue', label= peakvoltage_label)
# Set labels for y-axes
ax1.set_ylabel('Current [nA]')
ax2.set_ylabel('Voltage [kV]')
ax1.set_xlabel('Time [s]')
# Add legends
#ax1.legend(loc='lower left')
ax2.legend(loc='lower left')
# Adjust plot layout to prevent cropping in SVG
plt.tight_layout()
sec_combo_plot_title = f"{plot_title.replace('.asc', 'C&V_vs._t_filterbw')}_{frequency_limit}.asc"
save_file_path_svg = os.path.join(save_folder_path, sec_combo_plot_title.replace('.asc', '.svg'))
save_file_path_jpeg = os.path.join(save_folder_path, sec_combo_plot_title.replace('.asc', '.jpeg'))
plt.savefig(save_file_path_svg, format='svg')
plt.savefig(save_file_path_jpeg, format='jpeg')
plt.show()
```